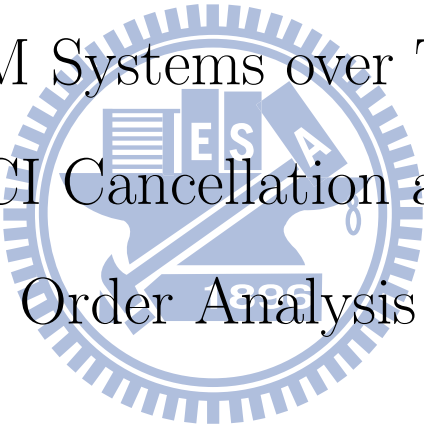


國立交通大學
電子工程學系電子研究所
博士論文

BICM-OFDM 系統在時變通道下之干擾
消除和多樣性分析

BICM-OFDM Systems over Time-Varying
Channels: ICI Cancellation and Diversity
Order Analysis



研究生：林欣德

指導教授：桑梓賢

林大衛

中華民國一〇二年四月

BICM-OFDM 系統在時變通道下之干擾消除和多樣性分析

BICM-OFDM Systems over Time-Varying Channels: ICI

Cancellation and Diversity Order Analysis

研究生：林欣德

Student: Hsin-De Lin

指導教授：桑梓賢

Advisors: Dr. Tzu-Hsien Sang

林大衛

Dr. David W. Lin



A Dissertation

Submitted to Department of Electronics Engineering and Institute of Electronics

College of Electrical and Computer Engineering

National Chiao Tung University

in Partial Fulfillment of the Requirements

for the Degree of Doctor of Philosophy

in

Electronics Engineering

April 2013

Hsinchu, Taiwan, Republic of China

中華民國一〇二年四月

BICM-OFDM 系統在時變通道下之干擾消除和多樣性分析

研究生：林欣德

指導教授：桑梓賢

林大衛

國立交通大學電子工程學系電子研究所

摘要

在高速移動的環境下，正交分頻多工 (OFDM) 系統將遭遇通道在一個符碼的時間內產生一定程度以上變化，其影響使得子載波間彼此產生干擾 (ICI) 進而導致正交特性被破壞。倘使沒有妥善處理子載波間干擾，將會造成系統效能嚴重低落。

本論文著眼於移動式無線通訊系統，在採取正交分頻多重存取 (OFDMA) 的先進技術之下，因高速移動而將面臨上述的問題。考慮在其規格限制下，如何設計出適合實現之低複雜度方法，且具有足夠的效能。本論文從多方面的考量來發展有效率地處理時變通道之方法。

爲了充分了解時變通道對正交分頻多重存取系統所造成的影響，首先必須對於時間以及頻率方面皆會有選擇性的雙選擇性衰落 (doubly-selective fading) 通道的基本性質以及模型建立等問題進行研究。透過推導以及觀察，我們發現了一個簡單易得且可用來度量出各子載波所承受之干擾程度的指標 (ICI indicator)，此指標將爲隨後所提出的高效率子載波間干擾消除策略做鋪陳。此外，我們對於子載波間干擾指標也進行了詳盡的分析從而闡述其可行性。從結果中可知其機率分布和移動速度密切相關，並且對於其他因素例如通道功率延遲以及都普勒功率頻譜則較不敏感。因此子載波間干擾指標可以廣泛地適用於不同的通道環境下。我們也討論了其他可能的應用，例如，其機率分布可提供最大的都普勒頻率或是通道衰落的速率等極爲有價值的資訊。

在了解子載波間干擾的生成機制後，我們發展了兩種方法來處理子載波間干擾。第一種方法是藉由子載波間干擾指標的輔助，提出了基於各個子載波適應性 (PSA) 處理架構。PSA 可結合許多目前現有的子載波間干擾消除方法並且在不犧牲效能的情況下大幅地降低計算複雜度。搭配 PSA 以及擾動近似 (PB)，我們也

設計了新穎的迫零 (ZF) 和最小均方誤差 (MMSE) 等化器。而這些提出的等化器在效能和實現成本 (可節省 80% 計算量) 上取得了不錯的平衡，也因此特別適合用於 OFDMA 下行鏈路接受器。

從另外一方面來看子載波間干擾的問題，我們了解子載波間干擾是源自於通道的變化，進而認知到妥善運用此變化來獲取多樣性的可能性。結合了位元交織編碼調變 (BICM), BICM-OFDM 是一個非常有效的方式來獲得時間和頻率多樣性。再者，雙選擇性衰落通道可以提供顯著的多樣性。故本論文中，我們推導了在單輸入單輸出 (SISO) 和多輸入多輸出 (MIMO) 下漸進最大多樣性分析。我們進一步研究了在實際的狀況中，信噪比 (SNR) 非無限大時系統錯誤率曲線的行爲。我們發現在 SISO 情況下，多樣性多寡取決於通道相關矩陣的秩，因此因快速衰落所引起的通道變化將有助於增進多樣性。在 MIMO 的情況下，藉由使用循環延遲 (CDD) 以及相位混合 (PRD) 的技術，可更進一步提昇多樣性。

對於以上兩種方法，我們都提供了充足的模擬數據來驗證理論分析的正確性以及其對於效能上的改進效果。最後，我們也考慮了未來可能繼續探索的相關主題和方向。



BICM-OFDM Systems over Time-Varying Channels: ICI Cancellation and Diversity Order Analysis

Student: Hsin-De Lin

Advisors: Dr. Tzu-Hsien Sang

Dr. David W. Lin

Department of Electronics Engineering and Institute of Electronics
National Chiao Tung University, Hsinchu, Taiwan, Republic of China

Abstract

In high mobility scenarios, orthogonal frequency division multiplexing (OFDM) systems experience temporal channel variations within one symbol time to a degree resulting in that the orthogonality among subcarriers is destroyed by inter-carrier interference (ICI) and significant performance degradation may follow, if ICI is left untreated. This dissertation is concerned with the challenging problems caused by high mobility to advanced mobile communication systems that adopt orthogonal frequency-division multiple access (OFDMA) technologies where standard specifications and concerns about complexity demand low-cost methods with deployment readiness and decent performance. In this dissertation, comprehensive frameworks are provided to develop effective approaches for dealing with time-varying channels.

To fully understand the problems that fast channel variations may cause to OFDMA systems, fundamental properties and modeling issues of doubly selective fading channels are studied. A simple ICI indicator is devised to show the relative severity of ICI on subcarriers in OFDMA symbols, paving the way for efficient ICI cancellation strategies. Furthermore, a thorough analysis of the ICI indicator is provided to reveal the reasons why it works. It is shown that its probability density function (PDF) is determined by the moving speed meanwhile is insensitive to other factors such as channel power delay profiles and Doppler power spectra. As a result, the applicability of it to indicate channel variations is quite wide-range. Some possible applications of the ICI indicator are also discussed; in particular, its PDF provides valuable information, such as the maximum Doppler spread or the channel fading rate.

Equipped with the understanding of mechanism of ICI generation, two approaches to deal with the ICI issue are developed. In the first approach, with the help of

the ICI indicator, a per-subcarrier adaptive (PSA) framework which can work with a variety of existing ICI cancellation methods is proposed to greatly reduce computational complexity while maintaining performance. Novel zero forcing (ZF) and minimum mean-square error (MMSE) equalizers based on PSA processing and perturbation-based (PB) approximation are introduced. The proposed equalizers strike a good balance between performance and implementation cost (up to 80 % savings); therefore they are especially suitable for OFDMA downlink receivers.

The other approach to the ICI issue is, knowing it is a result of channel variation, to recognize the possibility of using it to gain diversity. Bit-interleaved coded modulation with OFDM (BICM-OFDM) is an attractive approach to achieve time and frequency diversity. Remarkable diversity gain can be obtained when the channel is doubly selective fading. In this dissertation, the asymptotic diversity orders of BICM-OFDM systems in doubly selective fading channels for both single-input-single-output (SISO) and multiple-input-multiple-output (MIMO) cases are derived. In addition, the system bit-error rate (BER) behavior in practical situations with moderate signal-to-noise ratios (SNRs) is also investigated. In the SISO case, the diversity order depends on the rank of the channel correlation matrix. Therefore, the channel variations induced by fast fading contributes to improving diversity. In the MIMO case, the diversity order can be further increased when factors like cyclic delays or phase rolls are introduced.

For both approaches, ample simulation evidences are provided to verify theoretical analysis and performance claims. Possible directions on related topics are also outlined for further exploration.

誌

謝

十數年的時間就這樣過去了，從大學、碩士到博士，感謝交通大學以及電子工程系，提供孕育我成長的良好風氣以及環境。

感謝指導教授桑梓賢博士，從碩士班時的啓蒙，讓我對研究有了起頭的興趣，想更進一步探其奧妙。在博士班的過程中，也非常幸運能夠遇見林大衛教授願意傾囊相授，其在學術涵養上之深厚，對於我的研究或是論文，總是能給出精闢的意見。和他們二位相處討論的過程中，除了研究上激發出許多想法，做人處世，甚至到人生的規劃，都給與我許多建議，既是良師也是益友。期許自己之後不忘他們的教誨，在通訊系統的領域上，能夠趕上他們的腳步，將來有任何一絲成就，都將歸功於兩位教授！

求學過程中，許多人給予過幫助，有崑健、俊榮以及海薇的陪伴以及討論。由於是桑梓賢老師所帶的第一位學生，許多學弟妹都曾一起討論，教學相長也讓我學到許多。感謝實驗室中的所有成員，特別是口試時，子傑、琬瑜、明孝以及其他學弟的幫忙。另外本論文部分想法，始於和陳俊才博士合作討論所萌芽，感謝他的幫忙。

感謝我的家人，父親林全盛以及母親尤麗環，對我從小細心地栽培，期許我能夠成長，在我追求學問的過程中除了支持還是支持，另外弟弟君育，生活上也幫我許多。他們爲了我能在求學中無後顧之憂，辛苦的付出我都記在心底，除了說一聲感謝，也希望這個博士學位能讓他們感受到一絲絲榮耀。

最後，最最感謝我的另一半，親愛的老婆盈潔，從大學開始交往到結婚，總是支持我的決定，每當我灰心想放棄時，她始終相信我鼓勵我。雖然在這個年紀，同儕在事業上都小有成就，或是結婚生子，進入人生另一階段，而我還是窩在學校，但她不埋怨計較，更以我爲榮。她的聰明以及智慧，在我念博士的過程中，給了無比的幫助，她也能夠輕而易舉地消弭我失意以及負面的情緒，進而轉化爲正面的力量。沒有她，我就不可能完成這個艱辛的過程，與她共享這個博士學位！

Table of Contents

中文摘要	ii
Abstract	iv
誌謝	vi
List of Tables	x
List of Figures	xi
Chapter 1 Background and Motivation	1
1.1 ICI Cancellation for OFDM-Based Systems	3
1.2 BICM-OFDM over Doubly Selective Fading Channels	5
1.3 Thesis Organization	7
Chapter 2 Doubly Selective Fading Channels	8
2.1 Baseband Equivalent Representation and Statistical Characterization	9
2.1.1 Channel Autocorrelation Functions and Power Spectra	11
2.2 Discrete Time Channel Model and Simulators	18
2.2.1 Discrete Time Model	18
2.2.2 Channel Simulators	20
2.3 OFDM Systems over Doubly-Selective Fading Channels	21
2.4 ICI Indicator	26
2.5 Applications of ICI Indicator	31
2.5.1 Estimation of Channel Variations	33
Chapter 3 ICI Cancellation	38
3.1 ICI Cancellation Techniques	40
3.1.1 Frequency Domain Approaches	40

3.1.2	Time Domain Approaches	42
3.1.3	Other Approaches	43
3.2	The Per-Subcarrier Adaptive ICI Cancellation Framework	44
3.2.1	Incorporate the MAP ICI Equalizer	48
3.3	Proposed Novel Low-Complexity ICI Equalizers	51
3.3.1	Perturbation-based ZF ICI Equalizer	51
3.3.2	Perturbation-based MMSE ICI Equalizer	54
3.3.3	ICI Indicator Threshold Setting	56
3.3.4	CFR Matrix Inversion by Lookup Table	58
3.4	Performance Results and Discussions	61
3.4.1	BER Simulations	61
3.4.2	Computational Complexity	65
Chapter 4	On the Diversity Order of BICM-OFDM Systems over Doubly Selective Fading Channels	68
4.1	Introduction	68
4.2	Diversity Order Analysis	71
4.2.1	System Model	71
4.2.2	Asymptotic Analysis	74
4.2.3	Practical Diversity Gains	77
4.2.4	Simulation Results and Discussions	80
4.3	Extension to the Multiple-Input Multiple-Output Case .	83
4.3.1	Cyclic Delay Diversity	83
4.3.2	Phase-roll Diversity	85
Chapter 5	Conclusion and Future Work	88
5.1	Future Work	89

Appendix I: Asymptotic Analysis on the Diversity Order of BICM-OFDM in Doubly Selective Channels	91
Appendix II: Regarding the Diversity Order From Intra-Symbol Channel Variations	96
References	99
Personal Resume	107



List of Tables

2.1	Time and Frequency Dispersion	14
2.2	Simulation Parameters	35
3.1	Computational complexity comparison.	51
3.2	Upper bound of ICI indicator, $10\log_{10}(\frac{ \Delta_k }{ H_k })$, given target residual ICI channel power levels and PB ICI equalizers	58
3.3	Complexity comparison.	65



List of Figures

1.1	Block diagram of a BICM-OFDM system.	3
2.1	PDP of IEEE 802.11n channel model B.	15
2.2	Channel frequency response of the PDP described in Fig. 2.1.	17
2.3	Path gain variations of ITU Vehicular-A channel with speeds at 2, 45, and 100 km/h.	18
2.4	Channel tap generation of sum-of-sinusoidals channel simulator.	20
2.5	Channel tap generation of filtering-based channel simulator.	21
2.6	Probability density functions (solid lines) and two histograms (dash lines for the ITU Vehicular-A channel and dots for two-path equal gain channel) of $10\log_{10}(\frac{\Delta_k}{H_k})$ for moving speeds at 60, 120 and 350 km/h. Bell-shape Doppler power spectrum and uncorrelated scattering are used.	28
2.7	Probability density functions (solid lines) and two histograms (dash lines for the flat Doppler spectrum and dots for the correlated scattering with correlation 0.7 between paths) of $10\log_{10}(\frac{\Delta_k}{H_k})$ for moving speed at 350 km/h. Two-path equal gain channel is used.	29
2.8	Normalized MSE versus SNR curves.	36
2.9	Mean of $ \Delta/H $ versus speed curves.	37
3.1	OFDMA frequency description of PUSC mode.	39
3.2	Block and serial approaches for ICI equalization.	44
3.3	The magnitude of the CFR matrix and cross-sections at selected sub-carriers.	46
3.4	This figure shows the percentages of $ \Delta_k/H_k $ that are larger than 0 dB or smaller than -5 dB at different vehicle speeds. Two channel PDPs, the ITU Pedestrian-B channel and the two-path equal-gain channel, are used.	47
3.5	A receiver adopting the PSA framework.	48
3.6	A banded CFR matrix with variable bandwidth Q	49
3.7	BER performance comparisons for MAP ICI equalizers under 1024-point FFT, QPSK and ITU Vehicular-A channel model at 500 km/h. The BER curves of the MAP ICI equalizer (solid lines) and the variable Q MAP ICI equalizer (dash lines) essentially overlap.	50

3.8	PB ICI equalizer block diagram.	53
3.9	SER performance versus $ \Delta_k/H_k $ at 10, 20 and 30 dB SNR.	56
3.10	Empirical probability density functions of α , β and γ for two different channel PDPs: the ITU Pedestrian-B channel and a two-path equal-gain channel.	59
3.11	Empirical probability density functions of α , β and γ for the ITU Pedestrian-B channel at two different vehicle speeds: 350 km/h and 60 km/h.	60
3.12	BER performance comparisons for ICI equalizers under 1024-point FFT, 16-QAM and the ITU Pedestrian-B channel model at 350 km/h and 60 km/h.	61
3.13	BER performance comparisons with -20 dB MSE channel estimation error at 350 km/h.	63
3.14	BER with different quantization levels LUT under the ITU Pedestrian-B channel at 350 and 60 km/h.	64
3.15	PER comparison for different $Q = 3, 4$ and 5 under the ITU Pedestrian-B channel at 350 km/h. 16-QAM and rate-3/4 CTC are used.	66
4.1	Block diagram of the transmitter and receiver of the considered system. Soft-input soft-output (Soft-in-Soft-out) demodulator consists of the ICI equalization such as the feedback canceller [1] and demapper.	72
4.2	BER performance with 8-PSK modulation under two-multipath ($L = 2$) Rayleigh block fading channels with two different path-gain distributions. The DFT size is 64, $P = 2$, and a rate-1/2 convolutional code with the generator polynomial [133; 171] ($d_{\text{free}} = 10$) is adopted. 10^5 channel realizations are simulated.	79
4.3	The eigenvalues are obtained by sampling the convolution of the Doppler spectrum and the sinc function in frequency domain which can be recognized as the observed Doppler spectrum. The curves show the effect of different window lengths.	80
4.4	Comparison of the diversity gain provided by time-varying channels with three kinds of Doppler power spectral density (PSD): Jakes' model, uniform PSD and carrier frequency offset (CFO). The normalized Doppler frequencies 0.01, 0.05 and 0.1 are simulated. The path gains $h_p(k; l)$ for different l are assumed independent. The time-variation of the channel $E[h_p(k; l)h_p^*(m; l')]$ is $J_0(2\pi f_d(k - m)T) \cdot \delta(l - l')$ for Jakes' model, $\sin(2\pi f_d(k - m)T)/(\pi(k - m)T) \cdot \delta(l - l')$ for uniform PSD and $\exp(j2\pi f_d(k - m)T) \cdot \delta(l - l')$ for CFO, where f_d is the maximum Doppler frequency, T is the OFDM sampling time, $J_0(\cdot)$ is the zeroth order Bessel function of the first kind, and $\delta(\cdot)$ is the Kronecker delta function. Notice that the considered diversity here is the effective diversity order based on the dominant eigenvalues.	82

- 4.5 BER comparison of the MIMO BICM-OFDM employing CDD, PRD and STBC over doubly-selective fading channels. The DFT size is 64, $P = 10$, and a rate-1/2 convolutional code with the generator polynomial [133; 171] ($d_{\text{free}} = 10$) is adopted. Notice that the considered diversity here is the effective diversity order based on the dominant eigenvalues. The channel is equal-gain two-path at $l = 0$ and $l = 1$ and the introduced cyclic delay Δ is 5. The parameters of PRD are chosen as $\varepsilon_1 = 0.05$ and $\varepsilon_2 = -0.05$ 86



Chapter 1 Background and Motivation

As mobile data traffic is exploding, many advances in the physical layer of mobile wireless communications have seen successful deployment in the last two decades. The data rate of the second generation (2G) digital wireless systems, e.g., Global System for Mobile Communications (GSM), is about 200 k bits-per-second (bps) and for which only the voice service is suitable. In the late 1990s, various standards have been proposed for 3G systems and the data rate is increased up to several Mbps. As wireless multimedia services become popular, the global data traffic has been doubling each year during the last few years and the 4G wireless standards such as IEEE's 802.16 family and the Long Term Evolution (LTE) by Third-Generation Partnership Project (3GPP) target to support hundreds of Mbps. To promote these standards, recently, a high mobility feature has been introduced to enable mobile broadband services at vehicular speeds up to 350 km/h and even 500 km/h, e.g., in high speed railways. However, the higher mobility the operating environment has, the larger Doppler frequency spread, which needs to be coped with, is introduced. In short, wireless communication faces the ever-increasing demand for higher data rates with more efficient spectrum usage while maintaining good quality of service in high motion speeds. Two transmission techniques that are very popular in that regard are bit-interleaved coded modulation (BICM) and orthogonal frequency-division multiplexing (OFDM). BICM counters fading channels by spreading codeword bits in time so as to exploit the time diversity available in the time-varying channel response [2,3], whereas OFDM claims high bandwidth efficiency and simplicity in receiver design.

Since OFDM has been recognized as an effective technique for high data rate communications and is robust to multipath delay spread (or frequency selectivity equiv-

alently) [4–6], advanced wireless standards such as worldwide interoperability for microwave access (WiMAX) and LTE both adopt orthogonal frequency-division multiple access (OFDMA) as their modulation schemes. High spectral efficiency in such systems is achieved by tightly squeezing subcarriers into a limited bandwidth [7]. This in turn implies that, when operating in a high-mobility scenario, for example on a high-speed vehicle, the channel exhibits fast fading and the signal experiences channel variation within one OFDMA symbol. This kind of channel is classified as doubly (time and frequency) selective fading channels. Consequently, the channel frequency response (CFR) matrix in the transmission model is no longer diagonal, and off-diagonal terms contribute to severe intercarrier interference (ICI) [8,9]. In other words, the orthogonality between subcarriers is destroyed. As a result, a serious performance degradation may ensue if ICI is left untreated [10,11].

In this dissertation, we consider the performance of BICM-OFDM systems over doubly-selective fading channels. As Fig. 1.1 shows, the receiver under consideration consists of inner and outer parts whereas the inner receiver is mainly for the compensating the impairments caused by the channel and demodulation while the outer receiver is responsible for channel-decoding. For the inner receiver, we focus on the ICI problem since it greatly affects the error rate performance. Furthermore, the methods for dealing with ICI is not limited to BICM-OFDM systems but for all OFDM-based systems. For the outer receiver, it is interesting to exploit the benefits provides by the time-varying characteristics for the BICM-OFDM systems.

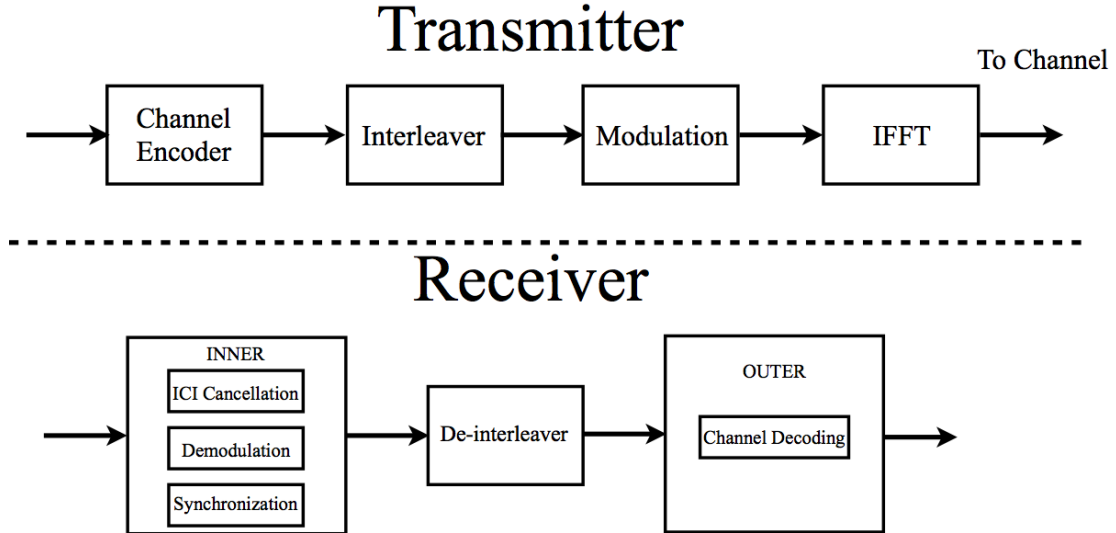


Figure 1.1: Block diagram of a BICM-OFDM system.

1.1 ICI Cancellation for OFDM-Based Systems

One approach to the ICI issue is to cancel it. ICI cancellation for OFDM/OFDMA systems in doubly selective fading channels has been an active research topic for many years. Well-known methods abound (please see [8–23] and references therein). Due to protocol constraints of industrial standards and implementation issues, linear ICI equalizations in the frequency domain is of particular interest and zero forcing (ZF) or minimum mean-square error (MMSE) ICI equalizers are proposed in [10,12,13,16]. For these methods, the major computational cost comes from matrix inversion. A common means to reduce the cost is to approximate the non-diagonal CFR matrix with a banded matrix in which all but few elements on selected $2Q + 1$ diagonals are set to zero [9,10,12,16,23]. With the banded structure, simpler matrix inversions are used to calculate MMSE or ZF ICI equalizer coefficients. A rule of thumb in choosing the bandwidth parameter Q is $Q \geq \lceil f_D/\Delta f \rceil + 1$, where f_D is the maximum Doppler frequency and Δf denotes the subcarrier spacing [9,16]. According to the rule, the choice of Q will be the same for a wide range of maximum Doppler frequency, for

example, in WiMAX $Q = 2$ for vehicle speeds at 60, 350, and 500 km/h. However, the BER performance can degrade severely when Q is not large enough. On the other hand, a large Q may only yield slight performance gain yet induce high complexity. Other than computational cost, features specified in advanced systems that were derived from mobile WiMAX (IEEE 802.16e) [7] and LTE can also impose serious difficulties on engineering development which will be discussed in detail later. Therefore, there is a strong motivation to seek possible improvement on conventional ICI equalizers to strike a right balance between performance and implementation complexity.

Based on empirical observations, we found that each subcarrier faces very different ICI situations and thus, there is no uniform band structure in the CFR matrix, i.e., fixed Q for every subcarrier. We introduce an useful measure called ICI indicator that can be used to indicate the relative degree of channel variation (or equivalently the ICI level) on individual subcarriers [24,25]. With the proposed ICI indicator, appropriate Q 's can be chosen for each subcarrier that also motivates to use different ICI cancellation strategies on different subcarriers according to the ICI situation (called per-subcarrier adaptive (PSA) ICI cancellation framework), say, simple ICI cancellation for subcarriers experiencing mild ICI and heavy ICI cancellation for severe ICI. Moreover, as for the standard's constraints and implementation readiness, the perturbation-based (PB) linear ICI equalizers that can be realized as finite-impulse response (FIR) filters are proposed. A much better trade-off between BER performance and computational complexity (up to 80 % savings) can be achieved.

We also provide a thorough analysis of the ICI indicator to reveal why it works and consider some possible applications. Collectively, the probability density function (PDF) of the ICI indicator provides valuable information, such as the maximum Doppler spread or the channel fading rate. Statistical analysis shows that its PDF

is only determined by the moving speed in the channel model, and is insensitive to channel power delay profiles and Doppler power spectra. Therefore, this indicator is applicable in a wide range of situations of interests.

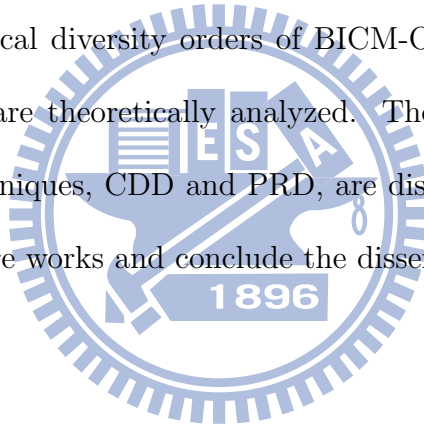
1.2 BICM-OFDM over Doubly Selective Fading Channels

Another approach to the ICI issue is, knowing it is a result of channel variation, to recognize the possibility of using it to gain diversity. Wireless communications face fading channels and robust data reception is always challenging. One of the most effective fading countermeasures is using the diversity techniques to exploit available diversity gain offered by the channel. By introducing a bit interleaving between the channel encoder and mapper, BICM was first proposed by Zehavi in [26] and then comprehensively investigated by Caire *et al.* [2]. A further development, BICM with iterative decoding (BICM-ID), is proposed by Li *et al.* [3]. The diversity order of BICM in flat fading channels is found to be the minimum number of distinct bits in two different code sequences and can be very high in a properly design BICM system. A lot of literatures about BICM deal with the flat fading channels; therefore, only temporal diversity is utilized. For the purpose to exploit frequency diversity as well, the combination of OFDM and BICM, called BICM-OFDM, over frequency selective fading channels is an attractive option. It is shown to achieve the maximum diversity order inherent in such channel [27]. Since many existing and future wireless standards employ bit-level interleaver and channel coding, e.g., WiFi, DVB, WiMAX, LTE and LTE-advanced, they can be considered and analyzed as BICM.

Doubly selective fading channels in many situations have been viewed as the cause of severe channel impairments such as ICI, it is also considered as a potential source of time and frequency diversity which may enhance the system performance. Compared to the performance with quasi-static channels, utilizing the ICI terms at the receiver may actually improve the error rate and simulation results also reveal that the performance gain comes from increasing diversity [9,12,28]. Pioneering work by Ma and Giannakis [29] considers the maximum diversity order over doubly selective channels for general block transmission systems without forward error correction (FEC). Recent papers start investigating time diversity for coded OFDM systems. Huang and others [1,18] reported that, in simulations the performance of BICM-OFDM systems is improved when the channel is fast fading. In [27], the diversity order of BICM-OFDM systems in frequency selective fading channels is analyzed. For BICM-OFDM systems, a theoretical analysis of the diversity order over doubly selectively fading channels has not appeared in the literature. It motivates us to provide such analysis and the maximum diversity order of BICM-OFDM over doubly selective fading channels is derived. First, we derive the asymptotic diversity order of BICM-OFDM systems by studying the role of correlation in rank analysis of the typical derivation of diversity order. The results also show that BICM-OFDM achieves the maximum diversity order given in [29]. Second, the effect of significant eigenvalues of the channel correlation matrix and the diversity order in realistic situations with moderate SNRs are examined by studying the channel correlation function and its Fourier dual. Finally, our analysis framework is extended to multiple input multiple output (MIMO) cases while incorporating more diversity techniques, such as cyclic delay diversity (CDD) and phase-roll diversity (PRD) [30]. This MIMO extension can also be applied in a distributed fashion, for example, in cooperative communications [31].

1.3 Thesis Organization

This dissertation is organized as follows. In Chapter 2, we give an extensive review of the doubly selective fading channels including the statistical characterization, discrete time model and generating approaches for computer simulations. With the development of system model of OFDM systems over doubly selective fading channels, a novel ICI indicator is introduced and the statistical analysis as well as possible applications of the ICI indicator are given. Chapter 3 discusses the ICI cancellation and introduces the PSA framework. The PSA PB-ZF and PB-MMSE ICI equalizers that consider the standard constraints and are suitable for implementation are presented. In Chapter 4, the asymptotic and practical diversity orders of BICM-OFDM systems over doubly-selective fading channels are theoretically analyzed. The analysis can be extend to MIMO cases and two techniques, CDD and PRD, are discussed. Finally, we consider possible directions of future works and conclude the dissertation in Chapter 5.



Chapter 2

Doubly Selective Fading Channels

Wireless communication often encounters environments with rich multipaths because of the atmospheric scattering and refraction, or reflections of surrounding objects. Traveling through these paths, the signals arrived at the receiver with random delays and attenuations will be added constructively or destructively and result in envelope fluctuations significantly, which is referred to *fading*. Furthermore, in high data rate wide-band systems, e.g., OFDM, the bandwidth of the transmitted signal is larger than the coherence bandwidth of the fading channel, giving rise to frequency-selectivity of fading channels. It becomes clear that emerging mobile applications will experience channel variations within one symbol time where the channel is said to be time-selective. This is mainly due to the changing atmospheric conditions and relative movements between transmitters and receivers. Consequently, the wireless channel of mobile communications is characterized as a time- and frequency-selective (or doubly-selective) fading channel. As these selectivities affect the system performance critically, the understanding and modeling of doubly-selective fading channels are important tasks for devising countermeasures.

A precise mathematical description of fading channels, i.e., the physical modeling based on electromagnetic radiation [32], for practical scenarios is either unknown or too complex to be tractable. However, considerable efforts have been devoted to the statistical modeling. Moreover, statistical descriptions could provide insights in many typical issues, e.g., the proper packet duration to avoid fades, the relative severity of experienced ISI/ICI, the appropriate subcarrier spacing for frequency diversity, the

necessary interleaving depth for time diversity, expected BER, etc..

In this chapter, we first consider the statistical characterization of doubly-selective fading channels. Then, the discrete-time channel model will be developed and channel simulators for computer simulations will be introduced. As OFDM has become the de facto transmission scheme in modern wireless communications, we consider the system model for OFDM over doubly-selective fading channels where ICI exists. Based on empirical observations, a measure called the ICI indicator was introduced to indicate the ICI level as well as to estimate the maximum Doppler frequency on each subcarrier. We also provide a thorough analysis of the ICI indicator to reveal why it works. Collectively, its PDF also provides valuable information on, for example, the maximum Doppler spread. Some applications of the ICI indicator are given.

2.1 Baseband Equivalent Representation and Statistical Characterization

Assume there exist multiple propagation paths, $\alpha_n(t)$ is the attenuation factor for the signal received on the n -th path, and $\tau_n(t)$ is the propagation delay of the n -th path. The bandpass received signal through discrete multipath channels in the absence of noise can be expressed in the form

$$y(t) = \sum_n \alpha_n(t)x(t - \tau_n(t)) \quad (2.1)$$

where $x(t)$ is the bandpass transmit signal.

Using the complex envelope and expressing $x(t)$ as $\text{Re}[x_{\text{bb}}(t)e^{j2\pi f_c t}]$ where $x_{\text{bb}}(t)$ is the baseband equivalent transmit signal and f_c is the central carrier frequency, we can carry out analysis and simulation of carrier-modulated (bandpass) signals and systems

at baseband. Equation (2.1) can be re-written as

$$y(t) = \text{Re}\left[\sum_n \alpha_n(t) e^{-j2\pi f_c \tau_n(t)} x_{\text{bb}}(t - \tau_n(t))\right] e^{j2\pi f_c t}. \quad (2.2)$$

From the above expression it is straightforward to write the baseband equivalent (or lowpass equivalent) signal as

$$y_{\text{bb}}(t) = \sum_n \alpha_n(t) e^{-j2\pi f_c \tau_n(t)} x_{\text{bb}}(t - \tau_n(t)). \quad (2.3)$$

By transmitting a conceptually ideal impulse, the complex baseband equivalent time-varying channel impulse response (CIR) is obtained as

$$\begin{aligned} c(t; \tau) &= \sum_n \alpha_n(t) e^{-j2\pi f_c \tau_n(t)} \delta(t - \tau_n(t)) \\ &= \sum_n \tilde{\alpha}_n(t; \tau) \delta(t - \tau_n(t)) \end{aligned} \quad (2.4)$$

where $\delta(\cdot)$ denotes the Dirac delta function.

For another type of channel model, the diffuse multipath channel, the signal is composed of a continuum of unresolvable components and is expressed in the integral form

$$y(t) = \int_{-\infty}^{\infty} \alpha(t; \tau) x(t - \tau) d\tau \quad (2.5)$$

where $\alpha(t; \tau)$ denotes the attenuation of the signal at delay τ and at time instant t . Following the similar procedures as in the case of discrete multipath channels, the CIR can be expressed by

$$c(t; \tau) = \alpha(t; \tau) e^{-j2\pi f_c \tau}. \quad (2.6)$$

In Equation (2.4), the channel fading is described by time variations in the magnitudes and phases of $c(t; \tau)$. These variations appear to be random and usually are treated as random processes. If there are numerous propagation paths, which usually is the case of wireless channels, we can model the CIR $c(t; \tau)$ as a complex-valued

Gaussian random process by the central limit theorem. When the CIR is zero-mean, the envelope $r = |c(t; \tau)|$ is Rayleigh-distributed that has the form [33]

$$f_R(r|\sigma^2) = \frac{r}{\sigma^2} e^{-r^2/(2\sigma^2)}, \quad r \geq 0 \quad (2.7)$$

and it is called the Rayleigh fading channel. This kind of simplification often applies to the non-light-of-sight (NLOS) case. When there is a direct-link between the transmitter and the receiver, i.e., the LOS case, the CIR cannot be modeled as zero-mean, and the channel is often modeled by Ricean fading following the PDF [33]

$$f_R(r|\nu, \sigma^2) = \frac{r}{\sigma^2} e^{-(r^2+\nu^2)/(2\sigma^2)} I_0\left(\frac{r\nu}{\sigma^2}\right), \quad r \geq 0 \quad (2.8)$$

where $I_0(\cdot)$ is the zero-th order modified Bessel function of the first kind. When $\nu = 0$, which means the power of the LOS path is zero, the distribution reduces to a Rayleigh distribution.

As the basic Rayleigh/Ricean model gives the PDF of the channel envelope, we now consider the question of how fast the signal fades in time and frequency. To answer the question, we need further characterize the CIR by its autocorrelation function and power spectral density (PSD); together they form a Fourier transform pair [33].

2.1.1 Channel Autocorrelation Functions and Power Spectra

Autocorrelation Functions

We assume $c(t; \tau)$ is wide-sense-stationary (WSS) and define the autocorrelation function of $c(t; \tau)$ as

$$R_c(\Delta t; \tau_1, \tau_2) = E[c(t; \tau_1)c^*(t + \Delta t; \tau_2)]. \quad (2.9)$$

In most cases, the attenuation and phase shift at the delay τ_1 path is uncorrelated with that at τ_2 , which is known as *uncorrelated scattering* (US). With the WSSUS condition,

(2.9) can be decoupled into

$$R_c(\Delta t; \tau_1, \tau_2) = R_c(\Delta t; \tau_1)\delta(\tau_2 - \tau_1). \quad (2.10)$$

Notice that $R_c(0; \tau) \triangleq R_c(\tau)$ is called the *power delay profile* (PDP); the range of τ within which $R_c(\tau)$ is non-zero is termed the maximum delay spread of the channel and is denoted as T_m .

PDP describes the average received power as a function of delay and is one of the most important parameters for channel modeling. We will see later that many industrial standards specify PDPs in their testing environments. PDP can be measured by probing the channel with a wideband radio-frequency (RF) waveform that is generated by modulating a high-rate pseudo-noise (PN) sequence. By cross correlating the receiver output against delayed versions of the PN sequence and measuring the average value of the correlator output, one can obtain the power versus delay profile. Just like there are many equally valid definitions of bandwidth, other useful measurements of the delay spread are possible. One of them is the root-mean-square (RMS) delay spread, which is defined by

$$T_{\text{RMS}} = \sqrt{\frac{\int \tau^2 R_c(\tau) d\tau}{\int R_c(\tau) d\tau} - \left(\frac{\int \tau R_c(\tau) d\tau}{\int R_c(\tau) d\tau}\right)^2}. \quad (2.11)$$

Now consider channel characterizations in the frequency domain. By taking the Fourier transform of $c(t; \tau)$ w.r.t. the variable τ , the time-variant channel frequency response is

$$C(t; f) = \int_{-\infty}^{\infty} c(t; \tau) e^{-j2\pi f\tau} d\tau. \quad (2.12)$$

Similarly, we can define the autocorrelation function of $C(t; f)$ as

$$R_C(\Delta t; f_1, f_2) = E[C(t; f_1)C^*(t + \Delta t; f_2)]. \quad (2.13)$$

Relating (2.13) to (2.10), it can be shown that

$$R_C(\Delta t; f_1, f_2) = \int_{-\infty}^{\infty} R_c(\Delta t; \tau_1) e^{-j2\pi\Delta f\tau_1} d\tau_1 \quad (2.14)$$

$$\triangleq R_C(\Delta t; \Delta f)$$

where $\Delta f = f_2 - f_1$. Equation (2.14) describes the autocorrelation function in the frequency variable. Moreover, the range of Δf within which the components of $R_C(\Delta f)$ are highly correlated is defined as the *coherence bandwidth* of the channel and denoted as $(\Delta f)_c$. As $R_c(\Delta t; \tau_1)$ and $R_C(\Delta t; \Delta f)$ form a Fourier transform pair, a very rough relation is that the coherence bandwidth is reciprocally proportional to the maximum delay spread [33]

$$(\Delta f)_c \approx \frac{1}{T_m}. \quad (2.15)$$

If the signal bandwidth is large compared to the channel's coherence bandwidth, the signal will be distorted and the channel is called frequency-selective. This is equivalent to the case where the delay spread is larger than the symbol time, which is also termed time-dispersion because transmitting an ideal impulse through the channel will yield a receive signal with several delayed pulses. In this case, the interference among different symbols occur and called inter-symbol interference (ISI).

Power Spectral Density

Now, we consider the time variations of the channel and investigate the Fourier transform pair

$$S_C(\lambda; \Delta f) = \int_{-\infty}^{\infty} R_C(\Delta t; \Delta f) e^{-j2\pi\lambda\Delta t} d\Delta t. \quad (2.16)$$

If Δf is set to 0, $S_C(\lambda)$ is called the channel's Doppler PSD and λ represents the Doppler frequency. The range of λ within which $S_C(\lambda)$ is non-zero is termed the maximum Doppler spread of the channel and is denoted as f_D . The maximum Doppler

Table 2.1: Time and Frequency Dispersion

	Time Dispersion	Frequency Dispersion
Time Domain	Delay spread	Time selective fading (fast fading)
Interpretation	ISI	Coherence time
Frequency Domain	Frequency selective fading	Doppler spread
Interpretation	Coherence bandwidth	ICI

frequency can be roughly calculated by

$$f_D = \frac{vf_c}{c} \quad (2.17)$$

with v being the mobile speed and c the speed of light. Similarly, the range of Δt within which the components of $R_C(\Delta t)$ are highly correlated is defined as the channel's *coherence time* and is denoted as $(\Delta t)_c$. Again, because they form a Fourier transform pair, the maximum Doppler spread and the coherence time are reciprocally related via

$$(\Delta t)_c \approx \frac{1}{f_D}. \quad (2.18)$$

Similarly, if the signal duration is large compared to the channel's coherence time, the channel is called time-selective. This is equivalent to the case where the Doppler spread is large enough, and a pure-tone transmit signal passing through the channel will yield a receive signal with several frequency components; we call this phenomenon frequency-dispersion. The terminologies and their relationships are summarized in the Table 2.1.

To relate the parameters τ , λ , Δf , and Δt , we define the scattering function of the channel

$$S_{sc}(\lambda; \tau) = \int_{-\infty}^{\infty} R_C(\Delta t; \Delta f) e^{-j2\pi\lambda\Delta t} e^{j2\pi\tau\Delta f} d\Delta t d\Delta f, \quad (2.19)$$

which is the double Fourier transform of $R_C(\Delta t; \Delta f)$.

Jakes' model is widely adopted to describe the time variation of the mobile radio channels with the the corresponding autocorrelation function

$$R_C(\Delta t) = J_0(2\pi f_D \Delta t) \quad (2.20)$$

where $J_0(\cdot)$ is the zero-th order Bessel function of the first kind. The Doppler PSD is obtained by Fourier transform, that is

$$\begin{aligned} S_C(f) &= \int_{-\infty}^{\infty} J_0(2\pi f_D \Delta t) d\Delta t \\ &= \frac{1}{\pi f_D \sqrt{1 - (f/f_D)^2}}, \text{ if } |f| \leq f_D \end{aligned} \quad (2.21)$$

and zeros elsewhere.

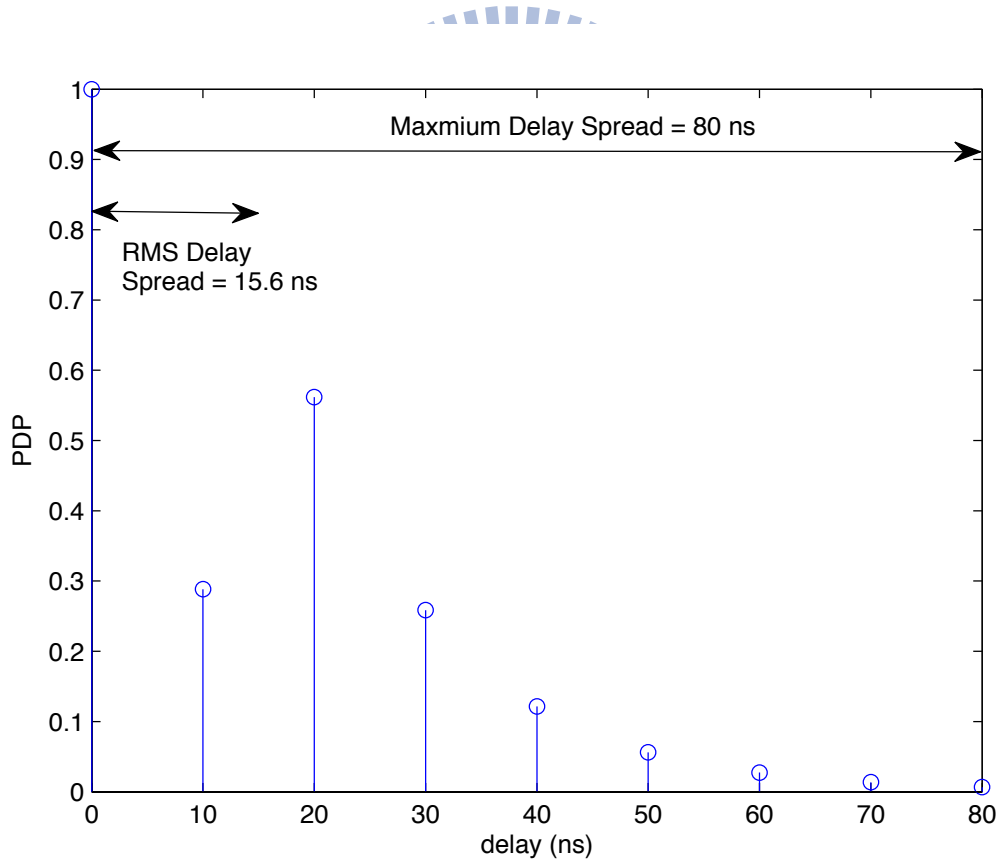


Figure 2.1: PDP of IEEE 802.11n channel model B.

Here we give some examples of the statistical channel parameters in practical systems. For the Wireless Local Area Network (WLAN), which is usually used in the

indoor, there are five channel models proposed by the IEEE 802.11 a/n standard [34] where the RMS delay spreads are about 0 ns to 150 ns depending on the scenarios, and the Doppler power spectrum is Bell-shaped, specified by

$$S_C(f) = \frac{1}{1 + A\left(\frac{f}{f_D}\right)^2}. \quad (2.22)$$

Fig. 2.1 shows the PDP of the IEEE 802.11n channel B whose the maximum delay spread is 80 ns and the RMS delay spread is 15.6 ns. According to (2.15), the coherence bandwidth is around 12.5 MHz. The channel frequency response is shown in Fig. 2.2 and it can be seen that the signal with 20 MHz bandwidth experience frequency-selectivity while the CFR varies slow within 5 MHz and thus the channel of the signal with 5 MHz bandwidth can be considered as flat-fading. However, since the application is in indoor, the mobility is very small and the channel varies very slowly so we demonstrate the Doppler effect in the following example.

For the wireless Metropolitan Area Network (MAN), e.g., IEEE 802.16e, the International Telecommunication Union (ITU) channel models are adopted where the RMS delay spreads for outdoor scenarios are around 2 us to 20 us, much longer than that of WLAN scenarios. The Jakes' U-shape Doppler spectrum is assumed and the typical maximum Doppler spreads at 2.5 GHz carrier frequency are 4.6, 104.2, and 231.5 Hz corresponding to the speed of 2, 45, and 100 km/h, respectively. The corresponding coherence time is 200, 10, and 4 ms, respectively. Fig. 2.3 shows the path gain variations of ITU Vehicular-A channel and it can be seen that higher speeds result in faster channel variations. In IEEE 802.16e, the symbol duration is around 100 μ s so that even at 100 km/h the channel still can be considered as linearly time-varying within one symbol.

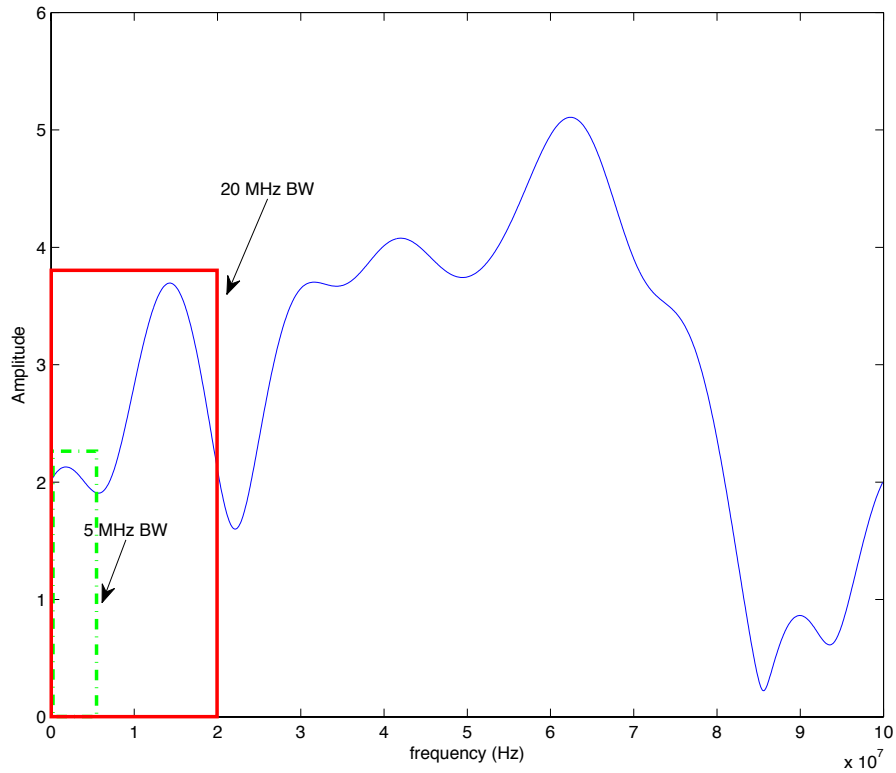


Figure 2.2: Channel frequency response of the PDP described in Fig. 2.1.

Large-scale versus small-scale fading

It is worthwhile to mention that channel fading can also be categorized into large-scale and small-scale fading [32]. While we have discussed the causes and effects of small-scale fading in the above, the large-scale fading is caused by propagation loss over long distance and by shadowing due to obscuring objects that attenuate the received signal strength. Since large-scale fading varies much slower compared to small-scale fading and the induced issues are more related to cell planning and receivers' sensitivity, in this dissertation we only focus on small-scale fading caused by multipath propagation.

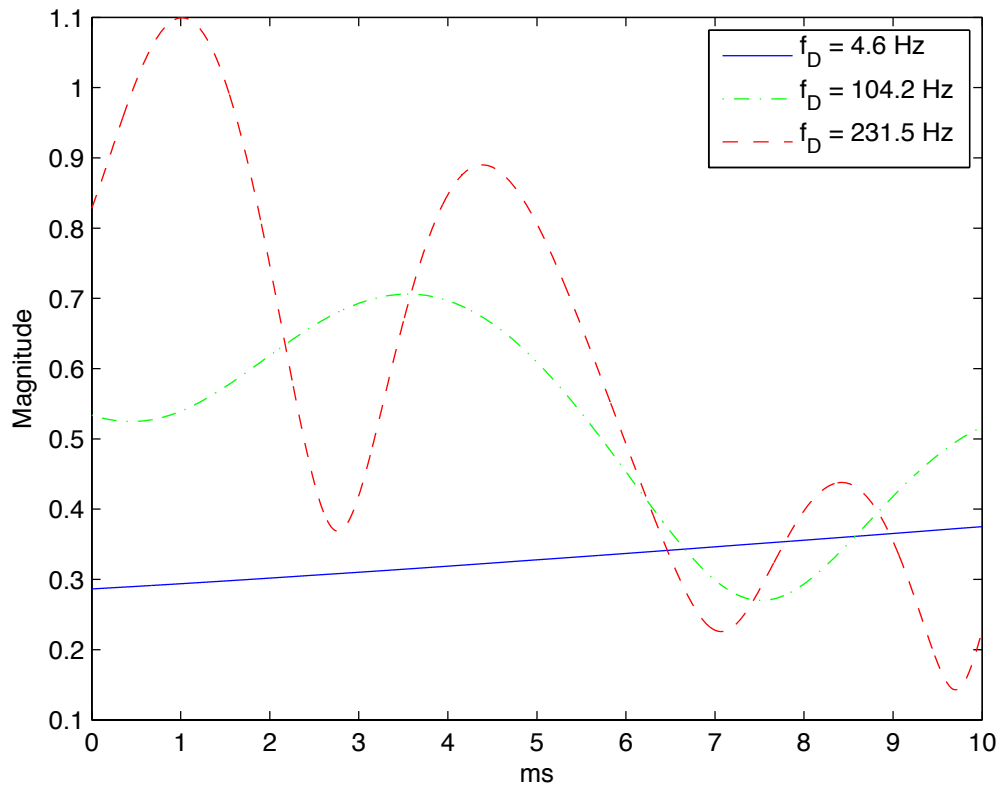


Figure 2.3: Path gain variations of ITU Vehicular-A channel with speeds at 2, 45, and 100 km/h.

2.2 Discrete Time Channel Model and Simulators

It has been shown that both PDP and Doppler PSD are effective tools to characterize wireless channels, we now consider the problem of how to efficiently generate channels for computer simulations. We focus on Rayleigh fading since the Ricean model can be obtained from the Rayleigh model by adding a non-zero mean.

2.2.1 Discrete Time Model

For most time the input-output relationship can be modeled as a linear time-varying system. The continuous time model often is not suitable for simulations because of

the intensive computational complexity due to very high oversampling. It has been shown that using discrete time representation realized by a tapped delay line model with time-variant tap gains is usually good enough for simulation purposes.

Let $p_T(t)$ and $p_R(t)$ be the time-invariant impulse response of the transmit filter and the receive filter, respectively, and both are normalized with unit energy. At the receiver, the resulting channel will have the combined impulse response as

$$h(t; \tau) = p_R(\tau) \odot c(t; \tau) \odot p_T(\tau) \quad (2.23)$$

where $a(\tau) \odot b(t; \tau) = \int b(t; \tau')a(\tau - \tau')d\tau'$ denotes the convolution operation. We consider typical digital communication where the transmit sequence $s(l)$ consists of complex symbols with the symbol time equals to T_{sym} . By replacing (2.4) with (2.23) and using (2.3), the baseband equivalent received signal $y(t)$ can be expressed by

$$y(t) = \sum_l x(l)h(t; t - lT_{\text{sym}}) \quad (2.24)$$

where the subscript _{bb} in (2.3) is omitted for brevity unless stated otherwise since we are concerned with the baseband equivalent model throughout most part of this dissertation.

The sampled version of $y(t)$ with the sampling period T_s is given by

$$y(kT_s) = \sum_l x(l)h(kT_s; kT_s - l\gamma T_s) \quad (2.25)$$

where γ is an integer oversampling factor and $T_s = T_{\text{sym}}/\gamma$. For considering RF- or analog-related effects, it may require oversampling, e.g., $\gamma = 2, 4, \dots$. If oversampling is used, the data sequence $\{x(k)\}$ should also be oversampled by inserting $(\gamma - 1)$ zeros between each symbol $x(k)$. It can be shown that the symbol-spaced model contains sufficient statistics for data detection if the transmit and receiver filters are carefully chosen, i.e., fulfilling the Nyquist condition. Consequently, we consider the the case $\gamma = 1$ and, thus, T_s can be dropped for brevity.

2.2.2 Channel Simulators

As the discrete time channel model in Equation (2.25) acts as an FIR time-varying filter, the problem is transformed to generating the tap gains for simulations. We consider two well-known methods: the first is to generate and combine several complex exponentials, and thus is properly termed sum-of-sinusoidal; the second is to generate a Gaussian random sequence and passing the sequence through an FIR filter with the transfer function designated to be the square-root of the required Doppler PSD.

Simulation Methods I: Sum-of-sinusoidals

The sum-of-sinusoidals is proposed by Jakes [35]:

$$h(k; l) = \frac{\sigma_l}{\sqrt{N_{\text{path}}}} \sum_{n=1}^{N_{\text{path}}} e^{j(\theta_n - 2\pi\lambda_n k T_s)} \quad (2.26)$$

where σ_l denotes the tap gain of the l -th path and θ_n are i.i.d. random variables with uniform distribution over the range of 0 to 2π . A small number of N_{path} , say, $N_{\text{path}} = 10$, will approximate Rayleigh fading quite accurately. The block diagram of the channel tap generation process is shown in Fig. 2.4.

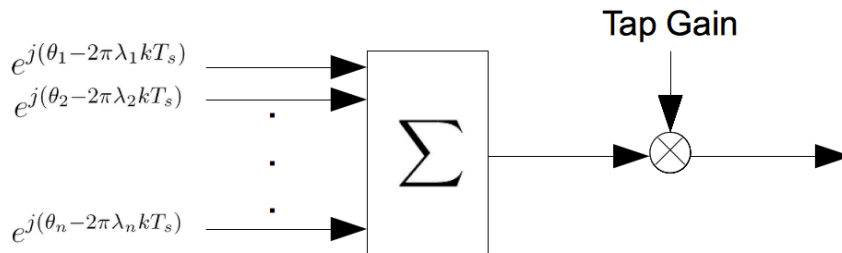


Figure 2.4: Channel tap generation of sum-of-sinusoidals channel simulator.

Simulation Methods II: Filtering

Another approach to simulate the tap gains with desired PDP and Doppler spectrum is [36,37]: first generate a complex white Gaussian random sequence; second, input the generated sequence to an FIR filter with the square root of the desired Doppler PSD as its transfer function; finally, properly scale the corresponding filter tap to follow the desired PDP. The block diagram of the channel tap generation process is shown in Fig. 2.5.

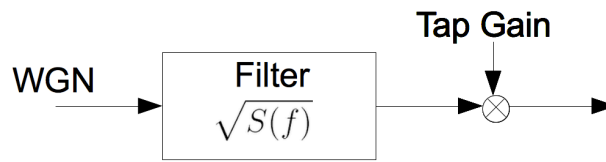


Figure 2.5: Channel tap generation of filtering-based channel simulator.

Both methods have their advantages and disadvantages. The filtering-based approach has accurate statistics but usually requires high computational complexity. Furthermore, the Doppler spectrum usually is discontinuous at the maximum Doppler frequencies and it makes the corresponding FIR filter to be very long. The statistics associated with the sum-of-sinusoidal approach may not be what we expect and some techniques have been proposed to improve the accuracy [38–40].

2.3 OFDM Systems over Doubly-Selective Fading Channels

OFDM is a promising transmission technique to achieve high data rates over wireless mobile channels. Besides bandwidth efficiency, OFDM offers many advantages over conventional single carrier systems, for example, robustness against multipath delay

spread, all-digital-FFT implementation, the possibility of adaptive channel allocation and adaptive modulation of the subcarriers for maximizing the capacity [41]. Thanks to cyclic prefix (CP), the ISI can be avoided, and the channel effect can easily be compensated by applying one-tap frequency domain equalizers since the frequency selective fading channel is transformed into parallel flat fading channels. However, if there exists channel variations within one OFDM symbol will introduce interferences among subcarriers, called ICI. OFDM is vulnerable to ICI due to tightly spacing between subcarriers.

Consider the baseband equivalent OFDM system model with N subcarriers. By doing N -point IDFT of the data sequence of the OFDM symbol, $\{S(m)\}$, the time-domain transmitted signal $x(k)$ at the k -th time instant can be written as

$$x(k) = \frac{1}{N} \sum_{m=0}^{N-1} S(m) e^{j \frac{2\pi m k}{N}}, \quad k = 0, 1, \dots, N-1. \quad (2.27)$$

Assume a CP with length of N_{CP} longer than the maximum delay spread of the channel, denoted as L ; the total length of a transmitted OFDM symbol is $N_S = N + N_{CP}$. Let $h(k; l)$ represent the l -th delay path of the time-varying dispersive channel impulse response at the k -th sampling instant. The channel path $\{h(k; l)\}$ is assumed to follow the WSSUS model, i.e., $E[h(k; l)h^*(k; l+l')] = \sigma_l^2 \xi_{l'}$ where $\xi_{l'}$ denotes the 1-D Kronecker delta and σ_l^2 is the average power of the l -th path. Assuming CP removal and perfect synchronization, the sampled baseband equivalent received signal $y(k)$ of the OFDM symbol can be expressed as [9,10]

$$y(k) = \sum_{l=0}^{L-1} h(k; l)x(k-l) + n(k), \quad 0 \leq k \leq N-1 \quad (2.28)$$

where $n(k)$ is the additive white Gaussian noise.

Taking discrete Fourier transform of Equation (2.28), the frequency-domain re-

ceived signal on the i -th subcarrier is

$$\begin{aligned}
R(i) &= \sum_{k=0}^{N-1} y(k) e^{-\frac{j2\pi ki}{N}} \\
&= \sum_{k=0}^{N-1} \left(\sum_{l=0}^{L-1} h(k;l) x(k-l) + n(k) \right) e^{-\frac{j2\pi ki}{N}} \\
&= \sum_{k=0}^{N-1} \left(\sum_{l=0}^{L-1} h(k;l) \left(\frac{1}{N} \sum_{m=0}^{N-1} S(m) e^{\frac{j2\pi m(k-l)}{N}} \right) + n(k) \right) e^{-\frac{j2\pi ki}{N}} \\
&= \sum_{m=0}^{N-1} S(m) H_{i,m} + Z(i)
\end{aligned} \tag{2.29}$$

where

$$H_{i,m} = \frac{1}{N} \sum_k H(m;k) e^{-\frac{j2\pi k(i-m)}{N}} \tag{2.30}$$

and

$$H(m;k) = \sum_l h(k;l) e^{-\frac{j2\pi lm}{N}}. \tag{2.31}$$

Note that $H(m;k)$ can be interpreted as the CFR on the m -th subcarrier at the k -th time instant. The ICI on the i -th subcarrier which is caused by the signal on the m -th subcarrier comes through the ICI channel $H_{i,m}$.

Assume that the time variation of CIR is linear within one OFDM symbol [13,15]. It is a reasonable assumption in most practical cases when the normalized Doppler frequency (normalized to subcarrier spacing) is smaller than 0.1, which corresponds to 500 km/h in WiMAX standard. The CIR of the p -th OFDM symbol can be written as

$$h(pN_S - N + k; l) = h\left(pN_S - \frac{N-1}{2}; l\right) + \frac{k - \frac{N-1}{2}}{N_S} \delta(pN_S; l) \tag{2.32}$$

where N_S denotes the length of CP plus N . $h(pN_S - \frac{N-1}{2}; l)$ represents the center point of the p -th OFDM symbol and $\delta(pN_S; l)$ is the slope of the l -th channel path at the p -th OFDM symbol. Note that with the linear variation assumption the channel at the center point is also the averaged channel in one OFDM symbol.

From (2.27) and (2.28), the received signal can be compactly expressed in vector

form as

$$\mathbf{y} = \mathbf{H}_t \mathbf{F}^H \mathbf{x} + \mathbf{n} \quad (2.33)$$

where $\mathbf{y} = [y(0), y(1), \dots, y(N-1)]^T$, $[\mathbf{H}_t]_{k,l} = h(pN_S - N + k; (k-l) \bmod N)$ denotes the CIR matrix, $[\mathbf{F}]_{m,n} = (1/\sqrt{N})e^{-j2\pi mn/N}$ is the N -point DFT matrix, $\mathbf{s} = [S(0), S(1), \dots, S(N-1)]^T$, and $\mathbf{n} = [n(0), n(1), \dots, n(N-1)]^T$.

Using (2.32), the CIR matrix in (2.33) can be decomposed as

$$\mathbf{H}_t = \mathbf{M}_t + \boldsymbol{\psi} \mathbf{D}_t \quad (2.34)$$

where $[\mathbf{M}_t]_{k,l} = h(pN_S - \frac{N-1}{2}; (k-l) \bmod N)$ and $[\mathbf{D}_t]_{k,l} = \delta(pN_S; (k-l) \bmod N)$ for $k, l = 0, 1, \dots, N-1$. \mathbf{M}_t and \mathbf{D}_t both are circulant matrices. The matrix $\boldsymbol{\psi}$ is diagonal and defined as $\boldsymbol{\psi} = \frac{1}{N_S} \text{diag}([- \frac{N-1}{2}, - \frac{N-1}{2} + 1, \dots, \frac{N-1}{2}]^T)$. Note that $h(pN_S - \frac{N-1}{2}; l)$ and $\delta(pN_S; l)$ are assumed to be zero when $l \leq 0$ or $l \geq L-1$.

Substituting (2.34) into (2.33) and applying DFT matrix to \mathbf{y} , the received signal $\mathbf{r} = [R(0), R(1), \dots, R(N-1)]^T$ in the frequency domain is given by

$$\begin{aligned} \mathbf{r} = \mathbf{F} \mathbf{y} &= \underbrace{\mathbf{F} \mathbf{M}_t \mathbf{F}^H}_{\equiv \mathbf{H}_{avg}} \mathbf{s} + \underbrace{\mathbf{F} \boldsymbol{\psi} \mathbf{F}^H}_{\equiv \mathbf{G}} \underbrace{\mathbf{F} \mathbf{D}_t \mathbf{F}^H}_{\equiv \boldsymbol{\Delta}} \mathbf{s} + \mathbf{F} \mathbf{n} \\ &= \mathbf{H}_{avg} \mathbf{s} + \underbrace{\mathbf{G} \boldsymbol{\Delta} \mathbf{s}}_{\text{ICI}} + \mathbf{z} \end{aligned} \quad (2.35)$$

where $\mathbf{H}_{avg} + \mathbf{G} \boldsymbol{\Delta}$ is the CFR matrix and \mathbf{z} is the AWGN in the frequency domain. The term $\mathbf{G} \boldsymbol{\Delta} \mathbf{s}$ represents ICI which is determined by $\boldsymbol{\Delta}$ and a fixed matrix \mathbf{G} where $\boldsymbol{\Delta}$ is DFT of the slope of the CIR, \mathbf{D}_t . Note that since \mathbf{M}_t and \mathbf{D}_t are circulant matrix, \mathbf{H}_{avg} and $\boldsymbol{\Delta}$ will be diagonal. On the contrary, \mathbf{G} is circulant since $\boldsymbol{\psi}$ is diagonal.

Consequently, the CFR matrix can be decomposed as

$$\begin{aligned} \mathbf{H}_f &= \mathbf{H}_{avg} + \mathbf{G}\mathbf{\Delta} \\ &= \begin{pmatrix} H_0 & 0 & \cdots & 0 \\ 0 & H_1 & & \vdots \\ \vdots & & \ddots & 0 \\ 0 & \cdots & 0 & H_{N-1} \end{pmatrix} + \begin{pmatrix} 0 & G_{-1} & \cdots & G_{-(N-1)} \\ G_1 & 0 & & \vdots \\ \vdots & & \ddots & G_{-1} \\ G_{N-1} & \cdots & G_1 & 0 \end{pmatrix} \begin{pmatrix} \Delta_0 & 0 & \cdots & 0 \\ 0 & \Delta_1 & & \vdots \\ \vdots & & \ddots & 0 \\ 0 & \cdots & 0 & \Delta_{N-1} \end{pmatrix}. \end{aligned} \quad (2.36)$$

Now, a tiny yet crucial rearrangement of this well-known ICI signal model is in order. By multiplying both sides of (2.35) by the diagonal matrix $(\mathbf{\Delta H}_{avg}^{-1})$, we can rearrange (2.35) into:

$$\underbrace{(\mathbf{\Delta H}_{avg}^{-1})\mathbf{r}}_{\tilde{\mathbf{r}}} = \underbrace{[\mathbf{I}_N + (\mathbf{\Delta H}_{avg}^{-1})\mathbf{G}]}_{\tilde{\mathbf{H}}} \underbrace{(\mathbf{\Delta s})}_{\tilde{\mathbf{s}}} + \underbrace{(\mathbf{\Delta H}_{avg}^{-1})\mathbf{z}}_{\tilde{\mathbf{z}}} \quad (2.37)$$

where \mathbf{I}_N denotes the $N \times N$ identity matrix, and $\tilde{\mathbf{s}}$ acts as the transmitted signal, $\tilde{\mathbf{r}}$ the received signal and $(\mathbf{\Delta H}_{avg}^{-1})\mathbf{G}$ as the ICI channel. Note that in (2.35), $\mathbf{\Delta}$ multiplies \mathbf{G} from the right; it follows that the column vectors of the CFR matrix are weighted by different Δ_k . This model registers how the signal on each subcarrier is spread over and comes to interfere other subcarriers. Different weights represent different spreading effects for each subcarrier. In (2.37), however, \mathbf{G} is multiplied by the diagonal matrix $(\mathbf{\Delta H}_{avg}^{-1})$ from the left; this time, row vectors of the CFR matrix are weighted with a different (Δ_k/H_k) . This model registers how a subcarrier is interfered by its neighboring subcarriers. Different weights indicates different ICI levels experienced by each subcarrier. These insights motivate us the following analysis.

2.4 ICI Indicator

The ICI model in (2.35) and (2.37) provides more insights when it is examined at the subcarrier-level granularity. There is no uniform band structure in the CFR matrix since each subcarrier faces very different ICI situations. In (2.37), $(\Delta \mathbf{H}_{avg}^{-1}) \mathbf{G}$ represents the ICI channel; this motivates us to propose the metric $|\Delta_k/H_k|$ to indicate the ICI level on each subcarrier. From (2.37), define the Signal-to-Interference Channel power Ratio (SICR) on the k -th subcarrier as

$$\text{SICR}_k = \frac{|\tilde{H}_{k,k}|^2}{\sum_{m=0, m \neq k}^{N-1} |\tilde{H}_{k,m}|^2}, \quad (2.38)$$

which can be further approximated to

$$\begin{aligned} \text{SICR}_k &\approx \left[\frac{N^2}{4\pi^2 N_s^2} \left| \frac{\Delta_k}{H_k} \right|^2 \left(2 \sum_{i=1}^{N/2-1} \frac{1}{|i|^2} \right) \right]^{-1} \\ &\approx \frac{12N_s^2}{N^2 |\Delta_k/H_k|^2} \end{aligned} \quad (2.39)$$

where $|G_i| \approx \frac{N}{2\pi N_s} \frac{1}{|i|}$ and $\sum_{i=1}^{\infty} \frac{1}{|i|^2} = \frac{\pi^2}{6}$ are used. Note that the SICR is inversely proportional to $|\Delta_k/H_k|^2$. For example, if a subcarrier suffers little ICI, the SICR (≥ 22 dB) will be quite high and $|\Delta_k/H_k|$ (≤ -5 dB) is low. On the other hand, when deep fading occurs at some subcarrier, $|\Delta_k/H_k|$ becomes large (≥ 0 dB) and SICR (≤ 12 dB) is low, and the demodulated symbol tends to be wrong due to severe ICI.

To better utilize $|\Delta_k/H_k|$ as the ICI indicator, its statistical properties are investigated. Assuming Rayleigh fading channels, $\delta(nN_s; l)$ and $h(nN_s - \frac{N-1}{2}; l)$, the CIR slope and the averaged CIR, are zero-mean circular complex Gaussian random variables (RVs) with variances $\sigma_{\delta(nN_s; l)}^2$ and $\sigma_{h(nN_s - \frac{N-1}{2}; l)}^2$. It follows that Δ_k and H_k are also zero-mean circular complex Gaussian RVs with variances $\sum_l \sigma_{\delta(nN_s; l)}^2$ and $\sum_l \sigma_{h(nN_s - \frac{N-1}{2}; l)}^2$ respectively. Note that denoting A as a zero-mean circular complex Gaussian RV with

variance σ^2 , the PDF of A is given by

$$p_A(a) = \frac{1}{\pi\sigma^2} \exp\left\{-\frac{|a|^2}{\sigma^2}\right\}. \quad (2.40)$$

It is well known that the magnitude of A , $B = |A|$, follows a Rayleigh distribution with parameter $\sigma^2/2$ as

$$p_B(b) = \frac{b}{\sigma^2/2} \exp\left\{-\frac{b^2}{\sigma^2}\right\}, \text{ if } b \geq 0, \quad (2.41)$$

and $p_B(b) = 0$ elsewhere.

To simplify the derivation, we further assume Δ_k and H_k are uncorrelated, on the grounds that Δ_k is caused by the mobility of scatterers while H_k is mainly determined by the reflection property of scatterers. This property is also shown in [13] in which the zeroth-order and the first-order derivative in the power series expansion of the channel correspond to our H_k and Δ_k . Define $X \triangleq 10\log_{10}(|\Delta_k|)$ and $Y \triangleq 10\log_{10}(|H_k|)$. Since $|\Delta_k|$ and $|H_k|$ are Rayleigh RVs with parameters $\frac{1}{2} \sum_l \sigma_{\delta(nN_S;l)}^2$ and $\frac{1}{2} \sum_l \sigma_{h(nN_S-\frac{N-1}{2};l)}^2$, X and Y follow the Log-Rayleigh distribution with the PDF [42], which can be derived from (2.41) by using the technique of function of RV, is given by

$$p(\varphi|\eta^2) = \frac{(e^{\varphi/c})^2}{c\eta^2} \exp\left(-\frac{(e^{\varphi/c})^2}{2\eta^2}\right) \quad (2.42)$$

where the constant $c = 10\log_{10}(e)$ and η^2 is the so-called localization parameter that equals to $\frac{1}{2} \sum_l \sigma_{\delta(nN_S;l)}^2$ for X and $\frac{1}{2} \sum_l \sigma_{h(nN_S-\frac{N-1}{2};l)}^2$ for Y . Since $10\log_{10}\left(\frac{|\Delta_k|}{|H_k|}\right) = 10\log_{10}(|\Delta_k|) - 10\log_{10}(|H_k|)$, the PDF of $10\log_{10}\left(\frac{|\Delta_k|}{|H_k|}\right)$ can be obtained as

$$p(\omega) = \int_{-\infty}^{\infty} p_X(\omega + y|\eta_X^2)p_Y(-y|\eta_Y^2)dy, \quad (2.43)$$

η_X^2 and η_Y^2 being the localization parameters of X and Y . Using the property that the mean of Log-Rayleigh PDF is $10\log_{10}(\eta^2) + c'$ where $c' = \frac{c}{2}(\ln 2 + \int_0^{+\infty} \ln v \exp(-v)dv)$ is a constant and the variance is $\frac{c^2\pi^2}{24}$ [42], it follows that the PDF of $10\log_{10}\left(\frac{|\Delta_k|}{|H_k|}\right)$ only

depends on the ratio between $\sum_l \sigma_{\delta(nN_S;l)}^2$ and $\sum_l \sigma_{h(nN_S-\frac{N-1}{2};l)}^2$. Intuitively, channel variation is caused by mobility rather than depends on the channel PDP. We expect the ratio to be insensitive to PDPs. In this case, the PDF of the ICI indicator will be consistent over a wide range of channels with different PDPs.

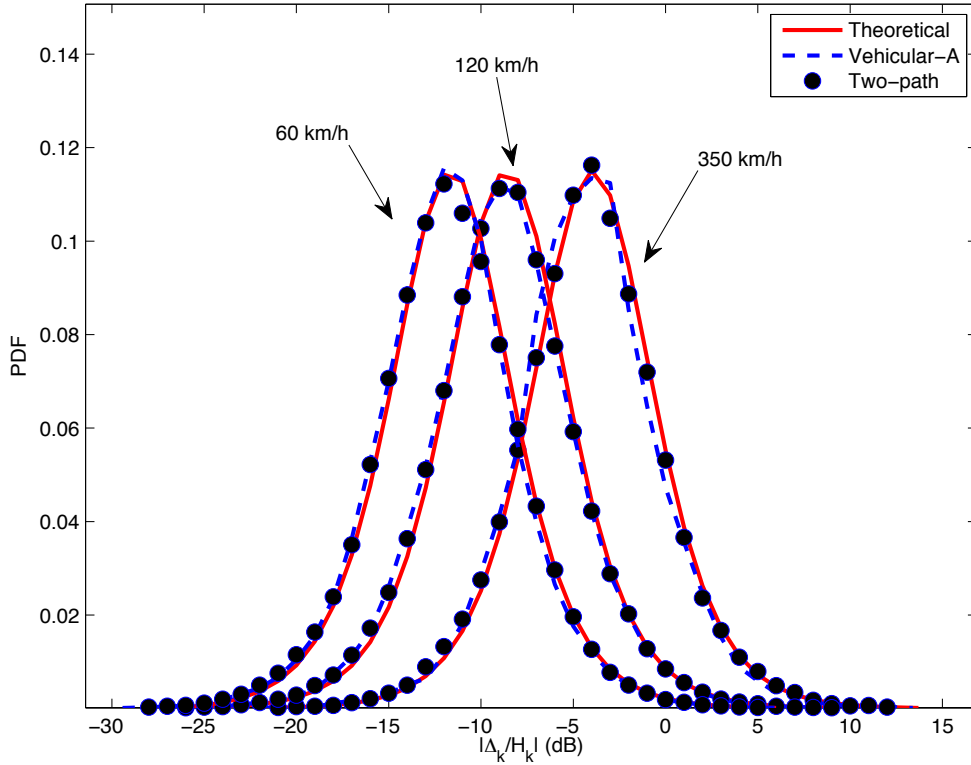


Figure 2.6: Probability density functions (solid lines) and two histograms (dash lines for the ITU Vehicular-A channel and dots for two-path equal gain channel) of $10\log_{10}(|\frac{\Delta_k}{H_k}|)$ for moving speeds at 60, 120 and 350 km/h. Bell-shape Doppler power spectrum and uncorrelated scattering are used.

Simulation is conducted to verify the theoretical result, using the WiMAX standard with 10 MHz bandwidth, 2.5 GHz central frequency, 1024 subcarriers. Two channel models with very different PDPs, the ITU Vehicular-A and a two-path equal gain channel, are used. Fig. 2.6 shows the theoretical PDF and the histogram of $10\log_{10}(|\frac{\Delta_k}{H_k}|)$ for various moving speeds, and they coincide closely so that our theo-

retical analysis of PDF is valid. Recall that larger $|\Delta_k/H_k|$ means higher ICI level. As the moving speed gets higher, more subcarriers experience severe ICI; yet even at 350 km/h, there still is a major portion of subcarriers experiencing mild ICI. It is also observed from Fig. 2.6 that the distribution of $|\Delta_k/H_k|$ remains essentially the same when two quite different PDPs are used. The PDF can be used in evaluating the benefit of reducing complexity by adapting ICI equalizers according to the ICI indicator. Details can be seen in Chapter 3.

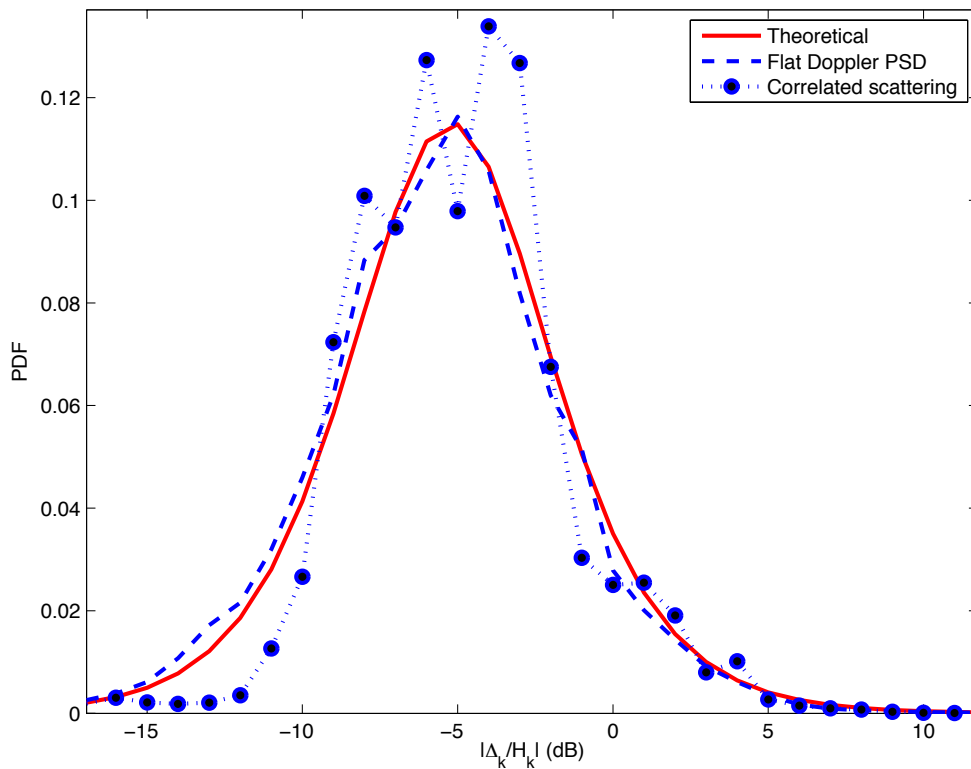


Figure 2.7: Probability density functions (solid lines) and two histograms (dash lines for the flat Doppler spectrum and dots for the correlated scattering with correlation 0.7 between paths) of $10\log_{10}(|\frac{\Delta_k}{H_k}|)$ for moving speed at 350 km/h. Two-path equal gain channel is used.

Other factors that may affect the PDF are also investigated. In Fig. 2.7, the effects of Doppler spectrum shape and correlated scattering are shown. As can be

seen, the PDF is also quite insensitive to the Doppler spectrum shape. In contrast, the correlation existing among channel paths can change the PDF. However, the overall trend is still that the PDF's center becomes larger when the moving speed gets larger, so does the maximum Doppler spread. Therefore, the ICI indicator can still offer useful information on channel variations.

In practice, the ICI indicator is obtained as the ratio between the estimates of Δ_k and H_k . An estimation method that uses consecutive OFDM symbols is provided in [15]. Here, with the goal of keeping complexity low, a simpler method is used. Instead of estimating the complete ICI model as in [15], we use the estimate of the averaged CFR, \hat{H}_k , which is always needed for signal demodulation. The estimate of Δ_k is simply obtained as the difference between \hat{H}_k of adjacent OFDM symbols due to the fact that CFR varies linearly across time-domain:

$$\hat{\Delta}_{k,n} = \hat{H}_{k,n} - \hat{H}_{k,n-1}$$

where second index in the subscript denotes the symbol index. Though the estimate is not very accurate, the degradation in simulated BER performance is insignificant. Channel estimation for time-varying channels may also be used [8,10–13], but we regard this as unnecessary in the current setting. To support higher Doppler spreads in the future, better channel estimation will be needed and advanced channel estimation techniques can be found in [43–47] and extended for MIMO channels in [48,49]. Furthermore, to jointly estimate the channel and other synchronization parameters has been proposed in [50–52].

2.5 Applications of ICI Indicator

In a vehicular network, a variety of communication types exist: vehicle-to-vehicle, vehicle-to-station, and vehicle-as-relay, etc. Together with the vastly different velocities at which each vehicle in the network moves, a very complicated landscape of relative velocities may exist. Due to the fact that the fading rate experienced at a receiver highly depends on the relative speed between the receiver and the transmitter, it becomes clear that a very diverse and dynamic fading environment is a reality that vehicular networks need to face on a regular basis. It is also well known that the information of fading rate can be utilized to adapt many communication subsystems to improve the overall performance. Therefore, the ability to make a timely estimation of the fading rate on each link can be a great asset to the nodes operating in a vehicular network.

The estimation of fading rate can not be always accomplished by deriving from the speed information obtained by global positioning system (GPS). For example, in a vehicle-to-vehicle link, the relative speed cannot be derived from GPS information before the link is established; however, the fading rate information may be valuable in establishing such a link. For another example, the fading rate may be effected greatly by fast-moving vehicles (reflectors) surrounding the transmitter/receiver, but the GPS information is not of much help in this case. Therefore, many techniques have been developed for estimating the fading rate in narrowband systems [53–55] or in wideband systems [56–58]. In narrowband systems, a common way is to use the level crossing rate of a certain signal, e.g., the received signal envelope [55], to estimate the Doppler frequency. Most methods rely on statistics collected in the time domain. For wideband systems, especially those that are based on OFDM, signals in the frequency domain are equally available; hence more options in choosing techniques to estimate the fading rate

may exist. Most approaches exploit the autocorrelation function (ACF) of the channel. However, the estimation of ACF usually demands higher computational complexity.

Since OFDM signals are distributed on a regular grid on the time-frequency plane, the channel variation can not only be described in the time domain, but also on each subcarrier on the frequency domain. The finer granularity with which the time-varying channel is described on the time-frequency plane may provide benefits when the information of channel variations is utilized.

A few things can be said about the benefits that a communication system can gain by utilizing the information of Δ_k . Several methods exist in the literature for estimating the maximum speed (or fading rate) of narrowband systems. Often, these methods rely on time-consuming practices of accumulating statistics in the time-domain. For wideband OFDM-based systems, the advantages accompanying wideband signals that cover large areas on the time-frequency plane should be exploited. Indeed, we found that the distribution of (Δ_k/H_k) is related to the maximum Doppler frequency (or speed) experienced by the receiver. Simulation results will be presented and confirm that the average of (Δ_k/H_k) in one OFDM symbol is enough to estimate the vehicle speed with impressive accuracy; furthermore, the relation between (Δ_k/H_k) and vehicle speed is quite insensitive to the assumed channel PDPs.

In modern communications, adaptive transmission systems are considered for maximizing the throughput and reducing the bit error rate. For example, the signal strength is widely used for the handoff decision [59]. Compared to conventional methods that only estimate a speed parameter for one symbol, (Δ_k/H_k) can be more useful by indicating the channel quality at a finer granularity, say, per subcarrier. Consequently, the system can adaptively adjust the coding, modulation, and power allocation for each

subcarrier according to (Δ_k/H_k) . At the receiver side, based on the channel quality at each subcarrier, different levels of interference cancellation and diversity combining schemes can be selected. Moreover, for OFDM systems experiencing fast fading, (Δ_k/H_k) is a more realistic metric since the impact due to ICI is also considered. This property is noticed in [24] where we proposed (Δ_k/H_k) to be used as an ICI indicator and to facilitate a low-complexity ICI equalization scheme.

2.5.1 Estimation of Channel Variations

Here we describe two channel variation estimation methods proposed in [15]. Both methods estimate the channel variation in time domain. However, in OFDM systems, pilot assisted channel estimation in frequency domain is more popular. Substituting (2.32) into (2.31), we obtain

$$\begin{aligned} H(m; pN_S - N + k) &= \sum_l \left(h\left(pN_S - \frac{N-1}{2}; l\right) + \frac{k - \frac{N-1}{2}}{N_S} \delta(pN_S; l) \right) e^{-\frac{j2\pi lm}{N}} \\ &= H_m + \frac{k - \frac{N-1}{2}}{N_S} \Delta_m \end{aligned} \quad (2.44)$$

where H_m denotes the DFT of the CIR at the center time of the p -th OFDM symbol:

$$H_m = \sum_l h\left(pN_S - \frac{N-1}{2}; l\right) e^{-\frac{j2\pi lm}{N}}, \quad (2.45)$$

and Δ_m is DFT of the CIR difference term,

$$\Delta_m = \sum_l \delta(pN_S; l) e^{-\frac{j2\pi lm}{N}}. \quad (2.46)$$

Based on the observations from (2.44), it can be observed that the CFR on the m -th subcarrier also varies linearly and a proposed estimation method in frequency domain has lower computational complexity.

Using Cyclic Prefixes

The redundancy information contained in the CP can be exploited for estimating the channel time variation. After subtracting the ISI caused from the previous OFDM symbol, the received signal in the CP duration of the current OFDM symbol can be expressed as an output of a linear system with variables $\{\delta(nN_S; l)\}$. By solving the linear equation, the channel variation estimate can be obtained. The details are referred to [15].

Using Three Consecutive Symbols in Time Domain

Assume an estimate of the averaged channel of the current symbol (n), $\{\hat{h}(nN_S - \frac{N-1}{2}; l)\}$, has been estimated. The channel variation estimate in time domain can be obtained by

$$\frac{[\hat{h}(nN_S - \frac{N-1}{2}; l) - \hat{h}((n-1)N_S - \frac{N-1}{2}; l)]}{2N_s} + \frac{[\hat{h}((n+1)N_S - \frac{N-1}{2}; l) - \hat{h}(nN_S - \frac{N-1}{2}; l)]}{2N_s}. \quad (2.47)$$

This method is based fitting a piece-wise linear model to the time-varying CIR, and it uses channel estimates of three OFDM symbols to estimate the variation rate at the middle OFDM symbol.

Using Two Adjacent Symbols

To keep the computational complexity low, a frequency-domain method can be used. Instead of trying to estimate the complete ICI model as in [15], we use the estimate of the averaged CFR, i.e. \hat{H}_k , which is always needed for signal demodulation. The estimate of Δ_k is simply obtained by subtracting \hat{H}_k of the adjacent OFDMA symbol,

Table 2.2: Simulation Parameters

Parameters	Values
Bandwidth	10 MHz
Sampling frequency	11.2 MHz
Subcarrier spacing	10.9375 KHz
OFDM symbol duration	102.9 μ s
CP ratio	1/8
Path delay of Veh-A channel	[0, 0.31, 0.71, 1.09, 1.73, 2.51] μ s
Path power of Veh-A channel	[0, -1, -9, -10, -15, -20] dB
Path delay of Ped-B channel	[0, 0.2, 0.8, 1.2, 2.3, 3.7] μ s
Path power of Ped-B channel	[0, -0.9, -4.9, -8, -7.8 -23.9] dB
Path delay of LDS channel	[0, 0.31, 0.71, 1.09, 1.73, 10] μ s
Path power of LDS channel	[0, -1, -9, -10, -15, -20] dB

reflecting the fact that CFR varies linearly across time-domain:

$$\hat{\Delta}_{k,n} = \hat{H}_{k,n} - \hat{H}_{k,n-1} \quad (2.48)$$

where second index in the subscript denotes the symbol index. Though the estimate is not very accurate, the degradation in simulated MSE performance is insignificant.

Computer simulations were conducted to compare the performance of channel variation estimators previously discussed. The simulation settings according to the WiMAX standard and the channel PDPs are summarized in Table 2.2.

The estimator performance in terms of normalized MSE (NMSE) is presented in Fig. 2.8. The NMSE is defined as $E[|\hat{\Delta} - \Delta|^2]/E[|\Delta|^2]$, where $E[\cdot]$ denotes the expectation operation. It can be seen that our proposed method, with lower complexity, has comparable performance to the method of using three OFDM symbols [15]. The method of using CP is the worst since its performance relies on the accuracy of ISI

estimation and cancellation.

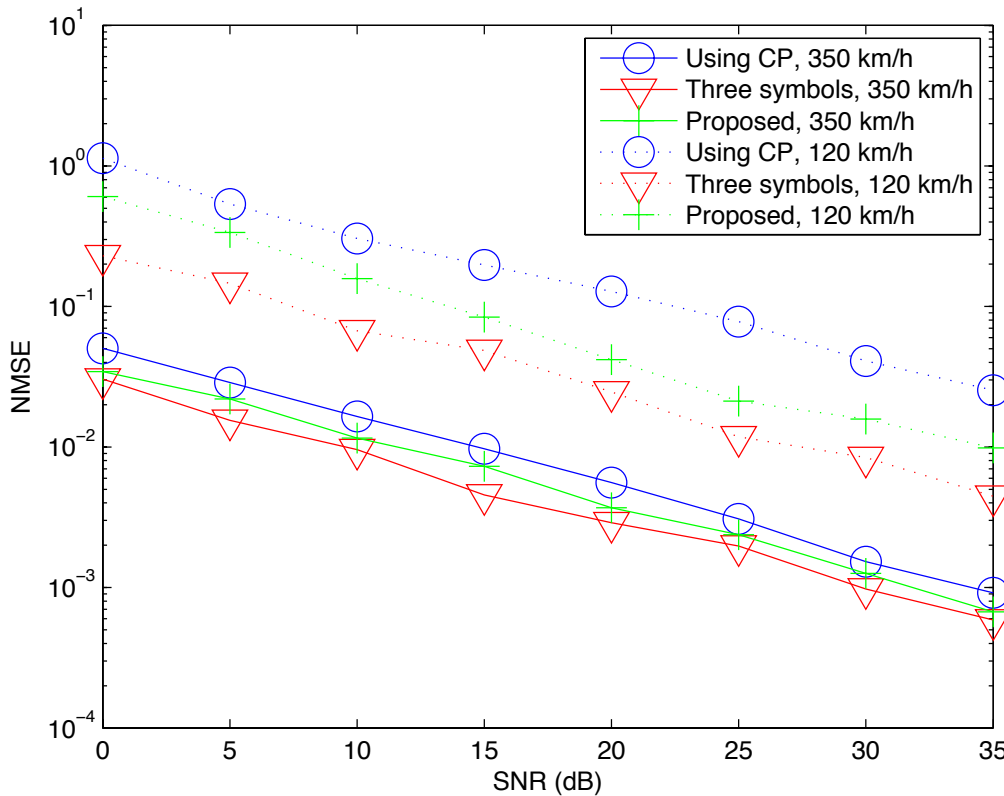


Figure 2.8: Normalized MSE versus SNR curves.

Fig. 2.9 depicts the mean of (Δ_k/H_k) with one OFDM symbol versus vehicle speeds. As can be seen, they follow a positively related curve which can be determined off-line. The estimation variance is rather small due to the large number of subcarriers in one OFDM symbol. More interestingly, the curve is insensitive to the assumed channel PDPs and thus remains a robust estimator of vehicle speed when the channel scenario changes.

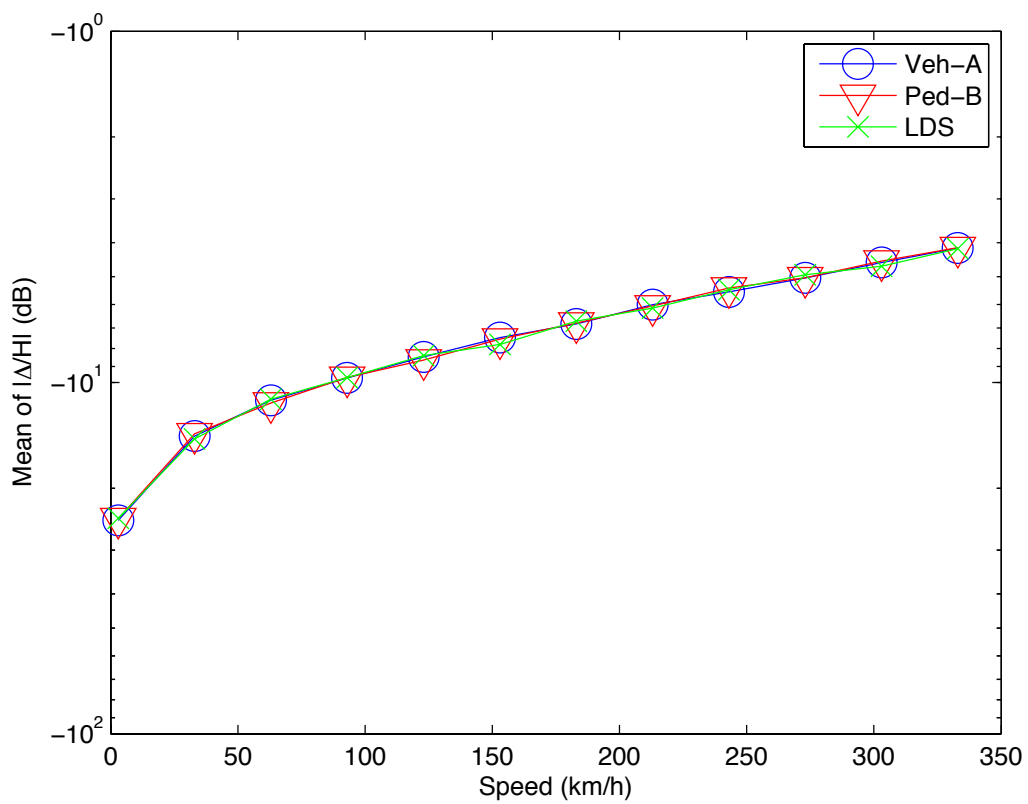


Figure 2.9: Mean of $|\Delta/H|$ versus speed curves.

Chapter 3 ICI Cancellation

For advanced mobile communication systems that adopt OFDMA technologies, ICI cancellation techniques are crucial for the performance when mobility is high and a number of methods have been studied. In [10,12,13,16], frequency-domain ZF or MMSE ICI equalizers are proposed, while time-domain equalizers are investigated in [8,11]. A common means to reduce the cost is to approximate the non-diagonal CFR matrix with a banded matrix in which all but few elements on selected $2Q + 1$ diagonals are set to zero [9,10,12,16,23].

Other than computational cost, features specified in advanced systems that were derived from WiMAX (IEEE 802.16e) [7] and LTE can also impose serious difficulties on engineering development. For instance, in Fig. 3.1 an example of subcarrier assignment under the mandatory mode of partial usage of subchannels (PUSC) in 802.16e is shown [7]. The usable subcarriers are divided into subsets denoted as subchannels. In the downlink, different users or groups of users may share the same subchannels. A user can end up using subcarriers interlaced with the subcarriers of other users. As a result, decision feedback equalizers (DFEs) [9,11,12] may not be appropriate for this situation, since its good performance relies on removing ICI induced by the user itself as well as by other users, which in turns requires the knowledge of CFR and data on unoccupied or other users' subcarriers. Under this circumstance, however, conventional linear equalizers can still be effective in mitigating ICI by inverting estimated CFR matrices with the help of pilots. Other sophisticated ICI cancellation techniques also face a variety of challenges restricting their deployment. The turbo ICI equalizer [17–19] requires CFR information and feedback from the channel decoder, and it has longer processing latency. Expectation-Maximization (EM) based iterative receivers that can

alleviates the error propagation and attains performance close to BER lower bound are investigated in [60]. Techniques that utilize time-domain windowing [9,14] are effective for a large Doppler spread range but the receiver has to deal with colored noise induced by windowing [61]. The maximum a-posteriori (MAP) and maximum likelihood sequence estimation (MLSE) ICI equalizers [21,23] offer the best BER performance, yet their cost is extremely high. Using the basis expansion model [14,21,22] to develop ICI equalizers has been a hot research topic; however, its practical deployment is complicated by issues of channel estimation and model fitting. In short, there is a strong motivation to seek possible improvement on conventional ICI equalizers to strike a right balance between performance and implementation complexity.

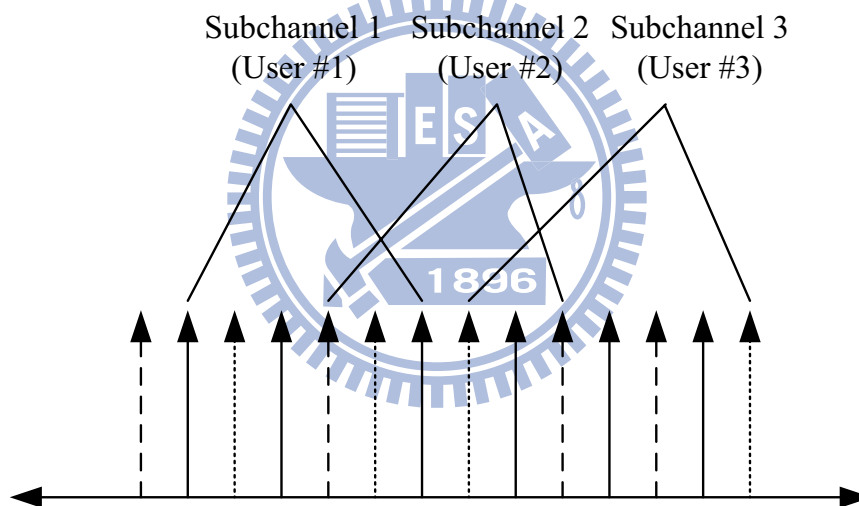


Figure 3.1: OFDMA frequency description of PUSC mode.

In this chapter, we focus on the inner receiver and develop low-complexity ICI equalizers for OFDMA downlink receivers. In Section 3.1, we review and classify existing techniques to deal with ICI in the literature. By using the system model and ICI indicator presented in Chapter 2, Section 3.2 introduces a per-subcarrier adaptive (PSA) ICI cancellation framework incorporating an ICI indicator. With the PSA framework, it is possible to use different ICI cancellation strategies on different subcarriers according to the ICI situation, say, simple ICI cancellation for subcarriers

experiencing mild ICI and heavy ICI cancellation for severe ICI. The PSA framework enables ICI equalizers achieve better trade-off between computational complexity and performance. In Section 3.3, novel low-complexity perturbation-based (PB) ZF and MMSE ICI equalizers are developed with the emphasis on implementation readiness and adequate performance. The proper mechanism of utilizing the ICI indicator is investigated to achieve robustness. Matrix inversion with lookup table (LUT) for sub-carriers experiencing severe ICI is also developed to complement the PB ICI equalizers. In Section 3.4, through comprehensive simulations, results of BER performance and savings in computational cost verify the effectiveness of our approach.

3.1 ICI Cancellation Techniques

A variety of techniques to combat ICI has been developed in recent years. We will introduce and classify them in the following.



3.1.1 Frequency Domain Approaches

As the linear equalization in the frequency domain is an area of particular interest, we recall the frequency domain system model (2.35). The received signal in the frequency domain can be written as

$$\mathbf{r} = \mathbf{H}_f \mathbf{s} + \mathbf{z} \quad (3.1)$$

where \mathbf{H}_f is the CFR matrix. The MMSE detector is to linear combine the received signal through a weighting matrix \mathbf{W} that minimizes the cost function $E[||\mathbf{s} - \mathbf{W}\mathbf{r}||^2]$.

The solution is given by

$$\mathbf{W} = \mathbf{H}_f^H (\mathbf{H}_f \mathbf{H}_f^H + \sigma^2 \mathbf{I}_N)^{-1} \quad (3.2)$$

where \mathbf{I}_N is the $N \times N$ identity matrix and σ^2 is the variance of \mathbf{z} .

When the SNR approaches to infinity, the MMSE solution is reduced to the ZF solution that tries to inverse the channel effect without considering the noise:

$$\mathbf{W} = \mathbf{H}_f^+ = (\mathbf{H}_f^H \mathbf{H}_f)^{-1} \mathbf{H}_f^H \quad (3.3)$$

where \mathbf{H}_f^+ is the pseudo inverse of \mathbf{H}_f and equals to $(\mathbf{H}_f)^{-1}$ if \mathbf{H}_f is invertible or not near ill-conditions. A well known fact is that the ZF equalizers yields worser performance than that of MMSE due to the noise enhancement problem.

Both ZF and MMSE equalizations require the $\mathcal{O}(N^3)$ complexity due to matrix inversion making them impractical for large N . Newton's iteration has been proposed to reduce the complexity in [20]. In the literature [9,10,16] it has been well recognized that the energy of Doppler-induced ICI will concentrated in the neighborhood and thus, the CFR matrix is approximated to be banded and the complexity can be reduced to $\mathcal{O}(N)$. However, according to the proposed ICI indicator we have a different perspective on this banded approximation as well as a more systematic way to do it. Mostly important benefit is that significant complexity reduction can be expected which will be more clear in the later.

Nonlinear approaches usually have better performance at the cost of increasing complexity. DFE which usually is realized as PIC or SIC in an iterative fashion is to reconstruct the interference term and cancel it from the received signal before the next iteration. The interference can be calculated as $\mathbf{H}_f' \hat{\mathbf{s}}$ where \mathbf{H}_f' is obtained by replacing the main diagonal of \mathbf{H}_f with zeros and $\hat{\mathbf{s}}$ is the ZF or MMSE data symbol estimate. Though the performance can be enhanced, the complexity is $\mathcal{O}(N^2)$ due to interference reconstruction and the error propagation problem could be an issue.

With the banded approximation, a trellis structure can be constructed from the

ICI channel and the optimal detector is MLSE in the sense of minimizing the sequence error probability and MAP in the sense of minimizing the bit error probability. Both cases need to calculate the conditional probability as the branch metric, for example, at the k -th subcarrier it is

$$P(R(k)|S(k)) = -\frac{1}{2\sigma_k^2} \left| R(k) - \sum_{l=-Q}^Q H_{k, \langle k-l \rangle_N} S(\langle k-l \rangle_N) \right|^2 \quad (3.4)$$

where $H_{i,j}$ is the (i, j) -th element of the matrix \mathbf{H}_f , $\langle \cdot \rangle$ denotes the modulo operation and σ_k^2 is the variance of $z(k)$. As the number of states in the trellis grows exponentially with the ICI channel length, the complexity of MLSE or MAP is $\mathcal{O}(M^{2Q+1})$ where M is the modulation order.

3.1.2 Time Domain Approaches

The effects of time variations could also be mitigated through the time-domain approaches. Let's recall the system model in the time domain (2.33) that the received signal in the time domain is

$$\mathbf{y} = \mathbf{H}_t \mathbf{x} + \mathbf{n}. \quad (3.5)$$

In [8], a temporal filter is designed to combat ICI by maximizing the SINR of each subcarrier. We briefly summarize the results and left details in [8]. By multiplying a matrix \mathbf{W} , the received signal can be expressed as

$$\tilde{\mathbf{y}} = \mathbf{W} \mathbf{y} = \mathbf{W} \mathbf{H}_t \mathbf{x} + \mathbf{W} \mathbf{n} \quad (3.6)$$

and the frequency domain signal is

$$\mathbf{r} = \mathbf{F} \tilde{\mathbf{y}} = \mathbf{F} \mathbf{W} \mathbf{H}_t \mathbf{F}^H \mathbf{s} + \mathbf{F} \mathbf{W} \mathbf{n} \stackrel{\text{def}}{=} \mathbf{G} \mathbf{s} + \tilde{\mathbf{n}}. \quad (3.7)$$

Using (3.7), the SINR at the k -th subcarrier can be derived as

$$\begin{aligned} \text{SINR}_k &= \frac{E[|\mathbf{G}_{k,k}|^2]}{\frac{1}{N}\text{tr}(\mathbf{R}_{\tilde{\mathbf{n}}\tilde{\mathbf{n}}}) + \sum_{l \neq k} E[|\mathbf{G}_{k,l}|^2]} \\ &= \frac{\mathbf{w}_k^H \mathbf{h}_k \mathbf{h}_k^H \mathbf{w}_k}{\mathbf{w}_k^H \left(\frac{1}{\text{SNR}} \mathbf{I} + \mathbf{R}_k \right) \mathbf{w}_k} \end{aligned} \quad (3.8)$$

where $\mathbf{f}_k = \mathbf{F}^H \mathbf{e}_k$, \mathbf{e}_k is a column vector with 1 at the k -th element and zeros elsewhere, $\mathbf{h}_k = \mathbf{H}_t \mathbf{f}_k$, $\mathbf{w}_k = \mathbf{W}^H \mathbf{f}_k$ and $\mathbf{R}_k = \mathbf{H}_t \mathbf{H}_t^H - \mathbf{h}_k \mathbf{h}_k^H$. From (3.8), the optimization problem can be formulated as

$$\begin{aligned} \max_{\mathbf{h}_k} \quad & \mathbf{w}_k^H \mathbf{h}_k \mathbf{h}_k^H \mathbf{w}_k \\ \text{subject to} \quad & \mathbf{w}_k^H \left(\frac{1}{\text{SNR}} \mathbf{I} + \mathbf{R}_k \right) \mathbf{w}_k = 1 \text{ and } \mathbf{h}_k^H \mathbf{h}_k = 1. \end{aligned} \quad (3.9)$$

The solution of (3.9) can be found by $\tilde{\mathbf{w}}_k = \mathbf{R}_{\mathbf{y}\mathbf{y}}^{-1} \tilde{\mathbf{h}}_k$ and then normalize $\tilde{\mathbf{w}}_k$ as $\tilde{\mathbf{w}}_k / |\tilde{\mathbf{w}}_k|$. Note that this approach requires the complexity of $\mathcal{O}(N^3)$ when designing the filter due to the matrix inverse of $\mathbf{R}_{\mathbf{y}\mathbf{y}}^{-1}$ and the complexity of $\mathcal{O}(N^2)$ when applying the filter.

Inspired by the ISI-shortening in the single carrier systems, Schiter [9] proposed a time domain windowing to limit the ICI spreads, say, only $2Q + 1$ ICI channel coefficients are nonzero after the windowing. Though the supported Doppler frequency can be greatly extended after adopting the time domain windowing approach, the estimation of the resulting channel becomes more challenging.

3.1.3 Other Approaches

There are many other approaches have been proposed and we list some of them in the following. As the ICI coefficients are similar between neighboring subcarriers, [62] proposed allocate the same data symbol on these subcarriers and the self-ICI-cancellation is proposed at the receiver with good performance but the data rate (spectral efficiency) is severely reduced.

It is possible to appropriately choose system parameters such as subcarrier spacing and OFDM symbol length to avoid ICI [63]. However, this requires changes both in the transmitter and receiver and the industrial standards nowadays usually do not provide so much flexibility.

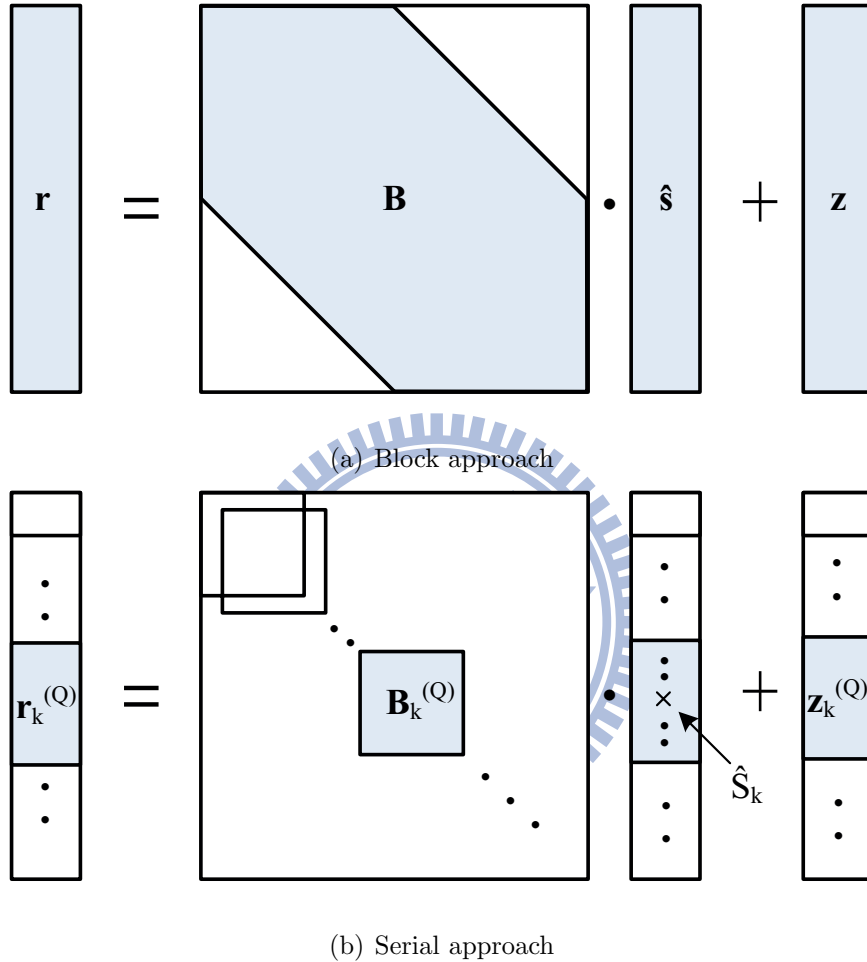


Figure 3.2: Block and serial approaches for ICI equalization.

3.2 The Per-Subcarrier Adaptive ICI Cancellation Framework

We focus on the linear equalizers in the frequency domain. As mentioned in Chapter 1, a common means to reduce the complexity of ICI equalization is to approximate

the non-diagonal CFR matrix with a banded matrix. For example, the approximation by banded CFR matrices can be utilized to construct the so-called *block* and *serial* ICI equalizers [16]. The CFR matrix \mathbf{H}_f in (3.1) is first approximated by a banded matrix \mathbf{B} in which all but few elements on the selected $2Q + 1$ diagonals are set to zero. The transmitted signal \mathbf{s} can be estimated by solving the resulted linear model, either by ZF or MMSE criteria. Figure 3.2 illustrates the difference between the block and serial approaches. In the block approach, the whole system of linear equations is solved altogether, e.g, the banded matrix \mathbf{B} is directly inverted in the ZF approach to find the estimation of \mathbf{s} . While in the serial approach, for each subcarrier a local $(2Q + 1) \times (2Q + 1)$ banded CFR matrix is considered, i.e., consider $\mathbf{B}_k^{(Q)} \triangleq [\mathbf{H}_f]_{\{<k-Q:k+Q>_N, <k-Q:k+Q>_N\}}$, and a truncated $(2Q + 1) \times (2Q + 1)$ system of linear equations is solved for each subcarrier. Apparently, the serial approach enjoys an even lower complexity than the block approach does, but it also results in a larger performance degradation since the truncation in building smaller systems of linear equations introduces larger approximation errors.

The approach of using banded CFR matrices is, however, highly inefficient, especially taking into account the fact that each subcarrier can experience vastly different ICI scenarios. Intuitively, if different counter-ICI measures are adopted for different subcarrier, possible benefits of reduced complexity and/or enhanced performance may follow. A closer look at the ICI model in (2.35) and (2.37) provides details about the different ICI scenarios faced by each subcarrier. Figure 3.3 shows the magnitude of a 32×32 example CFR matrix and three cross-sections on three subcarriers. It is clear that a uniform banded approximation is inappropriate, since each subcarrier faces very different ICI situations. Inspired by the observations made from (2.37), a metric $|\Delta_k/H_k|$ is introduced to indicate the ICI severity on the k -th subcarrier. In

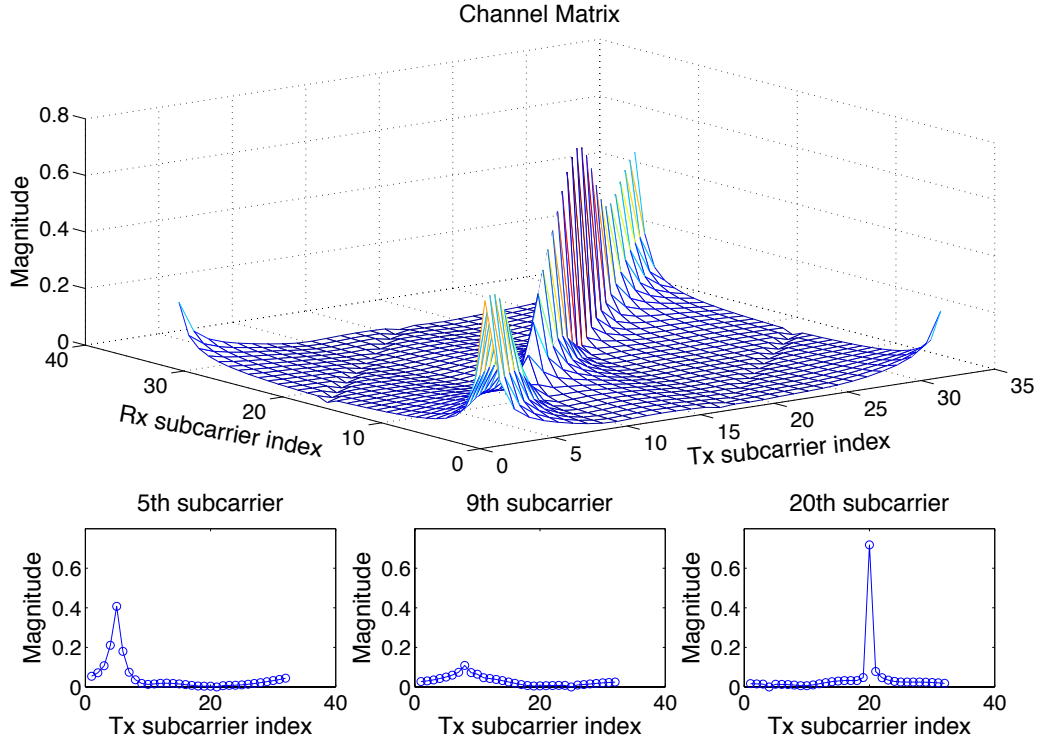


Figure 3.3: The magnitude of the CFR matrix and cross-sections at selected subcarriers.

Fig. 3.3, the 20-th subcarrier, with a small $|\Delta_k/H_k|$ ($|\Delta_k/H_k| < -5$ dB, SICR > 22 dB), is affected by insignificant amount of ICI. When moderate fading occurs, like on the 5-th subcarrier, $|\Delta_k/H_k|$ becomes higher, and moderate ICI emerges. When deep fading occurs, as on the 9-th subcarrier, $|\Delta_k/H_k|$ becomes significant ($|\Delta_k/H_k| > 0$ dB, SICR < 12 dB), severe ICI exists and heavy ICI cancellation may be needed to maintain BER performance. The term $|\Delta_k/H_k|$ is able to indicate the ICI situation and the different need of ICI cancellation strategies on each subcarrier.

Our experiences show that in practical situations, the majority of subcarriers face moderate or very mild ICI situations; that is, little or no ICI cancellation needs to be done on these subcarriers and the performance will not suffer. Fig. 3.4 gives an idea of how many percentages of subcarriers face very mild ($|\Delta_k/H_k| < -5$ dB) and

heavy ICI ($|\Delta_k/H_k| > 0$ dB). The simulation is conducted under WiMAX standard: 10 MHz bandwidth, 2.5 GHz central frequency, and 1024 subcarriers. Two very different channel PDPs are considered: the ITU Pedestrian-B (PedB) channel and a two-path equal-gain channel. Different vehicle speeds from 60 km/h to the maximum speed of 350 km/h suggested in the LTE and WiMAX standards are simulated. The results show that as vehicle speed gets higher, more subcarriers experience severe ICI; yet even at 350 km/h, there are still 85% of subcarriers on which $|\Delta_k/H_k| < 0$ dB and simple ICI cancellation strategies may be good enough for these subcarriers. An interesting observation is that the percentages of the ICI indicator remain almost the same when the channel PDP changes; therefore we expect the ICI indicator work properly for different types of channels.

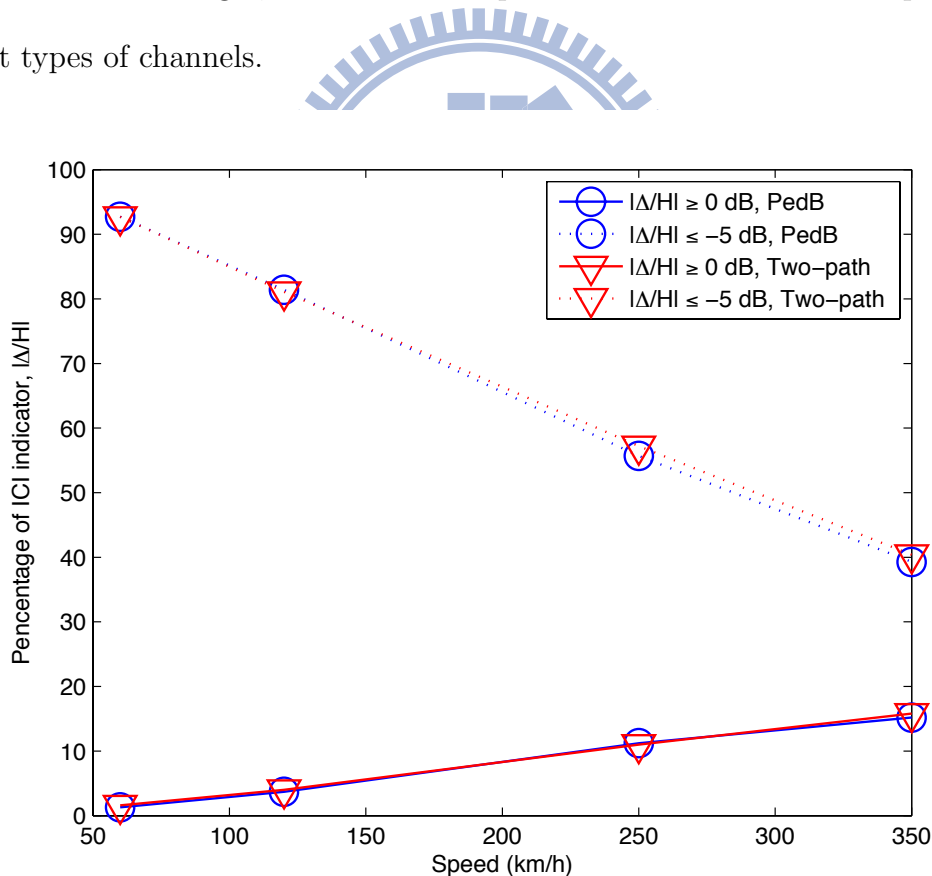


Figure 3.4: This figure shows the percentages of $|\Delta_k/H_k|$ that are larger than 0 dB or smaller than -5 dB at different vehicle speeds. Two channel PDPs, the ITU Pedestrian-B channel and the two-path equal-gain channel, are used.

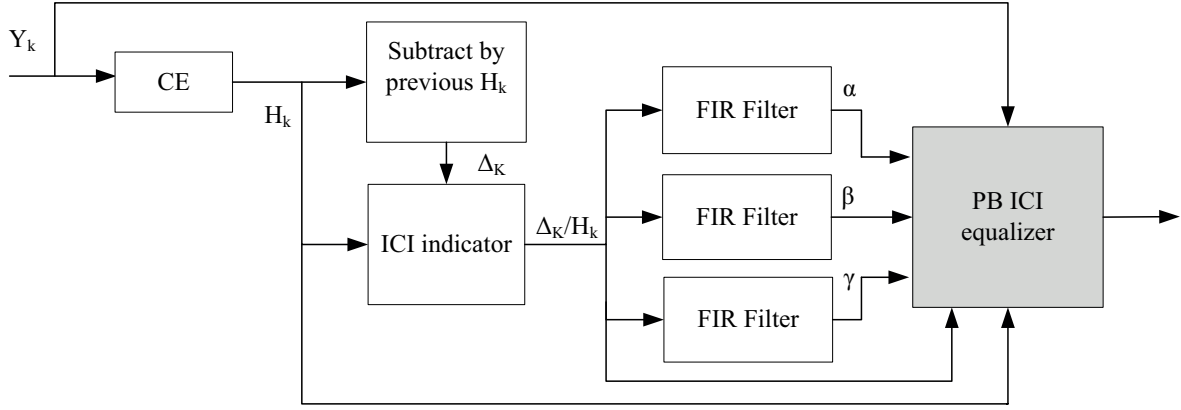


Figure 3.5: A receiver adopting the PSA framework.

Based on the ICI indicator, a PSA receiver architecture shown in Fig. 3.5 is also proposed in [24] where the FIR filters being the realization of proposed PB ICI equalizers which will be discussed in details in Section 3.3. A variety of existing ICI equalizers can be incorporated into this architecture and their settings can be adapted on each subcarrier according to $|\Delta_k/H_k|$; in this way, a better trade-off between computational complexity and performance can be achieved. PSA utilizes the idea of using different Q on each subcarrier to approximate the CFR matrix \mathbf{H}_f . Figure 3.6 depicts how the CFR matrix \mathbf{H}_f , instead of being approximated by a banded matrix with fixed bandwidth Q as shown in Fig. 3.2, is approximated by a banded matrix with variable bandwidth adaptively set at each subcarrier. The approach also works well with popular wireless access technologies such as WiMAX and LTE based on OFDMA. In the following section, the PSA architecture forms the foundation for us to develop novel low-complexity ICI methods with remarkable results.

3.2.1 Incorporate the MAP ICI Equalizer

The MAP equalizer offers the optimal performance yet is very costly. In our approach, reduction in computational complexity is achieved by reducing the size of trellis at

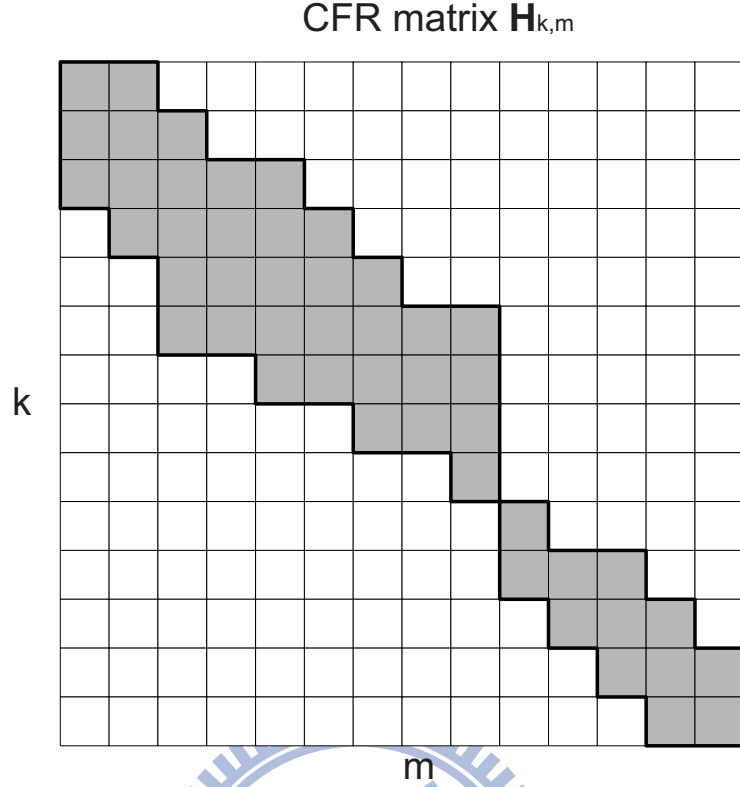


Figure 3.6: A banded CFR matrix with variable bandwidth Q .

most subcarriers. The MAP equalizer outputs the log-likelihood ratio (LLR) of the b -th bit of $S(m)$ via $L(S_{m,b}) \triangleq \log \frac{P(S_{m,b}=1|\mathbf{r})}{P(S_{m,b}=0|\mathbf{r})}$. LLRs can be efficiently calculated by the BCJR algorithm, which consists of forward recursion, backward recursion and calculating transition probabilities. The rearrangement of ICI model in (2.37) gets into calculating the branch metric of the k -th subcarrier through

$$P(\tilde{R}(k)|\tilde{S}(k)) = -\frac{1}{2\sigma_k^2} \left| \tilde{R}(k) - \sum_{l=-Q}^Q \tilde{H}_{k,\langle k-l \rangle_N} \tilde{S}(\langle k-l \rangle_N) \right|^2 \quad (3.10)$$

where σ_k^2 is the variance of $\tilde{z}(k)$.

Consider an OFDMA system (WiMAX) with 10 MHz bandwidth, 2.5 GHz central frequency, 1024 subcarriers, QPSK modulation, and the ITU Vehicular-A channel model at 500 km/h. Fig. 3.7 shows the BER curves of MAP ICI equalizers, with fixed Q and variable Q . The result verifies that adjusting the trellis size does not hurt the performance even when the speed hits 500 km/h. The MAP ICI equalizer with a

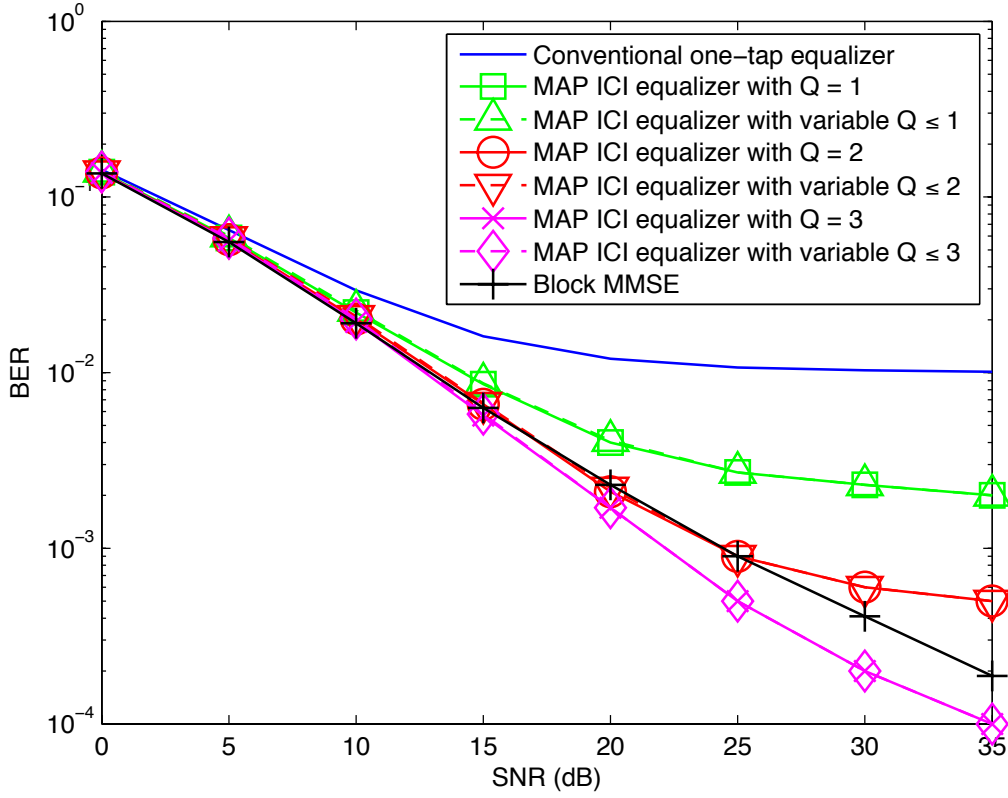


Figure 3.7: BER performance comparisons for MAP ICI equalizers under 1024-point FFT, QPSK and ITU Vehicular-A channel model at 500 km/h. The BER curves of the MAP ICI equalizer (solid lines) and the variable Q MAP ICI equalizer (dash lines) essentially overlap.

variable-size trellis attains the same BER performance as that of the MAP ICI equalizer with a fixed large trellis (in fact, their BER curves overlap each other), yet the computational cost is significantly reduced. The complexity comparison is summarized in Table 3.3, where the number of complex floating-point operations (FLOPs) is counted. Compared to the block MMSE and fixed Q MAP, variable $Q(\leq 3)$ MAP significantly reduces computational complexity by two orders of magnitude without sacrificing BER performance. Moreover, the memory required to store $M^{(2Q+1)}$ states at each trellis stage also enjoys great reduction by adopting variable Q . In the simulation, 85% of stages use merely 4 states instead of the full $4^7 = 16384$ states. Further reduction of

complexity is possible if techniques such as those in [18,23] can be incorporated in the future. Finally, it is interesting to note that the variable Q MAP ICI equalizer performs better than the block MMSE ICI equalizer. It is due to the extra gain provided by combining signals along different ICI paths constructively.

Table 3.1: Computational complexity comparison.

Methods	Complexity	Number of complex flops
Block MMSE	$\mathcal{O}(N^3)$	4×10^8
Conventional fixed Q MAP	$\mathcal{O}(M^{2Q+1}(4Q+2)N)$	$2 \times 10^8 (Q=3),$ $8.6 \times 10^6 (Q=2),$ $322560 (Q=1)$
Variable Q MAP	$\sum_i \mathcal{O}(M^{2Q_i+1}(4Q_i+2)N)$	$2.88 \times 10^6 (Q \leq 3),$ $1.24 \times 10^6 (Q \leq 2),$ $255728 (Q \leq 1)$

3.3 Proposed Novel Low-Complexity ICI Equalizers

3.3.1 Perturbation-based ZF ICI Equalizer

The PSA architecture allows different strategies be adopted for each subcarrier according to the ICI indicator. For subcarriers inflicted by severe ICI, costly methods, say, matrix inversion, are needed; while for subcarriers inflicted by mild ICI, very simple equalizers suffice to provide good performance. In this subsection, simple perturbation-based (PB) equalizers that are perfect for treating mild ICI are developed. Figure 3.8

shows the block diagram of the proposed PB ICI equalizers.

Start with (2.37) and zoom in the neighboring $2Q + 1$ subcarriers of the k -th subcarrier. The superscript (Q) and subscript k will be dropped temporarily for simplicity. A serial ZF equalizer on the k -th subcarrier operates as follows

$$\begin{aligned}\hat{S}_k &= \mathbf{w}\mathbf{r} = \mathbf{e}_c \mathbf{\Delta}^{-1} \tilde{\mathbf{H}}^{-1} (\mathbf{\Delta} \mathbf{H}_{avg}^{-1}) \mathbf{r} \\ &= \mathbf{e}_c \mathbf{\Delta}^{-1} (\mathbf{I}_{2Q+1} + (\mathbf{\Delta} \mathbf{H}_{avg}^{-1}) \mathbf{G})^{-1} (\mathbf{\Delta} \mathbf{H}_{avg}^{-1}) \mathbf{r},\end{aligned}\quad (3.11)$$

where the $1 \times (2Q + 1)$ row vector \mathbf{w} denotes the equalizer and \mathbf{e}_c is a $1 \times (2Q + 1)$ row vector with 1 at the center and zeros elsewhere. The diagonal matrix $(\mathbf{\Delta} \mathbf{H}_{avg}^{-1})$ will be approximated by a model with few parameters. The goals are two-folded: a simple model makes it possible to replace \mathbf{w} with simple filters on subcarriers facing mild ICI; meanwhile the matrix inversion $(\mathbf{I}_{2Q+1} + (\mathbf{\Delta} \mathbf{H}_{avg}^{-1}) \mathbf{G})^{-1}$ is available to fight severe ICI, with the corresponding inverse matrices being calculated off-line and stored in a LUT indexed by the parameters α , β and γ in (3.12).

Polynomial curve fitting is used to approximate the local CFR fluctuation of $(\mathbf{\Delta} \mathbf{H}_{avg}^{-1})$:

$$(\mathbf{\Delta} \mathbf{H}_{avg}^{-1}) \approx \alpha \mathbf{I}_{2Q+1} + \beta \mathbf{L} + \gamma \mathbf{P} \quad (3.12)$$

where \mathbf{L} and \mathbf{P} are both diagonal with linear and parabolic shapes, i.e., $\mathbf{L} = \text{diag}(Q, Q-1, \dots, -Q)$ and $\mathbf{P} = \text{diag}(Q^2, (Q-1)^2, \dots, (-Q)^2)$. Note that the parameters α , β and γ can be obtained by least squares method which can be realized as applying fixed finite-impulse response (FIR) filters. Substituting (3.12) into (3.11) and applying $(\mathbf{I} + \mathbf{A})^{-1} \approx \mathbf{I} - \mathbf{A} + \mathbf{A}^2 + o(\epsilon)$ where \mathbf{A} is the perturbation term and $o(\epsilon)$ denotes the higher-order terms, the low-complexity ICI equalizer can be obtained. Ignoring high-order terms, the first-order PB-ZF equalizer is given by

$$\mathbf{w}_{ZF^{1st}} = \mathbf{e}_c \mathbf{H}_{avg}^{-1} - \frac{1}{\Delta_k} (\alpha \mathbf{e}_c \mathbf{G}) (\mathbf{\Delta} \mathbf{H}_{avg}^{-1}). \quad (3.13)$$

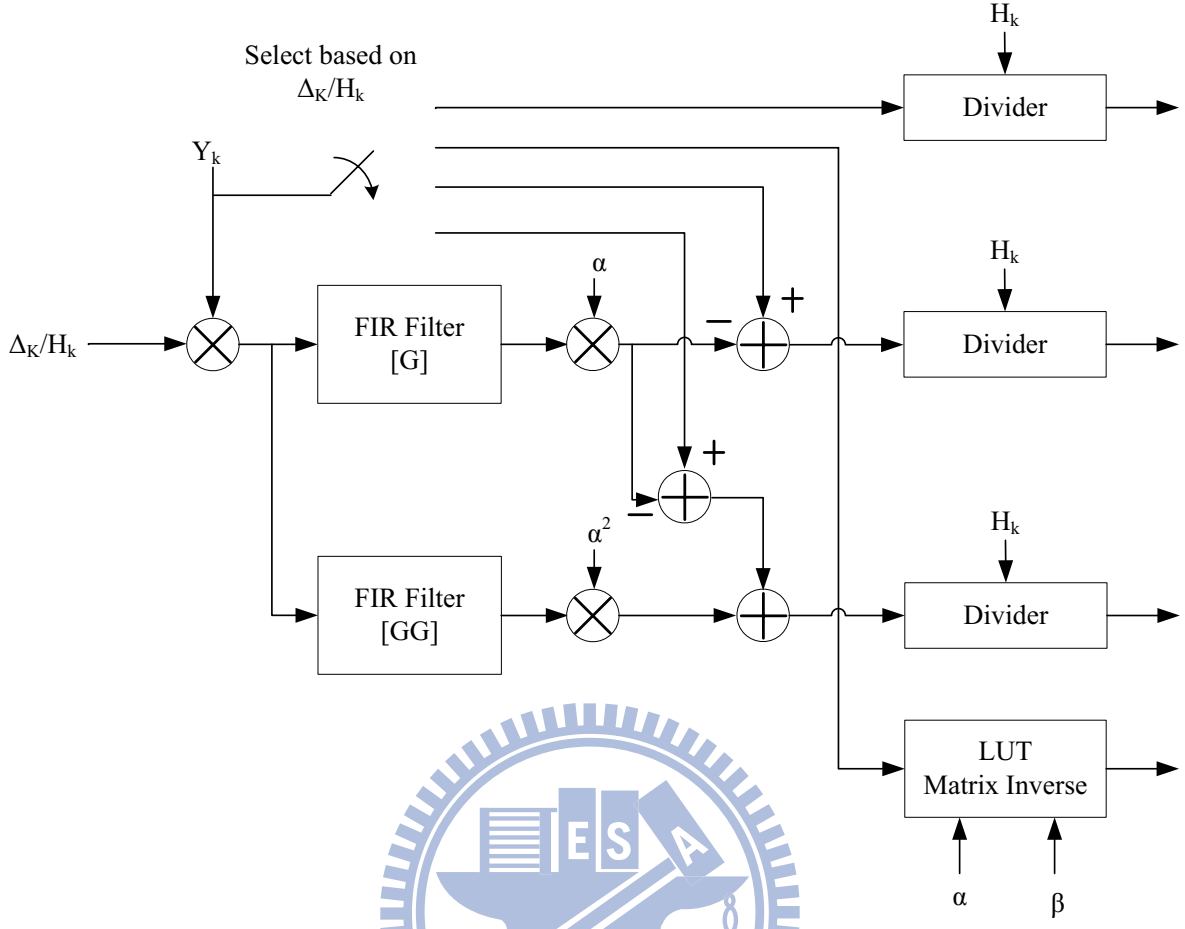


Figure 3.8: PB ICI equalizer block diagram.

Including second-order terms gives the second-order PB-ZF equalizer:

$$\mathbf{w}_{ZF^{2nd}} = \mathbf{e}_c \mathbf{H}_{avg}^{-1} - \frac{1}{\Delta_k} (\alpha \mathbf{e}_c \mathbf{G} - \alpha^2 \mathbf{e}_c \mathbf{G}^2) (\Delta \mathbf{H}_{avg}^{-1}). \quad (3.14)$$

Two approximations are involved here: the approximation of $(\Delta \mathbf{H}_{avg}^{-1})$ and the approximation of $(\mathbf{I}_{2Q+1} + (\Delta \mathbf{H}_{avg}^{-1}) \mathbf{G})^{-1}$. In most cases ZF equalizers with only lower-order terms are good enough. When ICI is severe, more costly methods (matrix inversion, for example) involved with β and γ may be used.

A crucial advantage of our approach becomes clear by observing that, without the approximation in (3.12), the conventional perturbation method that uses $(\mathbf{I} + \mathbf{A})^{-1} \approx \mathbf{I} - \mathbf{A} + \mathbf{A}^2 + o(\epsilon)$ will yield

$$\mathbf{w}_{ZF^{2nd}} = \mathbf{e}_c \mathbf{H}_{avg}^{-1} - \mathbf{e}_c \mathbf{H}_{avg}^{-1} (\mathbf{G} \Delta \mathbf{H}_{avg}^{-1}) + \mathbf{e}_c \mathbf{H}_{avg}^{-1} \mathbf{G} (\Delta \mathbf{H}_{avg}^{-1}) \mathbf{G} (\Delta \mathbf{H}_{avg}^{-1}). \quad (3.15)$$

In this case, the matrix multiplications within the third term of (3.15), $\mathbf{e}_c \mathbf{H}_{avg}^{-1} \mathbf{G} (\Delta \mathbf{H}_{avg}^{-1}) \cdot \mathbf{G} (\Delta \mathbf{H}_{avg}^{-1})$, cannot commute. That is, the signal will be multiplied by $(\Delta \mathbf{H}_{avg}^{-1})$, filtered by \mathbf{G} , then multiplied by $(\Delta \mathbf{H}_{avg}^{-1})$ before getting filtered by \mathbf{G} again. Our approximation results in a more efficient filtering procedure. With the polynomial approximation of $(\Delta \mathbf{H}_{avg}^{-1})$, the proposed perturbation equalization in (3.14) mainly consists of fixed FIR filters, i.e., the central row vectors of \mathbf{G} and $(\mathbf{G}\mathbf{G})$.

When the ICI is severe, matrix inversion may be needed to achieve decent ICI cancellation. By extracting the parameters $\{\alpha, \beta, \gamma\}$, a LUT of matrix inversion indexed by $\{\alpha, \beta, \gamma\}$ can be pre-calculated off-line and applied when needed. The LUT of matrix inversion will be described in more details in subsection 3.3.4.

3.3.2 Perturbation-based MMSE ICI Equalizer

When a channel goes into a fade, MMSE equalizers are more effective than ZF equalizers in preventing noise enhancement. In order to take advantage of the re-arrangement in (2.37) for developing low-complexity filters, the MMSE solution of $\tilde{\mathbf{s}}$ instead of \mathbf{s} is derived, and the inverse mapping $\Delta^{-1} \tilde{\mathbf{s}}$ is used to recover \mathbf{s} . Strictly speaking, this procedure differs from conventional MMSE approaches because the noise term $(\Delta \mathbf{H}_{avg}^{-1}) \mathbf{z}$ has different power levels on each subcarrier. But the effect on performance is negligible, due to reasons explained next. Consider serial equalizers, the corresponding channel matrix for each subcarrier is a truncated matrix, that is, a $(2Q+1) \times (2Q+1)$ one within which the noise is treated as white with a localized SNR. For practical channel scenarios, computer simulations show that this assumption of whiteness is quite accurate and has little impact on performance. Therefore, locally white noise with a localized SNR is assumed for the development of PB-MMSE ICI equalizers.

A typical MMSE IC equalizer is:

$$\begin{aligned}
\mathbf{w} &= \mathbf{e}_c \boldsymbol{\Delta}^{-1} \tilde{\mathbf{H}}^* [\tilde{\mathbf{H}} \tilde{\mathbf{H}}^* + \frac{1}{\rho_k} \mathbf{I}]^{-1} (\boldsymbol{\Delta} \mathbf{H}_{avg}^{-1}) \\
&= \mathbf{e}_c \boldsymbol{\Delta}^{-1} (\mathbf{I} + (\boldsymbol{\Delta} \mathbf{H}_{avg}^{-1}) \mathbf{G})^* \times \\
&\quad [(\mathbf{I} + (\boldsymbol{\Delta} \mathbf{H}_{avg}^{-1}) \mathbf{G})(\mathbf{I} + (\boldsymbol{\Delta} \mathbf{H}_{avg}^{-1}) \mathbf{G})^* + \frac{1}{\rho_k} \mathbf{I}]^{-1} (\boldsymbol{\Delta} \mathbf{H}_{avg}^{-1})
\end{aligned} \tag{3.16}$$

where * denotes the complex conjugate transposition and ρ_k the *localized* SNR which is estimated from $2Q + 1$ neighboring subcarriers.

By applying the polynomial approximation of $(\boldsymbol{\Delta} \mathbf{H}_{avg}^{-1})$ and the perturbation approximation of $(\mathbf{I} + \mathbf{A})^{-1}$ where \mathbf{A} is the perturbation term, the PB-MMSE ICI equalizer is obtained. When the localized SNR on a subcarrier is large, higher order terms can be ignored, and we have the first-order PB-MMSE ICI equalizer:

$$\begin{aligned}
\mathbf{w}_{MMSE^{1st}} &= \frac{\rho}{\rho + 1} \mathbf{e}_c \mathbf{H}_{avg}^{-1} - \frac{1}{\Delta_k} \cdot \frac{\rho}{\rho + 1} \times \\
&\quad \left[\frac{\rho}{\rho + 1} \alpha \mathbf{e}_c \mathbf{G} + \frac{1}{\rho + 1} \alpha^* \mathbf{e}_c \mathbf{G}^* + \right. \\
&\quad \left. \frac{1}{\rho + 1} \beta^* \mathbf{e}_c \mathbf{G}^* \mathbf{L}^* + \frac{1}{\rho + 1} \gamma^* \mathbf{e}_c \mathbf{G}^* \mathbf{P}^* \right] (\boldsymbol{\Delta} \mathbf{H}_{avg}^{-1}).
\end{aligned} \tag{3.17}$$

If \mathbf{H}_{avg} is close to a fade, higher-order terms with α^2 are added, and the second-order PB-MMSE ICI equalizer is:

$$\begin{aligned}
\mathbf{w}_{MMSE^{2nd}} &= \frac{\rho}{\rho + 1} \mathbf{e}_c \mathbf{H}_{avg}^{-1} - \frac{1}{\Delta_k} \cdot \frac{\rho}{\rho + 1} \times \\
&\quad \left[\frac{\rho}{\rho + 1} \alpha \mathbf{e}_c \mathbf{G} + \frac{1}{\rho + 1} \alpha^* \mathbf{e}_c \mathbf{G}^* + \frac{1}{\rho + 1} \beta^* \mathbf{e}_c \mathbf{G}^* \mathbf{L}^* + \right. \\
&\quad \left. \frac{1}{\rho + 1} \gamma^* \mathbf{e}_c \mathbf{G}^* \mathbf{P}^* - \frac{\rho^2}{(\rho + 1)^2} \alpha^2 \mathbf{e}_c \mathbf{G}^2 + \right. \\
&\quad \left. \frac{\rho}{(\rho + 1)^2} (\alpha^*)^2 \mathbf{e}_c \mathbf{G}^* \mathbf{G}^* + \frac{2\rho}{(\rho + 1)^2} |\alpha|^2 \mathbf{e}_c \text{Re}(\mathbf{G}^* \mathbf{G}) \right] (\boldsymbol{\Delta} \mathbf{H}_{avg}^{-1}).
\end{aligned} \tag{3.18}$$

Note that the row vectors $\mathbf{e}_c \mathbf{L} \mathbf{G}$ and $\mathbf{e}_c \mathbf{P} \mathbf{G}$ are zero vectors and discarded in the derivations.

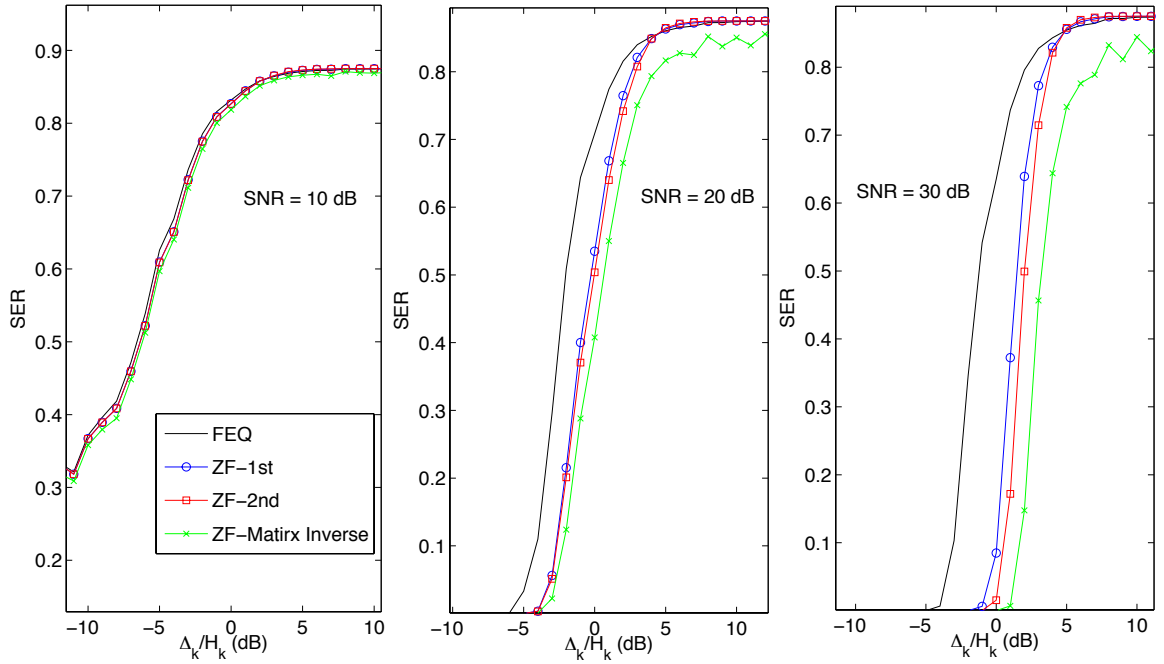


Figure 3.9: SER performance versus $|\Delta_k/H_k|$ at 10, 20 and 30 dB SNR.

3.3.3 ICI Indicator Threshold Setting

Since the PSA framework relies on the ICI indicator $|\Delta_k/H_k|$ to determine which ICI cancellation methods to use for each subcarrier, it is crucial to determine the thresholds against which the PSA framework compares the ICI indicator. The thresholds should be chosen for the PSA framework to operate robustly for a wide range of SNR. It can be done by comprehensive simulations. Define the residual interference plus noise at the ICI equalizer output as

$$\varepsilon(k) = S(k) - \hat{S}(k) = S(k) - \mathbf{w}_k \mathbf{r}_k. \quad (3.19)$$

The post-detection SINR at the ICI equalizer output is defined as

$$\text{SINR}_{post} = E[|\mathbf{H}_{avg} \mathbf{s}|^2 / |\varepsilon|^2] \quad (3.20)$$

where $\boldsymbol{\varepsilon} = [\varepsilon(0), \varepsilon(1), \dots, \varepsilon(N-1)]^T$. The approximate symbol error rate (SER) expression for rectangular M-QAM is

$$P_{SER} = 2 \left(1 - \frac{1}{\sqrt{M}}\right) Q \left(\sqrt{\frac{3}{M-1}} \text{SINR}_{post} \right) \quad (3.21)$$

where $Q(x) = \frac{1}{\sqrt{2\pi}} \int_x^\infty e^{-\frac{y^2}{2}} dy$.

With extensive simulations on SER for various SNRs and velocities, proper ICI indicator thresholds can be found by looking at when higher-order equalizers begin to provide performance benefits. A proper threshold setting should not deviate much from these observed forking points for a wide range of SNRs. With the same simulation setting as that in Section 3.2, Fig. 3.9 shows SER of PB-ZF ICI equalizers versus $|\Delta_k/H_k|$ at 350 km/h under 10, 20 and 30 dB SNR, respectively. It can be seen that when SNR is low, AWGN dominates and all ICI equalizers provide no significant benefits compared to conventional one-tap frequency domain equalizer (FEQ). When SNR becomes larger, the first-order PB-ZF ICI equalizer begins to outperform one-tap FEQ when $|\Delta_k/H_k| > -6$ dB and the second-order PB-ZF ICI equalizer excels the first-order one when $|\Delta_k/H_k| > -3$ dB. ZF Matrix Inversion outperforms the perturbation-based methods when $|\Delta_k/H_k| > 0$ dB. The threshold settings for PB-MMSE ICI equalizers can also be investigated in a similar way.

Note that the BER floor due to ICI starts to kick in around SNR = 20 dB and thus an appropriate threshold setting may be between -20 and -30 dB target residual ICI power. Furthermore, with a additional 3-dB margin, the threshold setting that four ranges (≤ -5 dB, $-5 \sim -3$ dB, $-3 \sim 0$ dB, and ≥ 0 dB) of $|\Delta_k/H_k|$ is a good choice for many realistic situations and adopted in the later simulations.

An alternative method to design the threshold is to calculate the theoretical residual ICI channel power of different-order equalizers. Recall that $(\boldsymbol{\Delta}\mathbf{H}_{avg}^{-1})\mathbf{G}$ contributes

to ICI. With $|G_i| \approx \frac{N}{2\pi N_S} \frac{1}{|i|}$, the residual ICI channel power of the p -th order PB equalizer is $[\frac{N}{2\pi N_S} \cdot |\Delta_k/H_k|^2 \cdot 2 \cdot \sum_{q=1}^Q (\frac{1}{q})^2]^{p+1}$. Then the proper combination of $|\Delta_k/H_k|$ and p is chosen for the residual ICI channel power to meet a pre-set level. Table 3.2 lists the upper bound of $|\Delta_k/H_k|$ for PB equalizers. The smaller the target power level is, the smaller the upper bound, and the higher order the perturbation is, the larger the upper bound.

The optimal threshold setting will also depend on the SNR; however, from experiences we found that the proposed threshold settings operate robustly for a wide range of SNR.

Table 3.2: Upper bound of ICI indicator, $10\log_{10}(\frac{|\Delta_k|}{|H_k|})$, given target residual ICI channel power levels and PB ICI equalizers

target residual ICI channel power	0-th order	1-st order	2-nd order
0.1 (-10 dB)	1.09	3.59	4.42
0.01 (-20 dB)	-3.91	1.09	2.76
0.001 (-30 dB)	-8.91	-1.41	1.09

3.3.4 CFR Matrix Inversion by Lookup Table

When the subcarrier experiences severe ICI, the approximate matrix inverse $\mathbf{I} - \mathbf{A} + \mathbf{A}^2 + \dots + \mathbf{A}^p$ adopted in PB-ZF and PB-MMSE ICI equalizers become a crude approximation and the error rate performance may degrade significantly. Hence, the exact matrix inverse, $(\mathbf{I} + \mathbf{A})^{-1}$, which demands high computational load is needed. Though the PB method is no longer appropriate, the localized CFR matrix approximated by polynomial functions as (3.12) is still accurate enough for the matrix inversion. We propose an LUT in which pre-calculated matrix inverses indexed by quantized param-

eters α , β and γ are stored and can be applied on the fly. The computational cost of matrix inverse is $\mathcal{O}(N^3)$ while the cost is reduced to $\mathcal{O}(N)$ by adopting the LUT approach.

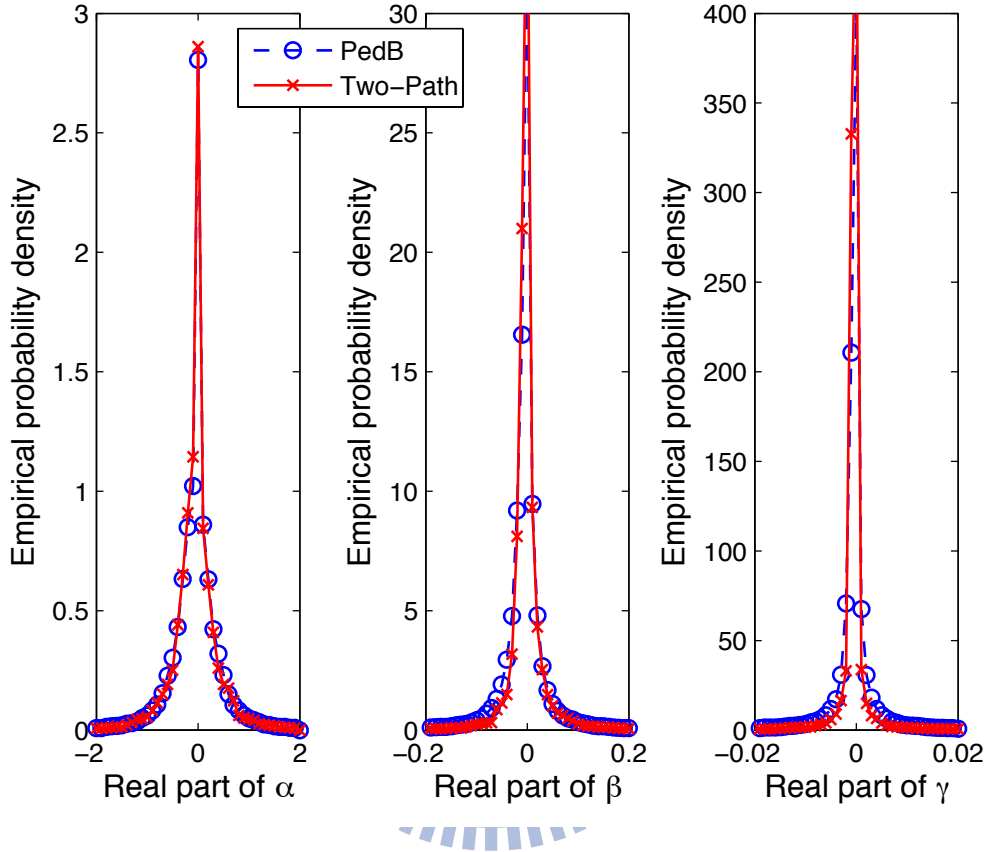


Figure 3.10: Empirical probability density functions of α , β and γ for two different channel PDPs: the ITU Pedestrian-B channel and a two-path equal-gain channel.

In practice, a trade-off between the number of quantization levels and the corresponding quantization error should be carefully designed to avoid performance degradation. By comprehensive computer simulations, the empirical probability density functions (PDFs) of α , β and γ for different channel PDPs at 350 km/h and for the ITU Pedestrian-B channel at different vehicle speeds are shown in Figs. 3.10 and 3.11 respectively. The empirical PDFs, like the ICI indicator, are insensitive to changes in channel PDPs. Furthermore, the empirical PDFs are quite concentrated; in fact, the

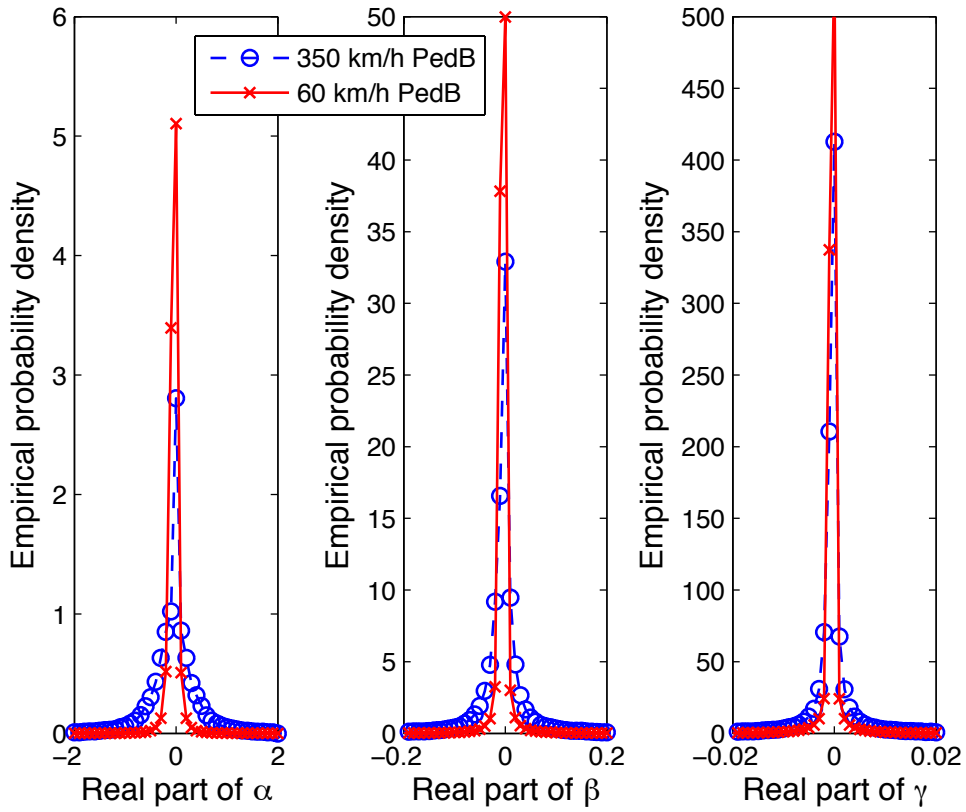


Figure 3.11: Empirical probability density functions of α , β and γ for the ITU Pedestrian-B channel at two different vehicle speeds: 350 km/h and 60 km/h.

lower the vehicle speed, the more concentrated they are. As a result, eight equally-spaced levels spanning from -2 to 2 is enough for quantizing α . Similarly, eight levels are used for quantizing β and γ . The total number of matrix inverses to be stored is 4096. For each matrix inverse, we only need to store the central row because the serial ICI equalizer is considered. For 12-bit fixed-point numerical resolution, the LUT size will be 16 KBytes. The detailed simulation results concerning the trade-off between BER performance and quantization levels will be provided in subsection 3.4.1.

It is worth noting that an LUT can always be used when matrix inversion is needed. However, without our transposed signal model in (2.37), the LUT approach will not be effective. For example, an LUT of matrix inversion for the signal model in

(2.35) needs to parameterize \mathbf{H}_{avg} and Δ in $[\mathbf{H}_{avg} + \mathbf{G}\Delta]^{-1}$. There will be two sets of parameters and two dynamic ranges to consider. Consequently, the resulted LUT will be too large to be effective.

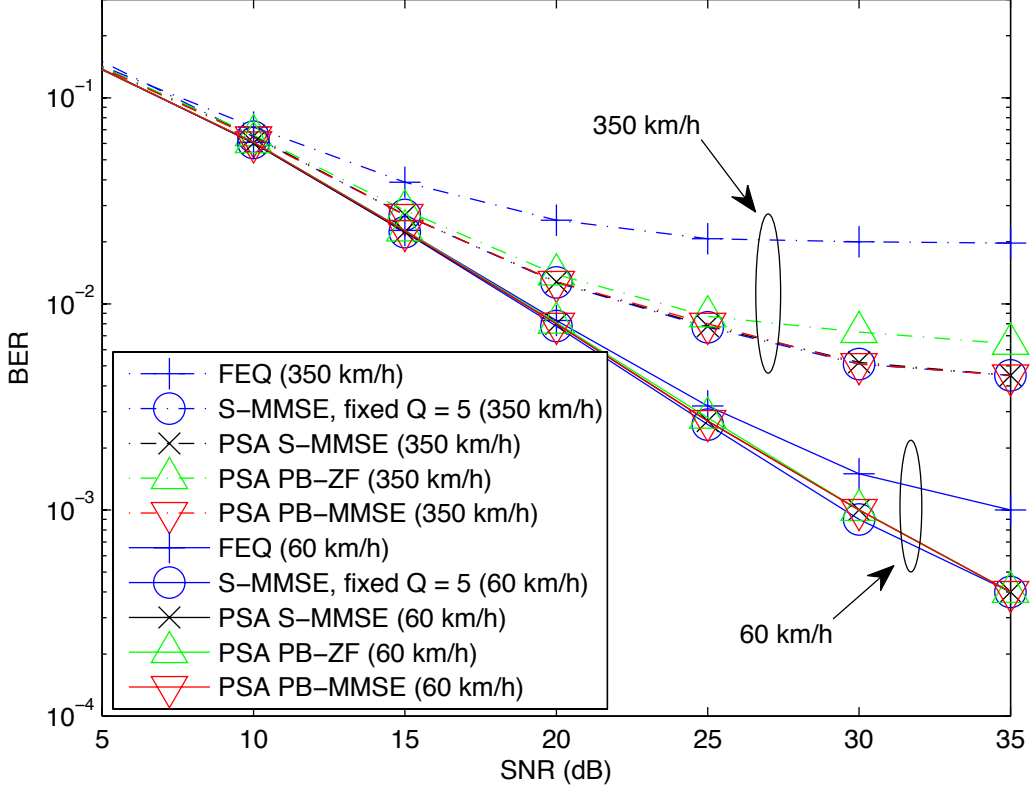


Figure 3.12: BER performance comparisons for ICI equalizers under 1024-point FFT, 16-QAM and the ITU Pedestrian-B channel model at 350 km/h and 60 km/h.

3.4 Performance Results and Discussions

3.4.1 BER Simulations

In this subsection, we investigate the performance and robustness of proposed ICI equalizers under different system parameters and channel conditions. Unless otherwise

stated, perfect channel state information (CSI) of the averaged CFR (H_k) is assumed. The ICI CFR, Δ_k , and the ICI indicator are estimated by the simple method mentioned in Section 3.2. First, with the same simulation set-up described in Section 3.2 with $N_A = 840$ active subcarriers, BER curves of different ICI equalizers at 60 km/h and 350 km/h are shown in Fig. 3.12. The serial MMSE (S-MMSE) ICI equalizer inverts for each subcarrier a local CFR sub-matrix whose size is $(2Q+1) \times (2Q+1)$ fixed for all subcarriers. The PSA ICI equalizers adjust Q according to the ICI indicator and the corresponding threshold setting is described in subsection 3.3.3. In Fig. 3.12, the PSA S-MMSE ICI equalizer with $Q \leq 5$ achieves, with lower complexity, the same BER as the conventional S-MMSE ICI equalizer with fixed $Q = 5$. Moreover, our PSA PB-MMSE ICI equalizers provide further complexity reduction without BER degradation, compared to the PSA S-MMSE ICI equalizers. Note that PB-ZF ICI equalizer suffers slightly performance degradation due to the noise enhancement effect. The results verify the effectiveness of the PSA PB ICI equalizers to improve the balance between performance and computational complexity. The results also indicate that the PSA approach is effective for different vehicle speeds. Intuitively this is expected, because the idea of PSA is to adjust the complexity of the ICI equalizer according to the ICI indicator, and the ICI indicator works fine regardless what the vehicle speed is. Moreover, as can be seen from Fig. 3.9, simple methods such as one-tap FEQ perform as good as sophisticated equalizers when $|\Delta_k/H_k|$ indicates little ICI. We conclude that the PSA approach works effectively for different vehicle speeds. Note that though Pedestrian-B channel PDP is used for the simulation, we also did some simulations with Vehicular-A channels and the results are similar to that of Pedestrian-B.

The impact due to the channel estimation error is also considered. Figure 3.13 shows the results under imperfect CSI. Follow the practice found in [11,61], the MSE of

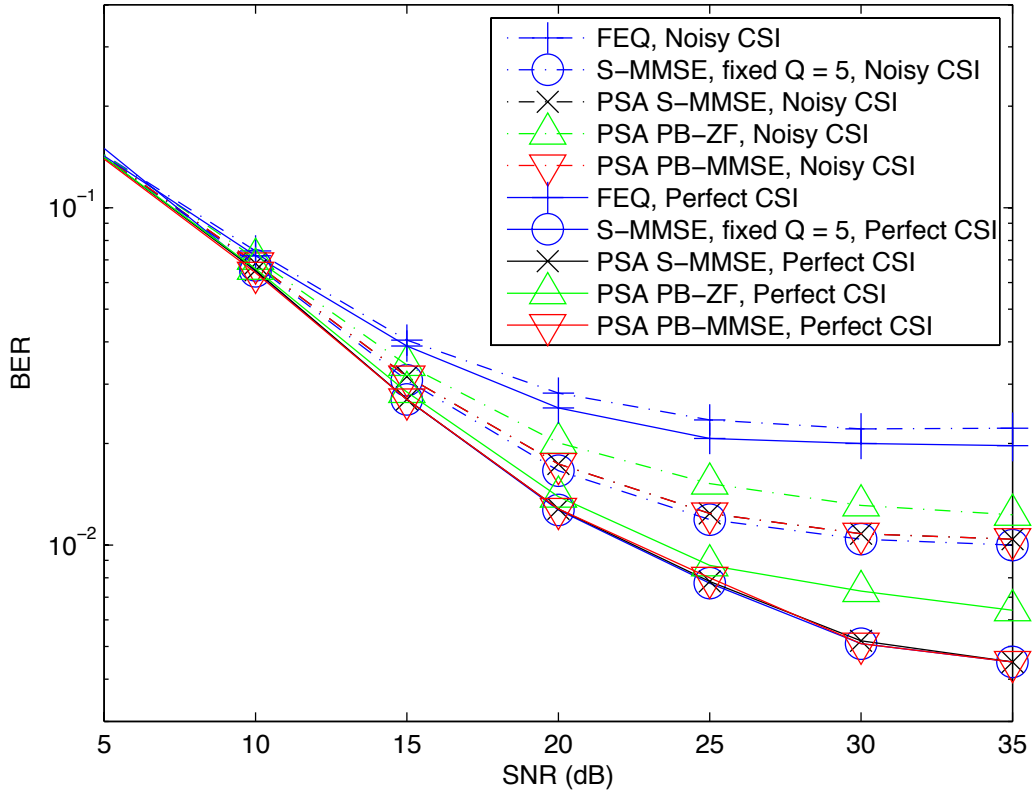


Figure 3.13: BER performance comparisons with -20 dB MSE channel estimation error at 350 km/h.

the channel estimation is set to -20 dB. The accuracy of channel estimation will effect the performance of any ICI cancellation methods. As for our method, there are two aspects that deserve discussion. The first is that it is built on a linear approximation of time-varying channels; therefore, it only requires estimating the averaged channel response, which is routinely done by OFDMA receivers in block-fading channels. The second is that, though the performance degradation is inevitable, our method is effected in a comparable way by which other linear methods, say, conventional S-MMSE ICI equalizers, are effected.

Next, we study how many quantization levels in LUT are enough for the PB ICI equalizers. From Fig. 3.14, it can be seen that an 8-levels LUT has the same

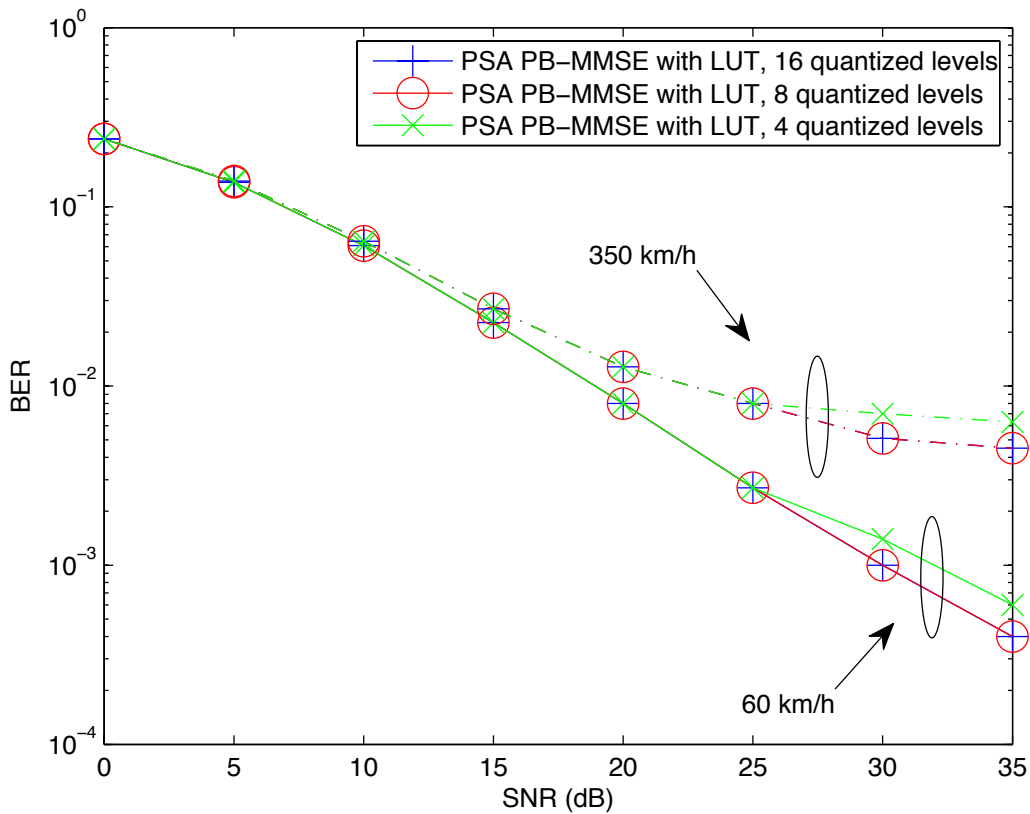


Figure 3.14: BER with different quantization levels LUT under the ITU Pedestrian-B channel at 350 and 60 km/h.

BER performance as a 16-level LUT, but a 4-level LUT will result in performance degradation. Consequently, an 8-level LUT is chosen for 350 km/h, i.e., the worst-case scenario, to make sure that it is enough for all speeds.

Finally, we consider the coded performance and compare the packet error rate (PER) of different ICI equalizers in Fig. 3.15. The modulation is 16-QAM and the channel coding is a rate-3/4 convolutional turbo code (CTC) that is mandatory in WiMAX [7]. Ten iterations of CTC decoding are conducted. Under this configuration, one packet consists of 44 bytes payload. The standard requires 10 % PER at 12 dB E_b/N_0 [64] where E_b/N_0 is defined as the SNR per bit. From Fig. 3.15, it can be seen that at 350 km/h the performances of linear equalizers are close to borderline.

Table 3.3: Complexity comparison.

Methods	Complexity	Number of complex flops
Ideal B-MMSE	$\mathcal{O}(N_A^3)$	4×10^8
Conventional Fixed Q S-MMSE	$\mathcal{O}(Q^3 N_A)$	745360 ($Q = 5$), 408240 ($Q = 4$), 192080 ($Q = 3$)
PSA Variable $Q \leq 5$ S-MMSE	$\sum_i \mathcal{O}(Q_i^3 N_A)$	162334 (350 km/h), 14301 (60 km/h)
PSA PB-ZF with LUT	$\mathcal{O}(Q N_A)$	68388 (350 km/h), 6822 (60 km/h)
PSA PB-MMSE with LUT	$\mathcal{O}(Q N_A)$	93883 (350 km/h), 10340 (60 km/h)

The S-MMSE with fixed $Q = 5$ and our PSA PB-MMSE offer the best performances with a very tight margin to spare. This demonstrates the value of our approach. The PSA equalizer can opt for a higher upper limit on Q with a reasonable increase in complexity, if a larger performance margin is required. But for a fixed- Q equalizer, the option to increase Q may be not feasible.

3.4.2 Computational Complexity

The computational complexity is measured in complex floating point operations (flops) and summarized in Table 3.3. The reduction of computational cost by our PSA framework incorporating PB-ZF/PB-MMSE equalizers and matrix inversion with LUT is shown. The calculation of equalizer coefficients dominates the computational cost. The ideal Block MMSE (B-MMSE) ICI equalizer inverts the whole $N_A \times N_A$ CFR matrix and requires $2N_A^3/3 \approx 4 \times 10^8$ flops which is unaffordably high, and the con-

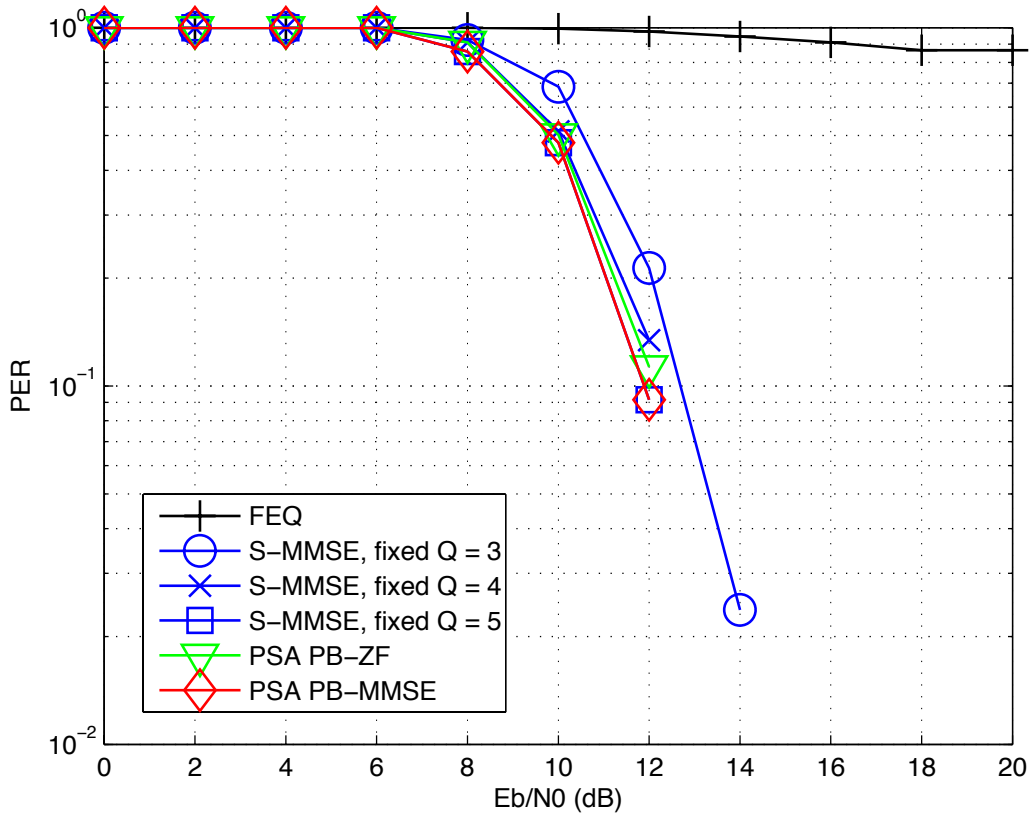


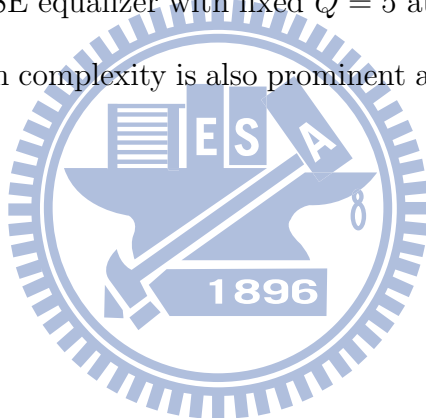
Figure 3.15: PER comparison for different $Q = 3, 4$ and 5 under the ITU Pedestrian-B channel at 350 km/h. 16-QAM and rate-3/4 CTC are used.

ventional S-MMSE ICI equalizer needs about $2(2Q + 1)^3 N_A / 3 \approx 7.5 \times 10^5$ flops with $Q = 5$. They are used as benchmarks for comparison.

We then consider the complexity of proposed PSA approaches. Notice that the complexity of calculation of the ICI indicator is one complex division per subcarrier and has been included in Table 3.3. Define Q_i as the value of Q chosen in the i -th $|\Delta_k/H_k|$ range and N_i as the number of subcarriers in that range. For example, in PSA S-MMSE equalizers, at the first stage ($Q_1 = 0$), there are $N_1 = 0.393N_A$ of subcarriers that use one-tap FEQ and, at the last stage ($Q_4 = 5$), there are $N_4 = 0.152N_A$ of subcarriers that use 11×11 matrix inversion resulting in the complexity of $\mathcal{O}(Q_4^3 N_4)$. Overall, its complexity is $\sum_{i=1}^4 \mathcal{O}(Q_i^3 N_i)$, which leads to 1.6×10^5 flops at 350 km/h,

about 4.5 times lower than that of the banded S-MMSE with fixed $Q = 5$.

The PSA PB-ZF and PB-MMSE ICI equalizers achieve big savings with their complexity in $\mathcal{O}(QN_A)$. In practice, PB-ZF and PB-MMSE ICI equalizers are used for subcarriers inflicted by mild ICI, while the LUT matrix inversion is used to combat severe ICI. For each subcarrier, the first-order PB-ZF requires $8Q + 7$ flops and the second-order PB-ZF requires $12Q + 12$ flops due to one and two Q -tap fixed FIR filters, respectively. Similarly, the first-order PB-MMSE requires $28Q + 23$ flops and the second-order PB-MMSE requires $36Q + 31$ flops. Overall, the complexity of PB-ZF and PB-MMSE with LUT matrix inversion are about 11 and 8 times lower than that of the conventional S-MMSE equalizer with fixed $Q = 5$ at 350 km/h. Furthermore, it can be seen that the save in complexity is also prominent at lower speed, say, 60 km/h.



Chapter 4 On the Diversity Order of BICM-OFDM Systems over Doubly Selective Fading Channels

4.1 Introduction

While ICI may cause performance degradation if left untreated [65], fully utilizing the ICI terms at the receiver may actually improve the error rate, compared to the performance with quasi-static channels [9,12,28]. Simulation results also reveal that the performance gain comes from increasing diversity. Combined with BICM, OFDM systems can achieve a high diversity order in a frequency selective, but not time-selective, fading channels efficiently, say, by using convolutional codes and Viterbi decoding [27]. As BICM-OFDM have been widely used in many wireless mobile communication systems. It is interesting to investigate the performance in doubly-selective fading channels. Huang *et al.* [1] applied bit-interleaving across several time and frequency slots in BICM-OFDM systems and demonstrated by simulations that the performance gain is due to time-varying channels. This performance improvement can be recognized as the time diversity gain obtained by exploiting the time-varying nature of the channel.

In this chapter, we focus on the diversity order of BICM-OFDM system over doubly selective, time- and frequency-selective, fading channels. To simplify the analysis, we only consider the conventional BICM structure without any kind of precoding. The further consideration of BICM systems with precoding can be left as a future work.

In Section 4.2, first, we derive the asymptotic diversity order of BICM-OFDM

systems by studying the role of correlation in rank analysis of the typical derivation of diversity order. The results also show that BICM-OFDM achieves the maximum diversity order given in [29]. While the diversity order of a BICM-OFDM system in the frequency selective fading channels is $\min(L, d_{\text{free}})$ where L is the multipath numbers and d_{free} is the minimum free distance of the channel code, the maximum diversity order in the doubly-selective fading channels becomes $\min(r_T L, d_{\text{free}})$. As d_{free} of the channel code usually can be very high, the diversity order is further increased by a factor r_T due to the time diversity. Second, the effect of significant eigenvalues of the channel correlation matrix and the diversity order in realistic situations with moderate SNRs are examined by studying the channel correlation function and its Fourier dual. Finally in Section 4.3, our analysis framework is extended to multiple input multiple output (MIMO) cases while incorporating more diversity techniques, such as cyclic delay diversity (CDD) and phase-roll diversity (PRD) [30]. This MIMO extension can also be applied in a distributed fashion, for example, in cooperative communications [31].

It is worth to mention that when we derived the diversity order of BICM-OFDM over doubly selective fading channels, we focused on the benefits of time-varying channels and assumed that the problems possibly caused by ICI can be handled by the receiver, i.e., the receiver can utilize ICI properly in order to achieve the diversity gain and that is exactly what has been demonstrated in our simulations. Note that various degrees of channel state information (CSI) knowledge are assumed in the aforementioned works; in our work, a moderate task of channel estimation is required in the sense that only the average of the time varying channel in each OFDM symbol time is needed for the receiver to function. Although in recent years the study of channel estimation (CE) of OFDM over doubly selective channels has been very ac-

tive [11,13,66,67], details of conducting CE is beyond the scope of this work.

Research in the BICM has become very active and of importance and recent developments of BICM include the precoder design [68–71] (and the references therein), labeling rule design [72,73], extension to MIMO to achieve better performance in terms of coding gain or/and diversity gain. However, the precoder design usually requires the knowledge of channel state information at the transmitter (CSIT) and the corresponding maximum likelihood precoder decoding exhibits high complexity. Labeling rule will affect the coding gain but not the diversity gain. In summary, the performance of BICM is complicated and affected by many parameters, i.e., channel code, interleaver, mapper, constellation, preprocessing (e.g., precoding, signal space diversity, constellation rotation, etc.), the underlying channel, and demapping/decoding strategy. Consequently, the design of optimum algorithm is complicated and diverse, also the fair comparison is difficult.

As for the maximum diversity order over doubly selective fading channels, it is derived for general block transmission systems without forward error-correcting code and a DFT-based precoding system relied on the basis expansion model of the channel is proposed to achieve the diversity order by Ma and Giannakis [29]. In a further development [74], a DFT-based receiver is proposed for such systems. The optimal precoding/decoding combination, however, may not be easily obtained in practical situations. For BICM-OFDM systems, a theoretical analysis of the diversity order over doubly selectively fading channels has not appeared in the literature. It motivate us to provide such analysis and the maximum diversity order of BICM-OFDM over doubly selective fading channels is derived. The results shows that BICM-OFDM achieves the maximum diversity order given in [29].

4.2 Diversity Order Analysis

4.2.1 System Model

This chapter considers coded OFDM systems and the benefits by utilizing multiple OFDM symbols so that we reformulate the system model correspondingly. A block diagram of the BICM-OFDM system under study is shown in Fig. 4.1. Information bits \mathbf{i}_n are first encoded by a channel encoder and the coded bits $\mathbf{c}_n \in \mathcal{C}$ are passed to the interleaver Π , where \mathcal{C} is the set of all possible codewords. The interleaved bits \mathbf{c}'_n are divided into P blocks and modulated using QAM or PSK where γ bits are mapped into one of totally 2^γ constellation points. Finally, an N -point inverse discrete Fourier transform generates the transmitted OFDM signal \mathbf{x}_n . The size of the interleaver is γNP bits. Note that the encoded bits are interleaved across several OFDM symbols as in [1] (which calls it time-frequency interleaving). Consider time-varying dispersive channels and the sampled baseband equivalent received signal $y_p(k)$ of the p -th OFDM symbol is

$$y_p(k) = \sum_{l=0}^{L-1} h_p(k; l)x_p(k-l) + w_p(k) \quad (4.1)$$

where $h_p(k; l)$ represents the l -th delay path of the multipath Rayleigh fading channel at the k -th sampling instant of the p -th OFDM symbol with $\text{E}[\sum_{l=0}^{L-1} |h_p(k; l)|^2] = 1$, L is the number of multipaths, $x_p(k)$ is the transmitted signal, and $w_p(k)$ is the additive white Gaussian noise (AWGN). The channel $\{h_p(k; l)\}$ is assumed to WSSUS. The autocorrelation function (ACF) of the channel in time for the l -th path is defined as $r(m) = \text{E}[h_p(k; l)h_{p+m}^*(k; l)]$.

Assume the CP is long enough to prevent inter-symbol interference and the synchronization is perfect. The received symbol in the frequency domain after CP removal

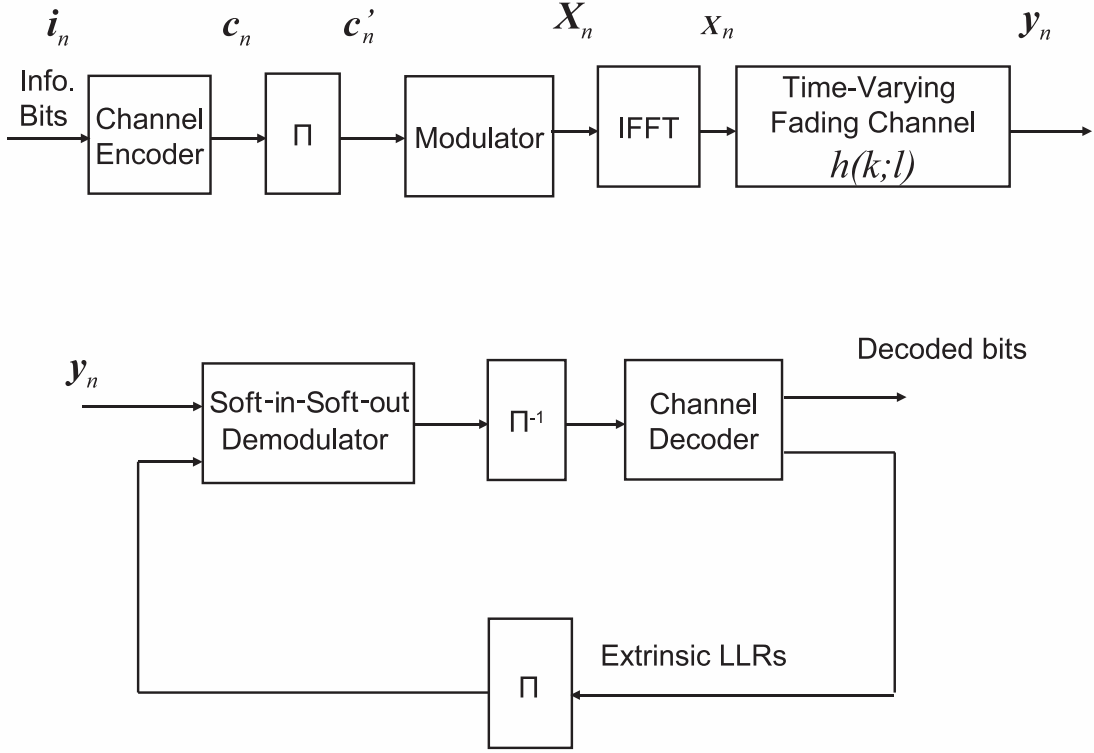


Figure 4.1: Block diagram of the transmitter and receiver of the considered system. Soft-input soft-output (Soft-in-Soft-out) demodulator consists of the ICI equalization such as the feedback canceller [1] and demapper.

is

$$\mathbf{y}_p = \mathbf{F}\mathbf{H}_p\mathbf{F}^H\mathbf{x}_p + \mathbf{w}_p \triangleq \mathbf{G}_p\mathbf{x}_p + \mathbf{w}_p, \quad p = 1, 2, \dots, P, \quad (4.2)$$

where $\mathbf{y}_p = [Y(N_p), Y(N_p + 1), \dots, Y(N_p + N - 1)]^T \in \mathbb{C}^{N \times 1}$ is the frequency-domain signal after DFT, $N_p = (p - 1)N$ marks the starting point of the p -th OFDM symbol, $[\mathbf{F}]_{k,n} = (1/\sqrt{N})e^{-j2\pi nk/N}$ is the (k, n) -th element in the DFT matrix \mathbf{F} , $\mathbf{x}_p = [X(N_p), X(N_p + 1), \dots, X(N_p + N - 1)]^T \in \mathbb{C}^{N \times 1}$ is the transmitted coded signal in the frequency domain with the average power normalized to one, $\mathbf{w}_p = [W(N_p), W(N_p + 1), \dots, W(N_p + N - 1)]^T \in \mathbb{C}^{N \times 1}$ represents the noise, and $\mathbf{H}_p \in \mathbb{C}^{N \times N}$ is the channel

impulse response matrix given by

$$[\mathbf{H}_p]_{i,j} = h_p(i; (i-j) \bmod N), \quad i, j = 0, 1, \dots, N-1. \quad (4.3)$$

Note that the CIR $h_p(k; l)$ is zero when $l \leq 0$ or $l \geq L-1$. The off-diagonal terms in \mathbf{G}_p are the ICI coefficients, where the (r, s) -th element can be expressed as

$$\begin{aligned} [\mathbf{G}_p]_{r,s} &= \frac{1}{N} \sum_{k=0}^{N-1} \sum_{l=0}^{L-1} h_p(k; l) \exp(j2\pi k(s-r)/N) \\ &\quad \times \exp(-j2\pi sl/N). \end{aligned} \quad (4.4)$$

The channel matrix \mathbf{G}_p can be decomposed as $\mathbf{G}_p = \mathbf{G}_p^d + \mathbf{G}_p^o$, where \mathbf{G}_p^d contains the diagonal terms of \mathbf{G}_p and \mathbf{G}_p^o consists all the off-diagonal terms of \mathbf{G}_p . Note that \mathbf{G}_p^d corresponds to the DFT of $\tilde{\mathbf{h}}_p = [\tilde{h}_p(0), \dots, \tilde{h}_p(L-1)]^T$, the *averaged* CIR in the p -th OFDM symbol, i.e., $\tilde{h}_p(l) = \frac{1}{N} \sum_{k=0}^{N-1} h_p(k, l)$. Meanwhile \mathbf{G}_p^o contributes to ICI terms. We can rewrite (4.2) as

$$\mathbf{y}_p = \mathbf{G}_p^d \mathbf{x}_p + \mathbf{G}_p^o \mathbf{x}_p + \mathbf{w}_p \triangleq \text{diag}(\mathbf{x}_p) \mathbf{F}_{N \times L} \tilde{\mathbf{h}}_p + \mathbf{z}_p \quad (4.5)$$

where $\mathbf{F}_{N \times L}$ is an $N \times L$ matrix composed of the first L columns of \mathbf{F} and \mathbf{z}_p denotes the interference-plus-noise terms.

The variation of doubly selective fading channels within one or across several OFDM symbols can provide some benefits. The intra-symbol channel variation also causes ICI. It has been observed that the diversity order slightly increases if ICI is utilized at the receiver [9,11,12,18] but the high complexity remains a concern. In this work, we focus on the much more pronounced benefit provided by the inter-symbol channel variation, assuming that ICI is handled by simple techniques such as the decision-feedback canceller [1] with FEC to improve the decision accuracy. In particular, we assume that any *residual* ICI will not ruin the possible diversity gain provided by inter-symbol channel variation. This assumption is reasonable even if the

normalized Doppler frequency $f_d T_S$ (T_S is one OFDM symbol duration) is as high as 0.1 about which many ICI mitigation methods can reach around 30 dB of signal-to-interference-ratio without the help of FEC [13,15]. As a result, the error floor due to residual ICI will not kick in until a very high SNR.

With this focus in mind, the stacked received signal $\mathbf{y} = [\mathbf{y}_1^T, \mathbf{y}_2^T, \dots, \mathbf{y}_P^T]^T$ can be given as

$$\mathbf{y} = \mathbf{X}(\mathbf{I}_P \otimes \mathbf{F}_{N \times L})\mathbf{h} + \mathbf{z} \triangleq \mathbf{X}\mathbf{h}_{eq} + \mathbf{z} \quad (4.6)$$

in which $\mathbf{h}_{eq} \triangleq (\mathbf{I}_P \otimes \mathbf{F}_{N \times L})\mathbf{h}$, \mathbf{I}_P is a $P \times P$ identity matrix, \otimes denotes the Kronecker product, \mathbf{h} is a length- PL vector defined as $\mathbf{h} = [\tilde{\mathbf{h}}_1^T, \tilde{\mathbf{h}}_2^T, \dots, \tilde{\mathbf{h}}_P^T]^T$, \mathbf{X} is a $PN \times PN$ diagonal data signal matrix given by $\mathbf{X} = \text{diag}(X(0), \dots, X(N-1), X(N), \dots, X(2N-1), \dots, X(PN-1))$ and \mathbf{z} is a $PN \times 1$ noise vector representing the residual ICI plus noise.

4.2.2 Asymptotic Analysis

In this subsection, we derive the asymptotic diversity order of BICM-OFDM by first bounding the pairwise error probability (PEP). Let \mathbf{X} be the coded transmit signal corresponding to codeword \mathbf{c} and $\hat{\mathbf{X}}$ be the detected signal corresponding to codeword $\hat{\mathbf{c}}$ where $\mathbf{c} \neq \hat{\mathbf{c}}$. In order to gain diversity, we adopt the assumption in [27] that the interleaver can disperse d consecutive coded bits to different symbols and onto different OFDM subcarriers whereas d bits cover the span of consecutive trellis branches on which d_{free} distinct bits of any two codewords occur. The assumption can be satisfied by practical interleavers, for instance, the block interleaver of IEEE 802.11a [34]. Assume that \mathbf{z} is complex Gaussian distributed with zero mean and variance N_0 . Evoke the maximum-likelihood (ML) decision rule and the conditional error probability $P(\mathbf{c} \rightarrow$

$\hat{\mathbf{c}}|\mathbf{h}$ is $P(\|\mathbf{z}\|^2 \geq \|\mathbf{z} + (\mathbf{X} - \hat{\mathbf{X}})\mathbf{h}_{eq}\|^2|\mathbf{h})$. It can be expressed by the Q -function as

$$Q\left(\frac{\|(\mathbf{X} - \hat{\mathbf{X}})\mathbf{h}_{eq}\|^2}{\sqrt{2N_0}\|(\mathbf{X} - \hat{\mathbf{X}})\mathbf{h}_{eq}\|^2}\right) = Q\left(\sqrt{\frac{1}{2N_0}}\|(\mathbf{X} - \hat{\mathbf{X}})\mathbf{h}_{eq}\|\right) \quad (4.7)$$

where $Q(x) = \frac{1}{\sqrt{2\pi}} \int_x^\infty e^{-\frac{y^2}{2}} dy$.

The PEP is obtained by ensemble averaging:

$$\begin{aligned} P(\mathbf{c} \rightarrow \hat{\mathbf{c}}) &= \mathbb{E} \left[Q \left(\sqrt{\frac{1}{2N_0}} \|(\mathbf{X} - \hat{\mathbf{X}})\mathbf{h}_{eq}\| \right) \right] \\ &= \mathbb{E} \left[Q \left(\sqrt{\frac{\text{SNR} \cdot \mathbf{h}_{eq}^H \mathbf{D}^H \mathbf{D} \mathbf{h}_{eq}}{2}} \right) \right] \end{aligned} \quad (4.8)$$

where $\text{SNR} = 1/N_0$ since the average power of channel and transmitted signal are normalized to one and $\mathbf{D} = \mathbf{X} - \hat{\mathbf{X}}$ is the coded symbol difference matrix. According to the assumption of the interleaver, at least d_{free} non-zero terms exist in \mathbf{D} [27]. In the following we consider the worst case that only d_{free} terms are non-zero in \mathbf{D} and each of these terms has Euclidean distance d_{min} . Note that the parameters of BICM-OFDM are usually chosen as $N \geq L$ and $N \geq d_{\text{free}}$.

A typical PEP analysis such as those in [27,32] assumes that the vector \mathbf{h}_{eq} has independent elements and the rank analysis is focused on the term $\mathbf{D}^H \mathbf{D}$. Here, however, the correlation of channels over several OFDM symbols needs to be considered. We adopt the approach in [29] to extract the statistical independent components in \mathbf{h}_{eq} which are considered as the source of diversity. After this extraction the usual PEP analysis can proceed.

Assume the Kronecker model [30,70,71] for the channel, i.e., the channel autocorrelation matrix can be decoupled as

$$\mathbf{R} = \mathbb{E}[\mathbf{h}\mathbf{h}^H] = \mathbf{\Phi}_T \otimes \mathbf{\Phi}_L \quad (4.9)$$

where $\mathbf{\Phi}_T$ is the $P \times P$ time autocorrelation matrix constructed by stacking the windowed ACFs, that is, the k -th row $[\mathbf{\Phi}_T]_{k,1:P} = [r(1-k), r(2-k), \dots, r(P-k)]$. $\mathbf{\Phi}_L$

is the $L \times L$ path gains autocorrelation matrix and constructed as a diagonal matrix $\text{diag}(\sigma_0^2, \sigma_1^2, \dots, \sigma_{L-1}^2)$ due to the uncorrelated scattering assumption where σ_l^2 denotes the power of the l -th path.

The rank of \mathbf{R} can be evaluated through [75, Fact 7.4.20]

$$\begin{aligned} \text{rank}(\mathbf{R}) &= \text{rank}(\mathbf{\Phi}_T \otimes \mathbf{\Phi}_L) \\ &= \text{rank}(\mathbf{\Phi}_T) \times \text{rank}(\mathbf{\Phi}_L) = r_T \times L \end{aligned} \quad (4.10)$$

where r_T and L are the ranks of $\mathbf{\Phi}_T$ and $\mathbf{\Phi}_L$, respectively. Note that $r_T \times L$ is bounded by $P \times L$. The autocorrelation matrix of \mathbf{h}_{eq} is $\mathbf{R}_{eq} = \text{E}[\mathbf{h}_{eq}\mathbf{h}_{eq}^H] = (\mathbf{I}_P \otimes \mathbf{F}_{N \times L})\text{E}[\mathbf{h}\mathbf{h}^H](\mathbf{I}_P \otimes \mathbf{F}_{N \times L})^H = (\mathbf{I}_P \otimes \mathbf{F}_{N \times L})\mathbf{R}(\mathbf{I}_P \otimes \mathbf{F}_{N \times L})^H$. Since $\mathbf{F}_{N \times L}$ has full rank L , the matrix $(\mathbf{I}_P \otimes \mathbf{F}_{N \times L})$ also has full rank PL . Therefore, by the rank property of matrix products [75, Proposition 2.6.2]¹, the rank of \mathbf{R}_{eq} is

$$\begin{aligned} \text{rank}(\mathbf{R}_{eq}) &= \text{rank}((\mathbf{I}_P \otimes \mathbf{F}_{N \times L})\mathbf{R}(\mathbf{I}_P \otimes \mathbf{F}_{N \times L})^H) \\ &= \text{rank}(\mathbf{R}) = r_T \times L. \end{aligned} \quad (4.11)$$

The eigenvalue decomposition is used to extract the statistically independent components in \mathbf{h}_{eq} . Consider $\mathbf{R}_{eq} = \mathbf{V}\mathbf{\Sigma}_h\mathbf{V}^H$ where \mathbf{V} is a $PN \times r_T L$ matrix satisfying $\mathbf{V}^H\mathbf{V} = \mathbf{I}_{r_T L}$ and $\mathbf{\Sigma}_h = \text{diag}(\xi_1^2, \dots, \xi_{r_T L}^2)$. In the following analysis, \mathbf{h}_{eq} is substituted by $\mathbf{V}\mathbf{\Sigma}_h^{\frac{1}{2}}\bar{\mathbf{h}}_{eq}$ where $\bar{\mathbf{h}}_{eq}$ is the $r_T L \times 1$ normalized equivalent channel vector containing independent and identically distributed (i.i.d.) zero-mean complex Gaussian random variables with unit variance. It can be shown that the PEP is not affected by this substitution, since \mathbf{h}_{eq} and $\mathbf{V}\mathbf{\Sigma}_h^{\frac{1}{2}}\bar{\mathbf{h}}_{eq}$ have identical distributions which is known as the isotropy property of the standard Gaussian random vector.

¹Proposition 2.6.2 in [75]: Let $\mathbf{A} \in \mathbb{C}^{n \times m}$, and let $\mathbf{C} \in \mathbb{C}^{k \times n}$ be left invertible (or equivalently, $\text{rank}(\mathbf{C}) = n$) and $\mathbf{B} \in \mathbb{C}^{m \times l}$ be right invertible (or equivalently, $\text{rank}(\mathbf{B}) = m$), then $\text{rank}(\mathbf{A}) = \text{rank}(\mathbf{CA}) = \text{rank}(\mathbf{AB})$. It is straightforward that $\text{rank}(\mathbf{CAB}) = \text{rank}(\mathbf{A})$. Since $\text{rank}(\mathbf{I}_P \otimes \mathbf{F}_{N \times L}) = \text{rank}((\mathbf{I}_P \otimes \mathbf{F}_{N \times L})^H) = PL$, (4.11) can be obtained by designating $\mathbf{C} = (\mathbf{I}_P \otimes \mathbf{F}_{N \times L})$, $\mathbf{A} = \mathbf{R}$, and $\mathbf{B} = (\mathbf{I}_P \otimes \mathbf{F}_{N \times L})^H$.

The term $\mathbf{h}_{eq}^H \mathbf{D}^H \mathbf{D} \mathbf{h}_{eq}$ in (4.8) now becomes $\bar{\mathbf{h}}_{eq}^H (\boldsymbol{\Sigma}_h^{\frac{1}{2}})^H \mathbf{V}^H \mathbf{D}^H \mathbf{D} \mathbf{V} \boldsymbol{\Sigma}_h^{\frac{1}{2}} \bar{\mathbf{h}}_{eq}$ in which the central part $(\boldsymbol{\Sigma}_h^{\frac{1}{2}})^H \mathbf{V}^H \mathbf{D}^H \mathbf{D} \mathbf{V} \boldsymbol{\Sigma}_h^{\frac{1}{2}}$ is a Hermitian matrix and can be diagonalized as $(\boldsymbol{\Sigma}_h^{\frac{1}{2}})^H \mathbf{V}^H \mathbf{D}^H \mathbf{D} \mathbf{V} \boldsymbol{\Sigma}_h^{\frac{1}{2}} = \mathbf{U} \boldsymbol{\Lambda} \mathbf{U}^H$ where \mathbf{U} is unitary, r_{TV} is its rank, and $\boldsymbol{\Lambda} = \text{diag}\{\lambda_1, \dots, \lambda_{r_{TV}}\}$ contains the eigenvalues. Moreover, define $\check{\mathbf{h}} = \mathbf{U}^H \bar{\mathbf{h}}_{eq}$ and notice that $\check{\mathbf{h}}$ is i.i.d. complex Gaussian with zero mean and unit variance since \mathbf{U} is unitary. Equation (4.8) becomes

$$\begin{aligned} P(\mathbf{c} \rightarrow \hat{\mathbf{c}}) &= \text{E} \left[Q \left(\sqrt{\frac{\text{SNR} \cdot \check{\mathbf{h}}^H \boldsymbol{\Lambda} \check{\mathbf{h}}}{2}} \right) \right] \\ &= \text{E} \left[Q \left(\sqrt{\frac{\text{SNR}}{2} \sum_{n=1}^{r_{TV}} \lambda_n |\check{h}_n|^2} \right) \right] \end{aligned} \quad (4.12)$$

where \check{h}_n is the n -th element in $\check{\mathbf{h}}$ and $|\check{h}_n|^2$ is Rayleigh distributed. The PEP is bounded by [32],

$$\begin{aligned} P(\mathbf{c} \rightarrow \hat{\mathbf{c}}) &\leq \text{E} \left[\exp \left(-\frac{\text{SNR}}{4} \sum_{n=1}^{r_{TV}} \lambda_n |\check{h}_n|^2 \right) \right] \\ &= \frac{1}{\prod_{n=1}^{r_{TV}} [1 + (\lambda_n \text{SNR}/4)]}. \end{aligned} \quad (4.13)$$

When SNR is large enough, the bound in (4.13) can be further simplified to:

$$P(\mathbf{c} \rightarrow \hat{\mathbf{c}}) \leq \left(\prod_{n=1}^{r_{TV}} \lambda_n \right)^{-1} \left(\frac{\text{SNR}}{4} \right)^{-r_{TV}}. \quad (4.14)$$

And it follows that the asymptotic diversity order is r_{TV} . As for the value of r_{TV} , since $\mathbf{V} \boldsymbol{\Sigma}_h^{\frac{1}{2}}$ has rank $r_T L$ and the diagonal matrix \mathbf{D} has rank d_{free} , it follows that $r_{TV} \leq \min(r_T L, d_{\text{free}})$, that is, the maximum asymptotic diversity order is no larger than $\min(r_T L, d_{\text{free}})$.

4.2.3 Practical Diversity Gains

Next, we consider the slope of the BER curve that is observed in more *realistic situations*. The full slope of $r_{TV} = \min(r_T L, d_{\text{free}})$ from asymptotic analysis is achieved

when SNR approaches infinity. In practical situations, smaller eigenvalues of \mathbf{R}_{eq} may not have the opportunity to contribute to steepening the slope before the effect of other impairments, such as residual ICI, kicks in. As a result, the actual slope observed at moderate SNR will not be as large as the asymptotic slope. A similar phenomenon caused by dominant eigenvalues in the context of channel estimation has also been reported [66].

Simulations are conducted to demonstrate the effect of the relative sizes of eigenvalues on the observed slope. Consider a BICM-OFDM system over a block fading channel. Here we did not use doubly selective fading channels because the magnitudes of eigenvalues need to be controlled to show their effects, and it is very difficult to do so for a doubly selective fading channel; while in a block fading channel, it can be easily done by setting the path gains. Fig. 4.2 shows two BER curves under two-multipath ($L = 2$) Rayleigh block fading channel with two different path-gain settings. The system uses 8-PSK modulation, the DFT size is 64, $P = 2$, and a rate-1/2 convolutional code with the generator polynomial [133; 171] ($d_{\text{free}} = 10$) is adopted such that the diversity order is not limited by d_{free} . 10^5 channel realizations are simulated. Two settings of eigenvalues of Φ_L are used; the first consists of (0.995, 0.05), and the second (0.5, 0.5). The full slope is -4 for both cases, but for the first setting, we expect the slope will only reach -2 when the SNR is moderate, since only one eigenvalue is significant. As can be seen from Fig. 4.2, in the SNR range from 10 to 20 dB, the slopes are -2 and -4 respectively, and the first setting's slope does not reach -4 until around SNR = 25 dB.

The relation between the practical diversity order and the channel autocorrelation function can be further expounded. Consider the number of significant eigenvalues of \mathbf{R}_{eq} in (4.11). Since \mathbf{R}_{eq} can be approximated to be circulant when N is large, its

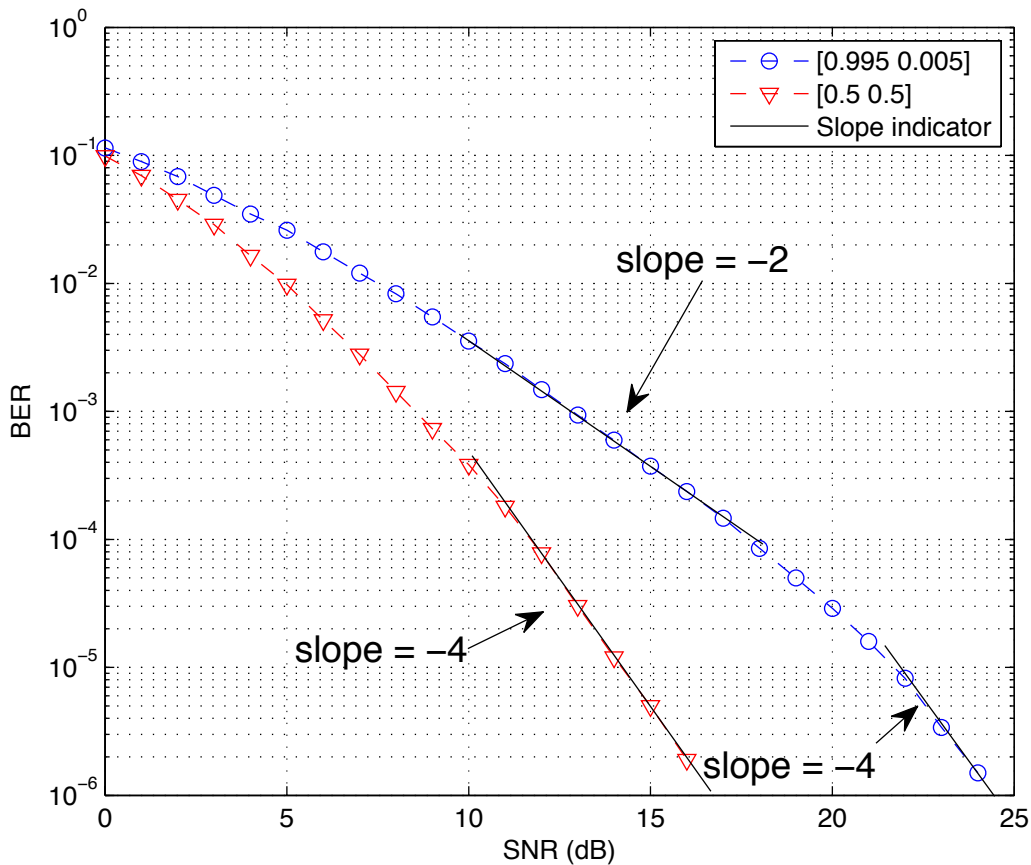


Figure 4.2: BER performance with 8-PSK modulation under two-multipath ($L = 2$) Rayleigh block fading channels with two different path-gain distributions. The DFT size is 64, $P = 2$, and a rate-1/2 convolutional code with the generator polynomial [133; 171] ($d_{\text{free}} = 10$) is adopted. 10^5 channel realizations are simulated.

eigenvalues can be obtained by applying DFT to it. It is essentially time-windowing the channel ACF, doing Fourier transform, and sampling the result. Therefore, the faster the channel changes, the narrower the ACF becomes relative to the observation window (the code block length), and a wider Fourier dual and more significant samples follow. Consequently the diversity order gets larger. Two contrasting examples are shown in Fig. 4.3 where the observed Doppler spectra are obtained by convolving the Doppler spectra with a sinc function, corresponding to the Fourier transform of time-windowed

channel ACFs. After obtaining the observed Doppler spectra, the eigenvalues can be obtained by sampling them.

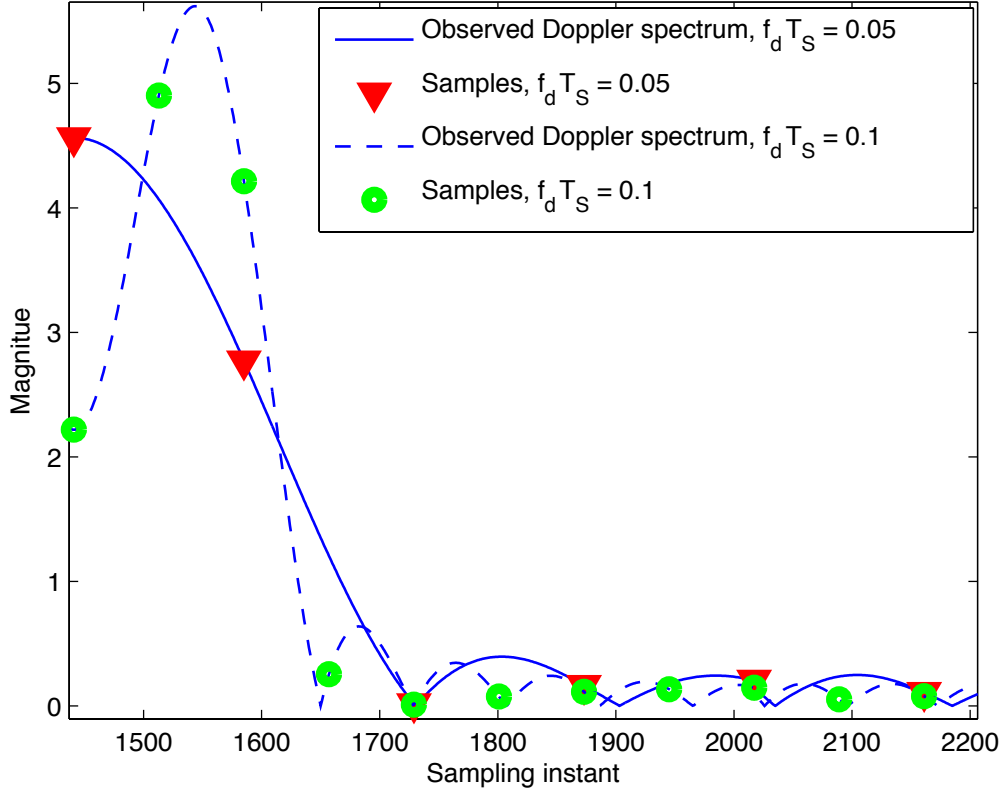


Figure 4.3: The eigenvalues are obtained by sampling the convolution of the Doppler spectrum and the sinc function in frequency domain which can be recognized as the observed Doppler spectrum. The curves show the effect of different window lengths.

4.2.4 Simulation Results and Discussions

Back to doubly selective fading channels, Fig. 4.4 shows the BER performance of a BICM-OFDM system under time-varying channels with two equal-gain paths ($L = 2$). The experiments are conducted with three Doppler spectra and different normalized Doppler frequencies. The system uses 8-PSK modulation, the DFT size is 64, $P = 10$, and a rate-1/2 convolutional code with the generator polynomial [133; 171] ($d_{\text{free}} = 10$)

is adopted such that the system performance is not limited by d_{free} . 10^5 channel realizations are simulated. Fig. 4.4 verifies our predictions on the diversity orders and the effectiveness of the BICM-OFDM systems. For example, consider the case of Jakes' model with $f_d T_S = 0.1$, the 6 largest eigenvalues of time ACF are 3.96, 3.44, 2.23, 0.349, 0.0162 and 0.0004. The first 3 eigenvalues contains 99.67 % of total channel power. As can be expected, the practical diversity order is limited by $r_T \times L = 3 \times 2 = 6$. When $f_d T_S$ is 0.05, the practical diversity order is further reduced to $r_T \times L = 2 \times 2 = 4$ since the number of significant eigenvalues of Φ_T is cut to 2. The results confirm that larger channel variations lead to higher diversity orders. The case of carrier frequency offset (CFO) is also shown to demonstrate channel variation introduced that does not contribute to diversity. The ACF of this case has $[\Phi_T]_{k,1:P} = [e^{j2\pi(1-k)f_d T_S}, e^{j2\pi(2-k)f_d T_S}, \dots, e^{j2\pi(P-k)f_d T_S}]$ at the k -th row. Alternatively, Φ_T can be rewritten as $([1, e^{-j2\pi f_d T_S}, \dots, e^{-j2\pi(P-1)f_d T_S}]^T \otimes [1, e^{j2\pi f_d T_S}, \dots, e^{j2\pi(P-1)f_d T_S}])$ that results in a rank-one matrix and no time diversity gain is available.

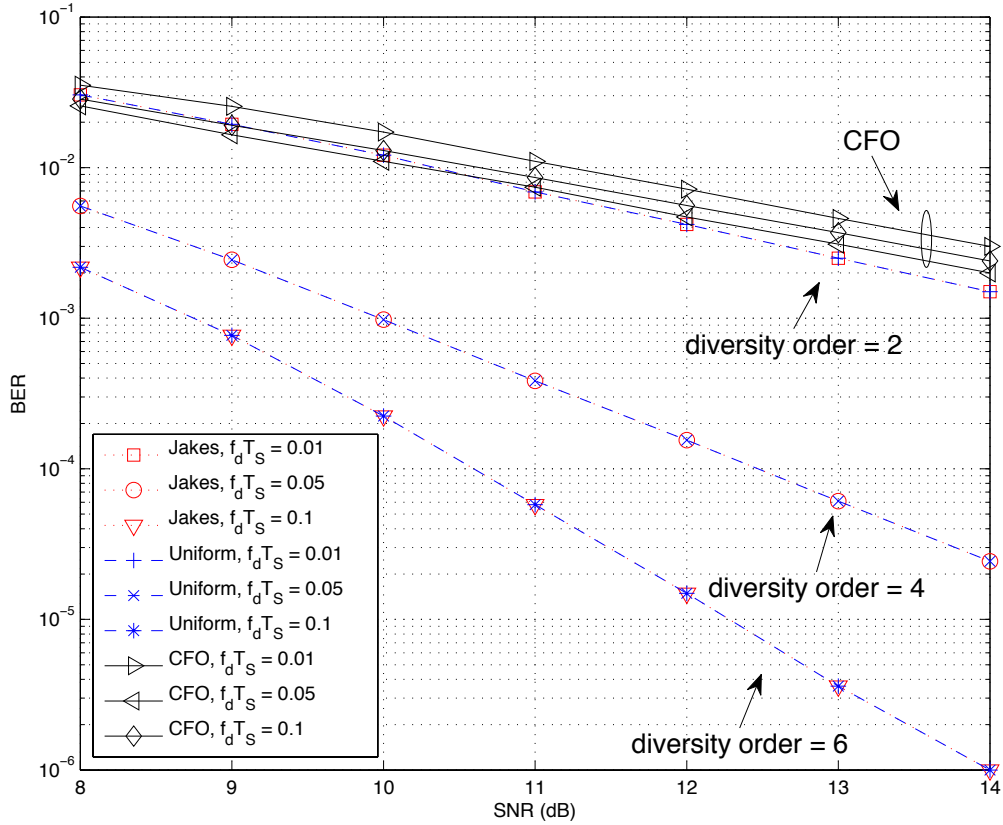


Figure 4.4: Comparison of the diversity gain provided by time-varying channels with three kinds of Doppler power spectral density (PSD): Jakes' model, uniform PSD and carrier frequency offset (CFO). The normalized Doppler frequencies 0.01, 0.05 and 0.1 are simulated. The path gains $h_p(k; l)$ for different l are assumed independent. The time-variation of the channel $E[h_p(k; l)h_p^*(m; l')]$ is $J_0(2\pi f_d(k - m)T) \cdot \delta(l - l')$ for Jakes' model, $\sin(2\pi f_d(k - m)T)/(\pi(k - m)T) \cdot \delta(l - l')$ for uniform PSD and $\exp(j2\pi f_d(k - m)T) \cdot \delta(l - l')$ for CFO, where f_d is the maximum Doppler frequency, T is the OFDM sampling time, $J_0(\cdot)$ is the zeroth order Bessel function of the first kind, and $\delta(\cdot)$ is the Kronecker delta function. Notice that the considered diversity here is the effective diversity order based on the dominant eigenvalues.

Note that in doing the above simulations, relatively simple channel estimation is required in the sense that only the time-averaged channel within each OFDM symbol

needs to be estimated for the receiver to function. The study of channel estimation of OFDM over doubly selective channels has been very active and many efficient methods are available [11,13,66]. Subsequently, efficient ICI cancellation can be done with many methods found in, for example, [1,13,15].

4.3 Extension to the Multiple-Input Multiple-Output Case

The transmission scheme can be extended to MIMO scenarios to benefit from additional gain from spatial diversity. As has been shown, BICM-OFDM can effectively capture time and frequency diversity; to further take advantage of spatial diversity in MIMO situations, a common way is to transform the spatial diversity to time or frequency diversity [30]. In the following we consider two techniques that achieve this goal with little modifications and overhead cost with respect to BICM-OFDM design for SISO cases. We choose a different approach from the obvious choice of combining BICM-OFDM with space time coding (STC), which potentially gives a even larger diversity order of $N_T \times \min\{L, d_{\text{free}}\}$ [27], out of the considerations that the simple receivers often used for Alamouti-like schemes suffer greatly in double selective fading environments and the ML decoders for general STC usually carry prohibitively high cost [76–78].

4.3.1 Cyclic Delay Diversity

The first example is the CDD method used in OFDM systems [79] to transform spatial diversity to multipath diversity (or recognized as frequency diversity); it is done by inserting different cyclic delays to the signal at each transmit antenna. The diver-

sity order is analyzed via the framework established in Section 4.2.2; in essence, the asymptotic diversity order is determined by the rank of \mathbf{R}_{eq} . For simplicity, the case of two transmit antennas and one receive antenna is considered and the results can be extended to more general cases. Starting from the SISO signal model of (2), inserting an intentional delay Δ is equivalent to multiply a circular shift matrix $\mathbf{P} = \begin{bmatrix} \mathbf{0} & \mathbf{I}_\Delta \\ \mathbf{I}_{N-\Delta} & \mathbf{0} \end{bmatrix}$ to the transmit signal $\mathbf{F}^H \mathbf{x}_p$. The receive signal will be $\mathbf{F} \mathbf{H}_p \mathbf{P} \mathbf{F}^H \mathbf{x}_p$ and we can combine \mathbf{P} and \mathbf{H}_p into an equivalent channel. Without loss of generality, assume that an intentional delay Δ is inserted at the second antenna and (4.6) is modified for the MIMO case:

$$\mathbf{y} = \mathbf{X}(\mathbf{I}_P \otimes \mathbf{F}_{N \times 2L'}) \underbrace{(\mathbf{h}_1 + \mathbf{h}_2)}_{\mathbf{h}} + \mathbf{z} = \mathbf{X} \mathbf{h}_{eq} + \mathbf{z} \quad (4.15)$$

where $L' = L + \Delta$ and \mathbf{h}_1 and \mathbf{h}_2 are respectively assembled by

$$\begin{aligned} \mathbf{h}_1 &= [\tilde{h}_1^1(0), \dots, \tilde{h}_1^1(L-1), \mathbf{0}_{1 \times \Delta}, \tilde{h}_2^1(0), \dots, \tilde{h}_2^1(L-1), \\ &\quad \mathbf{0}_{1 \times \Delta}, \dots, \tilde{h}_P^1(0), \dots, \tilde{h}_P^1(L-1), \mathbf{0}_{1 \times \Delta}]_{PL' \times 1}^T \\ \mathbf{h}_2 &= [\mathbf{0}_{1 \times \Delta}, \tilde{h}_1^2(0), \dots, \tilde{h}_1^2(L-1), \mathbf{0}_{1 \times \Delta}, \tilde{h}_2^2(0), \dots, \\ &\quad \tilde{h}_2^2(L-1), \dots, \mathbf{0}_{1 \times \Delta}, \tilde{h}_P^2(0), \dots, \tilde{h}_P^2(L-1)]_{PL' \times 1}^T \end{aligned} \quad (4.16)$$

where superscript is used to denote the transmit antenna index.

Assume that the time and path ACF of \mathbf{h}_1 and \mathbf{h}_2 satisfy the Kronecker model in (9) individually and denote the spatial correlation matrix between two transmit antennas as $\Phi_S = \begin{bmatrix} 1 & \rho_{12} \\ \rho_{21} & 1 \end{bmatrix}$. Further assume that $L \leq \Delta \leq N_{cp} - L$ where N_{cp} is CP length, then the taps of \mathbf{h}_1 and \mathbf{h}_2 will not overlap in the \mathbf{h} in (15), and the length of \mathbf{h} of each OFDM symbol is still within N_{cp} . As a result, the autocorrelation matrix of \mathbf{h} will satisfy the MIMO Kronecker model:

$$\mathbf{R} = \mathbb{E}[\mathbf{h} \mathbf{h}^H] = \Phi_T \otimes \Phi_S \otimes \Phi_L, \quad (4.17)$$

and thus

$$\text{rank}(\mathbf{R}_{eq}) = r_T \times N_T \times L. \quad (4.18)$$

Following the approach in Section 4.2.2, it is straightforward to see from (4.18) that the maximum achievable diversity order is $\min\{r_T \times N_T \times L, d_{\text{free}}\}$. Fig. 4.5 shows the BER performance of an MIMO BICM-OFDM system employing CDD with the normalized Doppler frequency set to 0.05 (thus r_T is 2). The slopes coincide with the analysis results, and the diversity order increases with the path and antenna counts.

4.3.2 Phase-roll Diversity

The second example is to generalize the phase-roll scheme [30], in which the correlation function of the equivalent channel $h[k] = h_1 + h_2 e^{j2\pi k\theta}$ has zeros at certain delays, i.e., $R_k[\Delta k] = \frac{1}{2} \text{E}\{h[k]h^*[k + \Delta k]\} = \frac{1}{2}(1 + e^{j2\pi\Delta k\theta}) = 0$ at $\Delta k\theta = \frac{1}{2}, \frac{3}{2}, \frac{5}{2}, \dots$. Zero correlation, as demonstrated in Section 4.2.2, in turn implies independent channel conditions and opportunities to exploit diversity. One interesting scenario happens when multiple CFOs exist among collaborating transmitters in cooperative communications. The scenario can be fitted into a PRD model with unintentional phase differences induced by CFOs. We have reported simulation results of similar schemes in [31] in which the effectiveness of PRD is clearly demonstrated.

Similarly as in the CDD case, by combining the phase rotation matrix $\mathbf{E} = \text{diag}(1, e^{j\frac{2\pi\varepsilon}{N}}, \dots, e^{j\frac{2\pi\varepsilon(N-1)}{N}})$ and \mathbf{H}_p into an equivalent channel, (4.6) can be rewritten as (when there are two transmit antennas)

$$\mathbf{y} = \mathbf{X}(\mathbf{I}_P \otimes \mathbf{F}_{N \times L})(\mathbf{E}_1 \mathbf{h}_1 + \mathbf{E}_2 \mathbf{h}_2) + \mathbf{z} = \mathbf{X} \mathbf{h}_{eq} + \mathbf{z} \quad (4.19)$$

where $\mathbf{E}_\alpha = \text{diag}([1, 1, \dots, 1] \otimes [e^{j\frac{2\pi\varepsilon_\alpha(N-1)}{N}}, e^{j\frac{2\pi\varepsilon_\alpha 2(N-1)}{N}}, \dots, e^{j\frac{2\pi\varepsilon_\alpha P(N-1)}{N}}])$, $\alpha \in \{1, 2\}$,

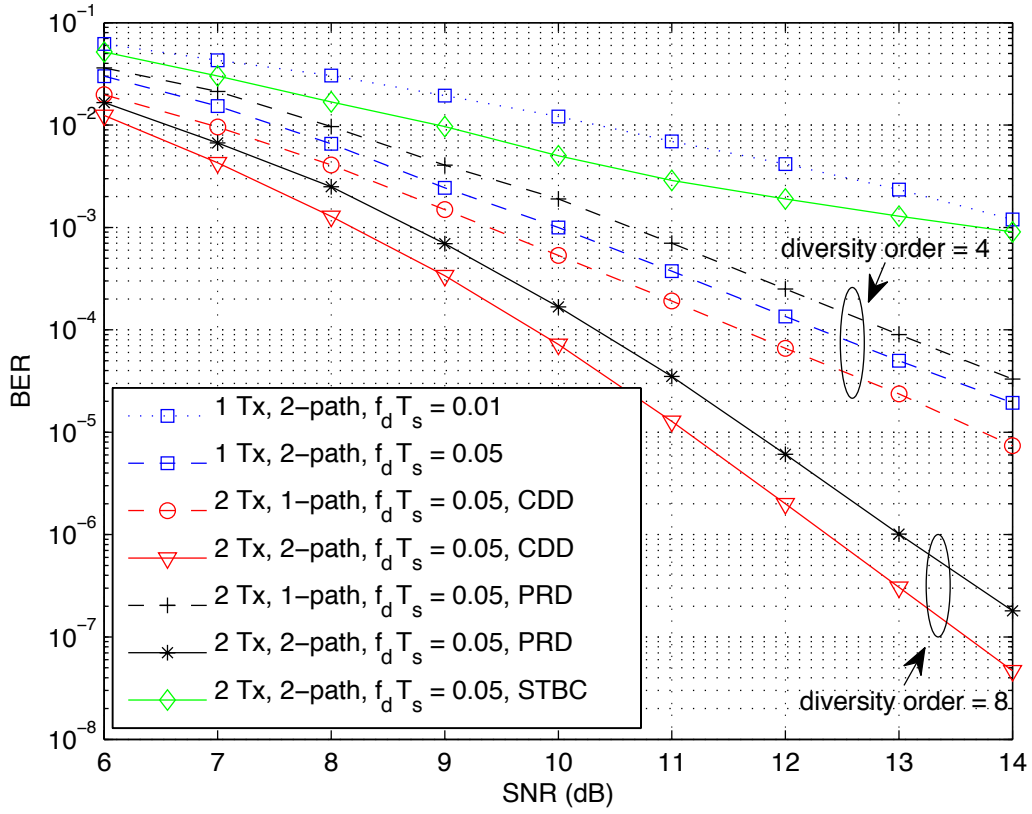


Figure 4.5: BER comparison of the MIMO-BICM-OFDM employing CDD, PRD and STBC over doubly-selective fading channels. The DFT size is 64, $P = 10$, and a rate-1/2 convolutional code with the generator polynomial [133; 171] ($d_{\text{free}} = 10$) is adopted. Notice that the considered diversity here is the effective diversity order based on the dominant eigenvalues. The channel is equal-gain two-path at $l = 0$ and $l = 1$ and the introduced cyclic delay Δ is 5. The parameters of PRD are chosen as $\varepsilon_1 = 0.05$ and $\varepsilon_2 = -0.05$.

is an $PL \times PL$ diagonal matrix representing phase offsets, and \mathbf{h}_α is defined as

$$\mathbf{h}_\alpha = [\tilde{h}_1^\alpha(0), \dots, \tilde{h}_1^\alpha(L-1), \tilde{h}_2^\alpha(0), \dots, \tilde{h}_2^\alpha(L-1), \dots, \tilde{h}_P^\alpha(0), \dots, \tilde{h}_P^\alpha(L-1)]_{PL \times 1}^T. \quad (4.20)$$

Assume that we correct the phase offset from the first transmit antenna and thus, \mathbf{E}_1

becomes an identity matrix. The rank of \mathbf{R}_{eq} can be bounded by [75, Fact 2.10.7]

$$\begin{aligned} \text{rank}(\mathbf{R}_{eq}) &= \text{rank}(\mathbf{R} + \mathbf{E}_2 \mathbf{R} \mathbf{E}_2^H) \\ &\leq \text{rank}(\mathbf{R}) + \text{rank}(\mathbf{E}_2 \mathbf{R} \mathbf{E}_2^H) = r_T \times L \times 2. \end{aligned} \quad (4.21)$$

The last equation follows that $\text{rank}(\mathbf{R}) = \text{rank}(\mathbf{E}_2 \mathbf{R} \mathbf{E}_2^H) = r_T \times L$. The maximum diversity order is increased by N_T due to space diversity, if d_{free} is not the limiting factor. Though the analysis does not find the condition when the bound can be achieved, simulation results, such as those shown in Fig. 5, indicate that it is achievable.

For slow fading channels, it is worth noting that in [70] the diversity gain provided by multiple transmit antennas appears in the same form as our result. It is of no surprise since both methods transform spatial diversity into other types of diversity for easier harvest. Finally, the simulation results show the weakness of Alamouti scheme over doubly selective fading channels. Consider the example of space time Alamouti code where the signal matrix \mathbf{X} in (4.6) becomes $\text{diag}(\mathbf{X}_1^{ST}, \dots, \mathbf{X}_{P/2}^{ST})$ where $\mathbf{X}_p^{ST} = \begin{bmatrix} \mathbf{X}_{2(p-1)+1} & \mathbf{X}_{2(p-1)+2} \\ -\mathbf{X}_{2(p-1)+2}^H & \mathbf{X}_{2(p-1)+1}^H \end{bmatrix}$ with $\mathbf{X}_p = \text{diag}(X((p-1)N), X((p-1)N+1), \dots, X((p-1)N+N-1))$. One would expect the diversity order to be $P \times \min\{L, d_{\text{free}}\}$; however, the performance degrades severely and an error floor occurs if a typical Alamouti receiver is deployed. The degradation is caused by channel variations within an Alamouti codeword and the induced destruction of the Alamouti structure.

Chapter 5 Conclusion and Future Work

The dissertation investigates issues of dealing with ICI in OFDM systems over doubly-selective fading channels. For the ICI cancellation, we proposed an indicator of ICI level on individual subcarrier. Its distribution is shown to be insensitive to the channel PDP and therefore it works properly for a wide range of channels. A PSA framework is proposed to adapt ICI cancellation strategies according to the ICI indicator for each subcarrier and enable a better tradeoff between computational complexity and system performance. PB ZF and MMSE ICI equalizers with very low complexity are developed within the PSA processing framework incorporating an ICI indicator and are very effective at dealing with mild ICI situations. A lookup table method is also developed that forms, together with these equalizers, a comprehensive ICI solution for OFDMA downlink receivers. Theoretical analysis and simulations are provided to show the effectiveness of our approach. About 80% reduction in complexity without sacrificing performance is achieved. We derive the PDF of the ICI indicator to reveal why it can effectively facilitate the PSA framework for low-complexity ICI cancellation schemes and offer valuable information on channel variations.

For exploiting the benefits from time variations, the diversity gains of BICM-OFDM over doubly selective fading channels are examined for both the asymptotic condition of very high SNR and the realistic situation with moderate SNRs. It is shown by simulation that the later diversity order is practically governed by dominant eigenvalues of the channel ACF. The same analysis framework is extended to show that BICM-OFDM together with MIMO techniques can provide even higher diversity gains in, for instance, asynchronous cooperative communications. The results provide insights on the design/tradeoff of design parameters of BICM-OFDM systems, e.g., the

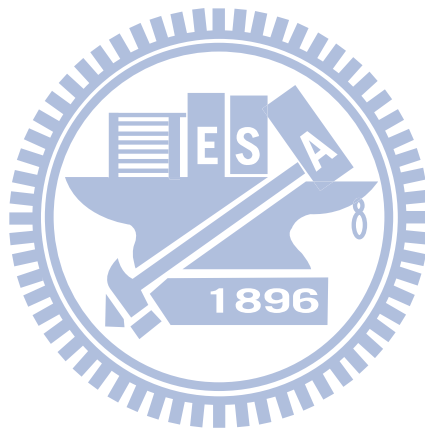
achievable time diversity order versus the length of blocks.

5.1 Future Work

1. Since the ICI indicator can identify whether the subcarrier experiences good or bad channel, to utilize it in the transmitter side to enhance the overall system performance such as adaptive loading or allocation is a potential future research topic. Furthermore, our ICI indicator originally derived from the time linearly varying model that holds only when the normalized Doppler frequency is lower than 0.2. For even faster changing channels, the model that considers higher order terms is necessary. It is worth further investigation on the questions that how to modify the ICI indicator and extend its usability for this scenario.
2. For OFDMA, we set the un-used sub-channels nearing the boundaries to zero. In PSA, we also have the flexibility to choose different ordering for cancellation. Further investigations are needed for these two issues, i.e., consider the co-channel interference from the un-used sub-channels and optimal ordering for ICI cancellation in PSA.
3. Nonlinear ICI cancellation approaches such as MAP or turbo ICI equalizers are still too complex even with the help of ICI indicator and thus further explorations are needed. MIMO ICI equalization is another important topic. In spatial multiplexing, our proposed ICI indicator and equalizers can be easily extended. However, when space-time or space-frequency codes are applied, it is not so trivial.
4. The inter-channel variations have been exploited to gain the diversity in this dissertation. The intra-channel variation may also be used to further improve

the diversity. An initial step on this has been provided in Appendix II. It is interesting to further investigate the diversity order.

5. In the current work, we did not consider the ICI caused by CFO which will result in performance degrades if CFO is left untreated or residual CFO exists; however, other ICI cancellation approaches focused on the Doppler spread induced ICI like us will also have performance degradation. It is worthwhile to study in the future the two kinds of ICIs jointly for practical applications.



Appendix I: Asymptotic Analysis on the Diversity Order of BICM-OFDM in Doubly Selective Channels

With the system model described in Chapter 4, the stacked received signal $\mathbf{y} = [\mathbf{y}_1^T, \mathbf{y}_2^T, \dots, \mathbf{y}_P^T]^T$ can be given as

$$\mathbf{y} = \mathbf{X}(\mathbf{I}_P \otimes \mathbf{F}_{N \times L})\mathbf{h} + \mathbf{z} \triangleq \mathbf{X}\mathbf{h}_{eq} + \mathbf{z} \quad (\text{I.1})$$

where \mathbf{I}_P is a $P \times P$ identity matrix, \otimes denotes the Kronecker product, \mathbf{h} is an length- PL vector defined as

$$\mathbf{h} = [\tilde{h}(1;0), \dots, \tilde{h}(1;L-1), \tilde{h}(2;0), \dots, \tilde{h}(2;L-1), \dots, \tilde{h}(P,0), \dots, \tilde{h}(P,L-1)]^T \quad (\text{I.2})$$

with $\tilde{h}(i;l)$ ($1 \leq i \leq P$, $0 \leq l \leq L-1$) representing the *average* channel impulse response in the i -th OFDM symbol, \mathbf{X} is an $PN \times PN$ diagonal matrix given by

$$\mathbf{X} = \text{diag}(X(0), \dots, X(N-1), X(N), \dots, X(2N-1), \dots, X(PN-1)), \quad (\text{I.3})$$

and \mathbf{z} is an $PN \times 1$ noise vector representing the residual ICI plus noise.

We derive the asymptotic diversity order of BICM-OFDM by first bounding the PEP. Let \mathbf{X} be the coded transmit signal corresponding to codeword \mathbf{c} and $\hat{\mathbf{X}}$ be the detected signal corresponding to codeword $\hat{\mathbf{c}}$ where $\mathbf{c} \neq \hat{\mathbf{c}}$. The assumption that the interleaver maps consecutive coded bits to different constellation points and transmitted onto different OFDM subcarriers is adopted [27]. Assume that \mathbf{z} is complex Gaussian distributed with zero mean and variance N_0 . The maximum-likelihood decision rule is to choose the error signal $\hat{\mathbf{X}}$ if

$$\frac{1}{(\pi N_0)^{PN/2}} \exp\left(-\frac{\|\mathbf{y} - \hat{\mathbf{X}}\mathbf{h}_{eq}\|^2}{N_0}\right) \geq \frac{1}{(\pi N_0)^{PN/2}} \exp\left(-\frac{\|\mathbf{y} - \mathbf{X}\mathbf{h}_{eq}\|^2}{N_0}\right). \quad (\text{I.4})$$

So, the conditional error probability $P(\mathbf{c} \rightarrow \hat{\mathbf{c}}|\mathbf{h})$ is equivalent to

$$\begin{aligned}
& P(\|\mathbf{z}\|^2 \geq \|\mathbf{z} + (\mathbf{X} - \hat{\mathbf{X}})\mathbf{h}_{eq}\|^2|\mathbf{h}) \\
&= P\{\mathbf{z}^H \mathbf{z} > \mathbf{z}^H \mathbf{z} - \mathbf{z}^H (\mathbf{X} - \hat{\mathbf{X}})\mathbf{h}_{eq} - \mathbf{h}_{eq}^H (\mathbf{X} - \hat{\mathbf{X}})^H \mathbf{z} + \mathbf{h}_{eq}^H (\mathbf{X} - \hat{\mathbf{X}})^H (\mathbf{X} - \hat{\mathbf{X}})\mathbf{h}_{eq}|\mathbf{h}\} \\
&= P(T \geq \|(\mathbf{X} - \hat{\mathbf{X}})\mathbf{h}_{eq}\|^2|\mathbf{h})
\end{aligned} \tag{I.5}$$

where $T = \mathbf{z}^H (\mathbf{X} - \hat{\mathbf{X}})\mathbf{h}_{eq} + \mathbf{h}_{eq}^H (\mathbf{X} - \hat{\mathbf{X}})^H \mathbf{z}$ is a zero-mean complex Gaussian random variable (RV) with variance $2N_0\|(\mathbf{X} - \hat{\mathbf{X}})\mathbf{h}_{eq}\|^2$.

By using the Q -function, the error probability in (I.5) can be written as

$$Q\left(\frac{\|(\mathbf{X} - \hat{\mathbf{X}})\mathbf{h}_{eq}\|^2}{\sqrt{2N_0\|(\mathbf{X} - \hat{\mathbf{X}})\mathbf{h}_{eq}\|^2}}\right) = Q\left(\sqrt{\frac{1}{2N_0}}\|(\mathbf{X} - \hat{\mathbf{X}})\mathbf{h}_{eq}\|\right) \tag{I.6}$$

where

$$Q(x) = \frac{1}{\sqrt{2\pi}} \int_x^\infty e^{-\frac{y^2}{2}} dy. \tag{I.7}$$

Then, the pairwise error probability (PEP) can be derived by averaging over all channel realization

$$\begin{aligned}
P(\mathbf{c} \rightarrow \hat{\mathbf{c}}) &= \mathbb{E} \left[Q\left(\sqrt{\frac{1}{2N_0}}\|(\mathbf{X} - \hat{\mathbf{X}})\mathbf{h}_{eq}\|\right) \right] \\
&= \mathbb{E} \left[Q\left(\sqrt{\frac{\text{SNR} \cdot \mathbf{h}_{eq}^H \mathbf{D}^H \mathbf{D} \mathbf{h}_{eq}}{2}}\right) \right] \\
&= \mathbb{E} \left[Q\left(\sqrt{\frac{\text{SNR} \cdot \mathbf{h}^H (\mathbf{I}_P \otimes \mathbf{F}_{N \times L})^H \mathbf{D}^H \mathbf{D} (\mathbf{I}_P \otimes \mathbf{F}_{N \times L}) \mathbf{h}}{2}}\right) \right]
\end{aligned} \tag{I.8}$$

where $\text{SNR} = 1/N_0$ since the average power of channel and transmitted signal are normalized to one and $\mathbf{D} = \mathbf{X} - \hat{\mathbf{X}}$ is the coded symbol difference matrix. According to the assumption made in the interleaver, there are at least d_{free} non-zero terms in \mathbf{D} [27]. In the following we consider the worst case that there are only d_{free} different terms between \mathbf{X} and $\hat{\mathbf{X}}$ and each of these terms has Euclidean distance d_{min}^2 . Note that the typical parameters of BICM-OFDM are chosen as $N \geq L$ and $N \geq d_{\text{free}}$.

A typical PEP analysis such as that in [27] assumes that the vector \mathbf{h}_{eq} has independent elements and the rank analysis is focused on the term $\mathbf{D}^H \mathbf{D}$. Here, however, the correlation of channels over several OFDM symbols needs to be considered. We adopt the approach in [29] to extract the statistical independent components in \mathbf{h}_{eq} which are considered as the source of diversity. After the extraction the usual PEP analysis can proceed.

Assume the Kronecker model [30,70,71] for the channel, i.e., the autocorrelation matrix of the channel can be decoupled as

$$\mathbf{R} = \mathbb{E}[\mathbf{h}\mathbf{h}^H] = \Phi_T \otimes \Phi_L, \quad (\text{I.9})$$

where Φ_T and Φ_L are the time and path gains autocorrelation matrices. The rank of the channel autocorrelation matrix is [75, Fact 7.4.20]:

$$\text{rank}(\mathbf{R}) = \text{rank}(\Phi_T \otimes \Phi_L) = \text{rank}(\Phi_T) \times \text{rank}(\Phi_L) = r_T \times L \quad (\text{I.10})$$

where r_T and L are the ranks of Φ_T and Φ_L , respectively. Note that $r_T \times L$ is bounded by $P \times L$. The correlation matrix of \mathbf{H}_{eq} is $\mathbf{R}_{eq} = \mathbb{E}[\mathbf{h}_{eq}\mathbf{h}_{eq}^H] = (\mathbf{I}_P \otimes \mathbf{F}_{N \times L}) \mathbb{E}[\mathbf{h}\mathbf{h}^H] (\mathbf{I}_P \otimes \mathbf{F}_{N \times L})^H = (\mathbf{I}_P \otimes \mathbf{F}_{N \times L}) \mathbf{R} (\mathbf{I}_P \otimes \mathbf{F}_{N \times L})^H$. Since $\mathbf{F}_{N \times L}$ has full rank L , the matrix $(\mathbf{I}_P \otimes \mathbf{F}_{N \times L})$ also has full rank PL .

We use the following proposition [75, Proposition 2.6.2]: let \mathbf{A} be a $m \times n$ matrix, \mathbf{B} is $n \times k$ with rank n , and \mathbf{C} is $l \times m$ with rank m , then $\text{rank}(\mathbf{AB}) = \text{rank}(\mathbf{A})$ and $\text{rank}(\mathbf{CA}) = \text{rank}(\mathbf{A})$. Therefore, the rank of \mathbf{R}_{eq} is

$$\text{rank}(\mathbf{R}_{eq}) = \text{rank}(\mathbf{R}) = r_T \times L. \quad (\text{I.11})$$

The eigenvalue decomposition is used to extract the statistically independent components in \mathbf{h}_{eq} . Consider $\mathbf{R}_{eq} = \mathbf{V} \Sigma_h \mathbf{V}^H$ where \mathbf{V} is a $PN \times r_T L$ matrix satisfying

$\mathbf{V}^H \mathbf{V} = \mathbf{I}_{r_T L}$ and $\boldsymbol{\Sigma}_h = \text{diag}(\sigma_1^2, \dots, \sigma_{r_T L}^2)$. In the following analysis, \mathbf{h}_{eq} is substituted by $\mathbf{V} \boldsymbol{\Sigma}_h^{\frac{1}{2}} \bar{\mathbf{h}}_{eq}$ where $\bar{\mathbf{h}}_{eq}$ is the $r_T L \times 1$ normalized equivalent channel vector containing independent and identically distributed (iid) zero-mean complex Gaussian random variables with unit variance. It can be shown that the PEP is not affected by this substitution, since \mathbf{h}_{eq} and $\mathbf{V} \boldsymbol{\Sigma}_h^{\frac{1}{2}} \bar{\mathbf{h}}_{eq}$ have identical distributions which is known as the isotropy property of the standard Gaussian random vector.

The term $\mathbf{h}_{eq}^H \mathbf{D}^H \mathbf{D} \mathbf{h}_{eq}$ in (I.8) now becomes $\bar{\mathbf{h}}_{eq}^H (\boldsymbol{\Sigma}_h^{\frac{1}{2}})^H \mathbf{V}^H \mathbf{D}^H \mathbf{D} \mathbf{V} \boldsymbol{\Sigma}_h^{\frac{1}{2}} \bar{\mathbf{h}}_{eq}$. Note that the central part $(\boldsymbol{\Sigma}_h^{\frac{1}{2}})^H \mathbf{V}^H \mathbf{D}^H \mathbf{D} \mathbf{V} \boldsymbol{\Sigma}_h^{\frac{1}{2}}$ is a Hermitian matrix and can be diagonalized by an unitary matrix \mathbf{U} , i.e., $(\boldsymbol{\Sigma}_h^{\frac{1}{2}})^H \mathbf{V}^H \mathbf{D}^H \mathbf{D} \mathbf{V} \boldsymbol{\Sigma}_h^{\frac{1}{2}} = \mathbf{U} \boldsymbol{\Lambda} \mathbf{U}^H$ where $\boldsymbol{\Lambda} = \text{diag}\{\lambda_1, \dots, \lambda_{r_{TV}}\}$ contains the eigenvalues. Since $\mathbf{V} \boldsymbol{\Sigma}_h^{\frac{1}{2}}$ has rank $r_T L$ and the diagonal matrix $\mathbf{D}^H \mathbf{D}$ has rank d_{free} , it follows immediately that the rank of $(\boldsymbol{\Sigma}_h^{\frac{1}{2}})^H \mathbf{V}^H \mathbf{D}^H \mathbf{D} \mathbf{V} \boldsymbol{\Sigma}_h^{\frac{1}{2}}$ is $\min(r_T L, d_{\text{free}})$, and hereafter it is denoted as r_{TV} .

Moreover, define $\check{\mathbf{h}} = \mathbf{U}^H \bar{\mathbf{h}}_{eq}$ and notice that $\check{\mathbf{h}}$ is iid complex Gaussian distributed with zero mean and unit variance since \mathbf{U} is unitary. Thus, (I.8) becomes

$$P(\mathbf{c} \rightarrow \hat{\mathbf{c}}) = \mathbb{E} \left[Q \left(\sqrt{\frac{\text{SNR} \cdot \check{\mathbf{h}}^H \boldsymbol{\Lambda} \check{\mathbf{h}}}{2}} \right) \right] = \mathbb{E} \left[Q \left(\sqrt{\frac{\text{SNR} \cdot d_{\min}^2}{2} \sum_{n=1}^{r_{TV}} \lambda_n |\check{h}_n|^2} \right) \right] \quad (\text{I.12})$$

where \check{h}_n is the n -th element in $\check{\mathbf{h}}$ and its magnitude $|\check{h}_n|$ is Rayleigh distributed with the PDF

$$f(x) = 2x \exp(-x^2), \quad x \geq 0. \quad (\text{I.13})$$

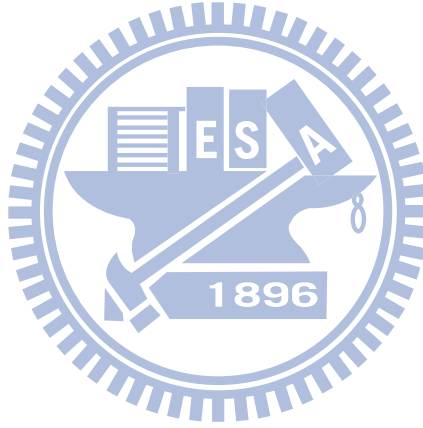
We use the upper bound on the Q-function, $Q(x) \leq e^{-\frac{x^2}{2}}$, and (I.12) can be upper bounded as

$$P(\mathbf{c} \rightarrow \hat{\mathbf{c}}) \leq \mathbb{E} \left[\exp \left(-\frac{\text{SNR} \cdot d_{\min}^2}{4} \sum_{n=1}^{r_{TV}} \lambda_n |\check{h}_n|^2 \right) \right]. \quad (\text{I.14})$$

Then using the PDF in (I.13), the RHS in (I.14) can be derived as

$$\begin{aligned}
& \mathbb{E}[\exp(-\frac{\text{SNR} \cdot d_{\min}^2}{4} \sum_{n=1}^{r_{TV}} \lambda_n |\check{H}_n|^2)] \\
&= \int \cdots \int 2|\check{h}_1| \times \cdots \times 2|\check{h}_{r_{TV}}| \cdot \exp(-\frac{\text{SNR} \cdot d_{\min}^2}{4} \sum_{n=1}^{r_{TV}} \lambda_n |\check{h}_n|^2) \times \\
& \exp(-|\check{h}_1|^2) \times \cdots \times \exp(-|\check{h}_{r_{TV}}|^2) d|\check{h}_1| \cdots d|\check{h}_{r_{TV}}| \\
&= \frac{1}{\prod_{n=1}^{r_{TV}} [1 + (\lambda_n \text{SNR} \cdot d_{\min}^2 / 4)]}.
\end{aligned} \tag{I.15}$$

Finally, when SNR is large enough and the eigenvalue is non-zero, the term 1 in the denominator in (I.15) can be neglected. Thus, Equation (4.14) in Chapter 4 can be obtained.



Appendix II: Regarding the Diversity Order From Intra-Symbol Channel Variations

We investigate the impact of ICI on the diversity order here. We have shown that available ICI-cancellation techniques are good enough for the system to realize the potential diversity order resulting from the *inter-symbol* channel variation. As regarding the benefit of exploiting the *intra-symbol* channel variation, it has been observed that the diversity order slightly increases if ICI is utilized at the receiver [9,11,12,18] but the high complexity remains a concern. However, more delicate effects of ICI on the diversity order still need further investigation. We chose not to distract ourselves in Chapter 4 with this venture. Here we show how one may further pursuit this direction of analysis by making additional assumptions. With these assumptions, our framework can be extended to evaluate the diversity gain provided by the *intra-symbol* channel variation.

Consider the transmission of a single OFDM symbol and assume that the time variation of CIR is linear within the OFDM symbol [13,15]. It is a reasonable assumption in most practical cases when the normalized Doppler frequency is smaller than 0.1, which corresponds to 500 km/h in WiMAX standard. The CIR can be written as

$$h(pN_S - N + t; l) = h(pN_S - \frac{N-1}{2}; l) + \frac{t - \frac{N-1}{2}}{N_S} \delta(pN_S; l) \quad (\text{II.1})$$

where N_S denotes the length of CP plus N . $h(pN_S - N + t; l)$ and $h(pN_S - \frac{N-1}{2}; l)$ represent the l -th path at the t -sample instant and the center point of the p -th OFDM symbol, respectively, and $\delta(pN_S; l)$ is the difference of CIR between the $(p-1)$ -th and

the p -th OFDM symbol. Note that with the linear variation assumption the channel at the center point is also the averaged channel in one OFDM symbol.

We shall drop the OFDM symbol index for simplicity for now since we are considering the *intra-symbol* channel variation. The CIR matrix can be decomposed as

$$\mathbf{H}_t = \mathbf{M}_t + \boldsymbol{\xi} \boldsymbol{\Delta}_t \quad (\text{II.2})$$

where $[\mathbf{M}_t]_{i,j} = h(pN_S - \frac{N-1}{2}; i - j)$ and $[\boldsymbol{\Delta}_t]_{i,j} = \delta(pN_S; i - j)$ for $i, j = 0, 1, \dots, N - 1$. \mathbf{M}_t and $\boldsymbol{\Delta}_t$ both are circulant matrices. The diagonal matrix $\boldsymbol{\xi}$ is defined as $\boldsymbol{\xi} = \frac{1}{N_S} \text{diag}(-\frac{N-1}{2}, -\frac{N-1}{2} + 1, \dots, \frac{N-1}{2})$. Note that $h(pN_S - \frac{N-1}{2}; l)$ and $\delta(pN_S; l)$ are assumed to be zero when $l \leq 0$ or $l \geq L - 1$.

The CFR can be derived as

$$\begin{aligned} \mathbf{H}_f &= \mathbf{F} \mathbf{H}_t \mathbf{F}^H \\ &= \mathbf{F} \mathbf{M}_t \mathbf{F}^H + \mathbf{F} \boldsymbol{\xi} \mathbf{F}^H \mathbf{F} \boldsymbol{\Delta}_t \mathbf{F}^H \\ &= \mathbf{H}_f + \boldsymbol{\Xi} \boldsymbol{\Delta}_f \end{aligned} \quad (\text{II.3})$$

The frequency-domain received signal model is

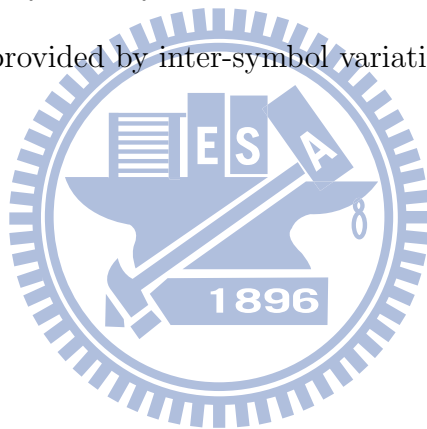
$$\begin{aligned} \mathbf{y} &= \mathbf{H}_f \mathbf{x} + \mathbf{z} \\ &= \mathbf{H}_f \mathbf{x} + \boldsymbol{\Xi} \boldsymbol{\Delta}_f \mathbf{x} + \mathbf{z} \\ &= \mathbf{X} \mathbf{F} \mathbf{h}_t + \boldsymbol{\Xi} \mathbf{X} \mathbf{F} \boldsymbol{\delta}_t + \mathbf{z} \end{aligned} \quad (\text{II.4})$$

where $\mathbf{h}_t = [h(pN_S - \frac{N-1}{2}; 0), h(pN_S - \frac{N-1}{2}; 1), \dots, h(pN_S - \frac{N-1}{2}; L - 1)]^T$ and $\boldsymbol{\delta}_t = [\delta(pN_S; 0), \delta(pN_S; 1), \dots, \delta(pN_S; L - 1)]^T$.

To obtain the signal model used in Chapter 4 (cf. Equation (4.6)), (II.4) is rewritten in matrix form:

$$\begin{aligned} \mathbf{y} &= \begin{bmatrix} \mathbf{X} & \boldsymbol{\Xi} \mathbf{X} \end{bmatrix} \mathbf{F} \begin{bmatrix} \mathbf{h}_t \\ \boldsymbol{\delta}_t \end{bmatrix} + \mathbf{z} \\ &\triangleq \mathbf{X}_{eq} \mathbf{h}_{eq} + \mathbf{z}. \end{aligned} \quad (\text{II.5})$$

The diversity order can be analyzed via the framework established in Chapter 4.2; in essence, the asymptotic diversity order is determined by the rank of \mathbf{R}_{eq} . It can be inferred that the *intra-symbol* channel variation potentially provides higher diversity orders. However, the power of the difference channel $\boldsymbol{\delta}_t$ is usually two-order smaller than that of the average channel \mathbf{h}_t [13]. The diversity gain due to $\boldsymbol{\delta}_t$, unlike the frequency diversity provided by \mathbf{h}_t , is not accessible when SNR is moderate. Moreover, the optimal ML receiver fully exploiting the signal energy from the ICI terms is required while the corresponding super-trellis in the Viterbi algorithm usually demands unaffordable computational resource. Instead of complicating the analysis by studying the marginal gain provided by intra-symbol channel variation, we chose to focus on the more pronounced benefit provided by inter-symbol variation.



References

- [1] D. Huang, K. B. Letaief, and J. Lu, “Bit-interleaved time-frequency coded modulation for OFDM systems over time-varying channels,” *IEEE Trans. Commun.*, vol. 53, no. 7, pp. 1191–1199, Jul. 2005.
- [2] G. Caire, G. Taricco, and E. Biglieri, “Bit-interleaved code modulation,” *IEEE Trans. Inf. Theory*, vol. 44, no. 3, pp. 927–946, May 1998.
- [3] X. Li, A. Chindapol, and J. A. Ritcey, “Bit-interleaved coded modulation with iterative decoding and 8-PSK signaling,” *IEEE Trans. Commun.*, vol. 50, no. 8, pp. 1250–1257, Aug. 2002.
- [4] S. B. Weinstein and P. M. Ebert, “Data transmission by frequency division multiplexing using the discrete fourier transform,” *IEEE Trans. Commun.*, vol. COM-19, pp. 628–634, Oct. 1971.
- [5] L. J. Cimini, “Analysis and simulation of a digital mobile radio channel using orthogonal frequency division multiplexing,” *IEEE Trans. Commun.*, vol. COM-33, pp. 665–675, Jul. 1985.
- [6] J. A. C. Bingham, “Multicarrier modulation for data transmission: An idea whose time has come,” *IEEE Commun. Mag.*, vol. 28, no. 5, pp. 5–14, May 1990.
- [7] *Draft IEEE Standard for Local and Metropolitan Area Networks Part 16: Air Interface for Fixed and Mobile Broadband Wireless Access Systems*, IEEE Draft Std. 802.16e/D7, 2005.
- [8] A. Stamoulis, S. N. Diggavi, and N. Al-Dhahir, “Intercarrier interference in MIMO OFDM,” *IEEE Trans. Signal Process.*, vol. 50, no. 10, pp. 2451–2464, Oct. 2002.
- [9] P. Schniter, “Low-complexity equalization of OFDM in doubly selective channels,” *IEEE Trans. Signal Process.*, vol. 52, no. 4, pp. 1002–1011, Oct. 2004.
- [10] W. G. Jeon, K. H. Chang, and Y. S. Cho, “An equalization technique for orthogonal frequency-division multiplexing systems in time-variant multipath fading channels,” *IEEE Trans. Commun.*, vol. 47, no. 1, pp. 27–32, Jan. 1999.

- [11] Y. S. Choi, P. J. Voltz, and F. A. Cassara, "On channel estimation and detection for multicarrier signals in fast and selective Rayleigh fading channels," *IEEE Trans. Commun.*, vol. 49, no. 8, pp. 1375–1387, Aug. 2001.
- [12] X. Cai and G. B. Giannakis, "Bounding performance and suppressing intercarrier interference in wireless mobile OFDM," *IEEE Trans. Commun.*, vol. 51, no. 12, pp. 2047–2056, Dec. 2003.
- [13] A. Gorokhov and J.-P. Linnartz, "Robust OFDM receivers for dispersive time-varying channels: equalization and channel acquisition," *IEEE Trans. Wireless Commun.*, vol. 52, no. 4, pp. 572–583, Apr. 2004.
- [14] I. Barhumi, G. Leus, and M. Moonen, "Time-domain and frequency-domain per-tone equalization for OFDM over doubly selective channels," *Signal processing*, vol. 84, no. 11, pp. 2055–2066, 2004.
- [15] Y. Mostofi and D. C. Cox, "ICI mitigation for pilot-aided OFDM mobile systems," *IEEE Trans. Wireless Commun.*, vol. 4, no. 2, pp. 765–774, Mar. 2005.
- [16] L. Rugini, P. Banelli, and G. Leus, "Simple equalization of time-varying channels for OFDM," *IEEE Commun. Lett.*, vol. 9, no. 7, pp. 619–621, Jul. 2005.
- [17] S. Das and P. Schniter, "Max-SINR ISI/ICI-shaped multi-carrier communication over the doubly dispersive channel," *IEEE Trans. Signal Process.*, vol. 55, no. 12, pp. 5782–5795, Dec. 2007.
- [18] D. N. Liu and M. P. Fitz, "Iterative MAP equalization and decoding in wireless mobile coded OFDM," *IEEE Trans. Commun.*, vol. 57, no. 7, pp. 2042–2051, Jul. 2009.
- [19] K. Fang, L. Rugini, and G. Leus, "Low-complexity block turbo equalization for OFDM systems in time-varying channels," *IEEE Trans. Signal Process.*, vol. 56, no. 11, pp. 5555–5566, Nov. 2008.
- [20] C.-Y. Hsu and W.-R. Wu, "Low-complexity ICI mitigation methods for high-mobility SISO/MIMO-OFDM systems," *IEEE Trans. Veh. Technol.*, vol. 58, no. 6, pp. 2755–2768, Jul. 2009.

- [21] I. Barhumi and M. Moonen, “MLSE and MAP equalization for transmission over doubly selective channels,” *IEEE Trans. Veh. Technol.*, vol. 58, no. 8, pp. 4120–4128, Oct. 2009.
- [22] T. Hrycak, S. Das, G. Matz, and H. G. Feichtinger, “Low complexity equalization for doubly selective channels modeled by a basis expansion,” *IEEE Trans. Signal Process.*, vol. 58, no. 11, pp. 5706–5719, Nov. 2010.
- [23] E. Panayirci, H. Dogan, and H. V. Poor, “Low-complexity MAP-based successive data detection for coded OFDM systems over highly mobile wireless channels,” *IEEE Trans. Veh. Technol.*, vol. 60, no. 6, pp. 2849–2857, Jul. 2011.
- [24] H. D. Lin, T. H. Sang, and J. T. Chen, “Low-cost perturbation-based ICI equalizers for OFDMA mobile systems,” *IEICE Trans. Commun.*, vol. E95-B, no. 11, pp. 3509–3518, Nov. 2012.
- [25] H. D. Lin and T. H. Sang, “Estimation of channel variation and its applications in OFDM-based systems,” in *the 12th International Conference on ITS Telecommunications*, Nov. 2010.
- [26] E. Zehavi, “8-PSK trellis codes for a Rayleigh channel,” *IEEE Trans. Commun.*, vol. 40, no. 5, pp. 873–884, May 1992.
- [27] E. Akay and E. Ayanoglu, “Achieving full frequency and space diversity in wireless systems via BICM, OFDM, STBC, and Viterbi decoding,” *IEEE Trans. Commun.*, vol. 54, no. 12, pp. 2164–2172, Dec. 2006.
- [28] L. Zhang, C. Zhao, J. Wu, and W. Wang, “MAP based equalizer for OFDM systems in time-varying multipath channels,” in *GLOBECOM '06 IEEE*, Dec. 2006.
- [29] X. Ma and G. Giannakis, “Maximum diversity over doubly selective fading channels,” *IEEE Trans. Inf. Theory*, vol. 49, no. 7, pp. 1832–1840, Jul. 2003.
- [30] A. Paulraj, R. Nabar, and D. Gore, *Introduction to Space-Time Wireless Communications*. Cambridge University Press, 2003.

- [31] H.-D. Lin, T.-H. Sang, and D. W. Lin, “BICM-OFDM for cooperative communications with multiple synchronization errors,” in *Proc. Int. Wirel. Commun. Mobile Comput. Conf.*, Jul. 2010, pp. 1055–1059.
- [32] D. Tse and P. Viswanath, *Fundamentals of Wireless Communication*, 1st ed. Cambridge University Press, 2005.
- [33] J. G. Proakis, *Digital Communications*, 5th ed. NJ: McGraw-Hill, 2007.
- [34] *Wireless LAN Medium Access Control (MAC) and Physical Layer (PHY) specifications: High-speed Physical Layer in the 5 GHz Band*, IEEE Std. 802.11a, 1999.
- [35] W. C. Jakes, *Microwave Mobile Communications*. New York: Wiley, 1974.
- [36] W. Tranter, K. Shanmugan, T. Rappaport, and K. Kosbar, *Simulation of communication systems: modeling, methodology and technique*. Prentice Hall Press, 2003.
- [37] M. C. Jeruchim, P. Balaban, and K. S. Shanmugan, *Simulation of communication systems: modeling, methodology and technique*, 2nd ed. Springer, 2000.
- [38] C. Xiao, Y. R. Zheng, and N. C. Beaulieu, “Second-order statistical properties of the WSS Jakes’ fading channel simulator,” *IEEE Trans. Commun.*, vol. 50, pp. 888–891, Jun. 2002.
- [39] Y. R. Zheng and C. Xiao, “Improved models for the generation of multiple uncorrelated Rayleigh fading waveforms,” *IEEE Commun. Lett.*, vol. 6, pp. 256–258, Jun. 2002.
- [40] —, “Simulation models with correct statistical properties for Rayleigh fading channels,” *IEEE Trans. Commun.*, vol. 51, pp. 920–928, Jun. 2003.
- [41] C.-H. Chen, C.-L. Wang, and C.-T. Chen, “A resource allocation scheme for cooperative multiuser OFDM-based cognitive radio systems,” *IEEE Trans. Commun.*, vol. 59, no. 11, pp. 3204–3215, Nov. 2011.
- [42] B. Rivet, L. Girin, and C. Jutten, “Log-Rayleigh distribution: A simple and efficient statistical representation of Log-Spectral coefficient,” *IEEE Transactions on Audio, Speech & Language Processing*, vol. 15, no. 3, pp. 796–802, Mar. 2007.

- [43] J.-C. Lin, "Least-squares channel estimation for mobile OFDM communication on time-varying frequency-selective fading channels," *IEEE Trans. Veh. Technol.*, vol. 57, no. 6, pp. 3538–3550, Nov. 2008.
- [44] —, "Channel estimation assisted by postfixed pseudo-noise sequences padded with zero samples for mobile orthogonal-frequency-division-multiplexing communications," *IET Commun.*, vol. 3, pp. 561–570, Apr. 2009.
- [45] —, "Least-squares channel estimation assisted by self-interference cancellation for mobile PRP-OFDM applications," *IET Commun.*, vol. 3, pp. 1907–1918, Dec. 2009.
- [46] W.-R. Wu and C.-F. Lee, "A low-complexity channel-estimation method for IEEE 802.16e systems," in *2007 Asia-Pacific Conference on Communications*, Oct. 2007.
- [47] W.-R. Wu, R.-C. Chiueh, and F.-S. Tseng, "Channel estimation for OFDM systems with subspace pursuit algorithm," in *Proc. IEEE ICGCS 2010*, 2010.
- [48] M.-L. Ku and C.-C. Huang, "A refined channel estimation method for STBC/OFDM systems in high-mobility wireless channels," *IEEE Trans. Wireless Commun.*, vol. 7, no. 11, pp. 4312–4320, Nov. 2008.
- [49] H.-Y. Chen, M.-L. Ku, S.-J. Jou, and C.-C. Huang, "A robust channel estimator for high-mobility STBC-OFDM systems," *IEEE Trans. Circuits Syst.*, vol. 7, no. 4, pp. 925–936, Apr. 2010.
- [50] Y.-H. Chung and S.-M. Phoong, "OFDM channel estimation in the presence of transmitter and receiver i/q imbalance," in *European Signal Processing Conference*, Aug. 2008.
- [51] —, "Joint estimation of I/Q imbalance, CFO and channel response for MIMO OFDM systems," *IEEE Trans. Commun.*, vol. 58, no. 5, pp. 1485–1492, May 2010.
- [52] C.-L. Wang and H.-C. Wang, "Optimized joint fine timing synchronization and channel estimation for MIMO systems," *IEEE Trans. Commun.*, vol. 59, no. 4, pp. 1089–1098, Apr. 2011.

- [53] K. E. Baddour and N. C. Beaulieu, "Robust Doppler spread estimation in non-isotropic fading channels," *IEEE Trans. Wireless Commun.*, vol. 4, no. 6, pp. 2677–2682, Nov. 2005.
- [54] C. Tepedelenlioglu and G. Giannakis, "On velocity estimation and correlation properties of narrow-band mobile communication channels," *IEEE Trans. Veh. Technol.*, vol. 50, no. 4, pp. 1039–1052, Jul. 2001.
- [55] J. M. Holtzman and A. Sampath, "Adaptive averaging methodology for handoffs in cellular systems," *IEEE Trans. Veh. Technol.*, vol. 44, no. 1, pp. 59–66, Feb. 1995.
- [56] T. Yucek, R. M. A. Tannious, and H. Arslan, "Doppler spread estimation for wireless ofdm systems," in *IEEE Sarnoff Symposium on Advances in Wired and Wireless Communication*, Apr. 2005, pp. 233–236.
- [57] Y.-S. Choi, O. C. Ozdural, H. P. Liu, and S. Alamouti, "A maximum likelihood Doppler frequency estimator for OFDM system," in *IEEE ICC*, 2006, pp. 4572–4576.
- [58] Y.-R. Tsai, K.-J. Yang, C.-H. Tsai, and C.-L. Wang, "Low-complexity ML doppler spread estimation for OFDM systems," in *Proceedings of the 2011 IEEE Vehicular Technology Conference - Fall (VTC 2011-Fall)*, Sep. 2011.
- [59] C. Tepedelenlioglu, A. Abdi, G. Giannakis, and M. Kaveh, "Estimation of doppler spread and signal strength in mobile communications with applications to handoff and adaptive transmission," *Wireless Communications and Mobile Computing*, vol. 1, pp. 221–242, Mar. 2001.
- [60] M.-L. Ku, W.-C. Chen, and C.-C. Huang, "EM-based iterative receivers for OFDM and BICM/OFDM systems in doubly selective channels," *IEEE Trans. Wireless Commun.*, vol. 10, no. 5, pp. 1405–1415, May 2011.
- [61] H.-W. Wang, D.-W. Lin, and T.-H. Sang, "OFDM signal detection in doubly selective channels with blockwise whitening of residual intercarrier interference and noise," *IEEE J. Sel. Areas Commun.*, vol. 30, no. 4, pp. 684–694, May 2012.

- [62] Y. Zhao and S. G. Haggman, "Intercarrier interference self-cancellation scheme for OFDM mobile communication systems," *IEEE Trans. Commun.*, vol. 49, no. 7, pp. 1185–1191, Jul. 2001.
- [63] H. Steendam and M. Moeneclaey, "Analysis and optimization of the performance of OFDM on frequency-selective time-selective fading channels," *IEEE Trans. Commun.*, vol. 47, no. 12, pp. 1811–1819, Dec. 1999.
- [64] *Mobile radio conformance tests amendment: Wave 2 tests*, WiMAX Forum Std., Jul. 2007.
- [65] M. Speth, S. A. Fechtel, G. Fock, and H. Meyr, "Optimum receiver design for wireless broad-band systems using OFDM-part I," *IEEE Trans. Commun.*, vol. 47, no. 11, pp. 1668–1677, Nov. 1999.
- [66] T. Y. Al-Naffouri, K. M. Z. Islam, N. Al-Dhahir, and S. Lu, "A model reduction approach for OFDM channel estimation under high mobility conditions," *IEEE Trans. Signal Process.*, vol. 58, pp. 2181–2193, Apr. 2010.
- [67] O. O. Oyerinde and S. H. Mneney, "Iterative decision directed channel estimation for BICM-based MIMO-OFDM systems," in *GLOBECOM 2010 IEEE*, Dec. 2010.
- [68] N. Tran, H. Nguyen, and T. Le-Ngoc, "Multidimensional subcarrier mapping for bit-interleaved coded OFDM with iterative decoding," *IEEE Trans. Signal Process.*, vol. 55, pp. 5772–5781, 2007.
- [69] —, "Bit-interleaved coded OFDM with signal space diversity: Subcarrier grouping and rotation matrix design," *IEEE Trans. Signal Process.*, vol. 55, pp. 1137–1149, 2007.
- [70] H. Chen and R. Schober, "Cyclic space-frequency filtering for BICM-OFDM systems with multiple co-located or distributed transmit antennas," *IEEE Trans. Wireless Commun.*, vol. 8, no. 4, pp. 1825–1835, Apr. 2009.
- [71] H. Chen, R. Schober, and W. Gerstacker, "Robust transmit processing for BICM-OFDM systems," *IEEE Trans. Wireless Commun.*, vol. 8, pp. 5671–5681, Nov. 2009.

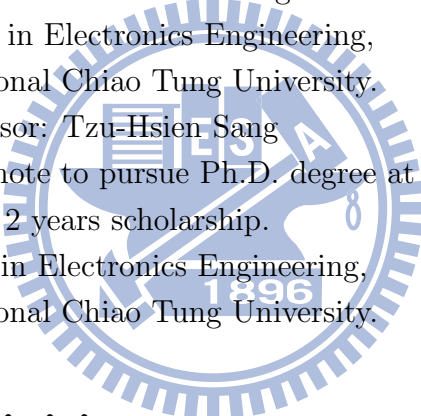
- [72] L. Zhao, J. Huber, and W. Gerstacker, "Design and analysis of bit interleaved coded space-time modulation," *IEEE Trans. Commun.*, vol. 56, no. 6, pp. 904–914, Jun. 2008.
- [73] Z. Yang, Q. Xie, K. Peng, and J. Song, "Labeling optimization for bicm-id systems," *IEEE Commun. Lett.*, vol. 14, no. 11, pp. 1047–1049, Nov. 2010.
- [74] Z. Tang and G. Leus, "Low-complexity equalization for maximum diversity transmissions over doubly-selective channels," *IEEE Trans. Signal Process.*, vol. 54, pp. 3642–3648, Sep. 2006.
- [75] D. S. Bernstein, *Matrix Mathematics: Theory, Facts, and Formulas*, 2nd ed. Princeton University Press, 2009.
- [76] J. Kim, R. W. Heath, and E. J. Powers, "Receiver designs for Alamouti coded OFDM systems in fast fading channels," *IEEE Trans. Wireless Commun.*, vol. 4, no. 2, pp. 550–559, Mar. 2005.
- [77] S. Lu, B. Narasimhan, and N. Al-Dhahir, "A novel SFBC-OFDM scheme for doubly-selective channels," *IEEE Trans. Veh. Technol.*, vol. 58, no. 5, pp. 2573–2578, Jun. 2009.
- [78] D.-B. Lin, P.-H. Chiang, and H. Li, "Performance analysis of two-branch transmit diversity block-coded OFDM systems in time-varying multipath Rayleigh-fading channels," *IEEE Trans. Veh. Technol.*, vol. 54, no. 1, pp. 136–148, Jan. 2005.
- [79] J. Tan and G. L. Stuber, "Multicarrier delay diversity modulation for MIMO systems," *IEEE Trans. Wireless Commun.*, vol. 3, no. 5, pp. 1756–1763, Sep. 2004.

Personal Resume

Name: Hsin-De Lin (林欣德)
Lab: Communication Electronics and Signal Processing Laboratory (CommLab)
Address: Department of Electronics Engineering and Institute of Electronics,
National Chiao Tung University,
1001 Ta-Hsueh Road, Hsinchu, Taiwan 30010, R.O.C.
E-mail: good.goodee92g@gmail.com

Academic Background

2004/09 – present Ph.D. candidate in Electronics Engineering,
National Chiao Tung University.
Advisors: Tzu-Hsien Sang and David W. Lin
2003/9 – 2004/06 M.S. in Electronics Engineering,
National Chiao Tung University.
Advisor: Tzu-Hsien Sang
Promote to pursue Ph.D. degree at 2004/09
with 2 years scholarship.
1999/9 – 2003/06 B.S. in Electronics Engineering,
National Chiao Tung University.



Professional Activities

Reviewer

IEEE Transactions on Vehicular Technology

Conference Presentation

2006/12 IEEE Globecom, San Francisco, USA

Publications

Journals

1. **Hsin-De Lin** and Tzu-Hsien Sang, "On the Diversity Order of BICM-OFDM in Doubly Selective Fading Channels," to appear in *IEEE Transaction on Vehicular Technology*, 2013.
2. **Hsin-De Lin**, Tzu-Hsien Sang, and Jiunn-Tsair Chen, "Low-Cost Perturbation-Based ICI Equalizers for OFDMA Mobile Systems," *IEICE Transaction on Communications*, vol. E95-B, no. 11, pp. 3509-3518, Nov. 2012.

Conferences

1. **Hsin-De Lin**, Tzu-Chieh Lin, and Tzu-Hsien Sang, "Estimation of Channel Variation and Its Applications in OFDM-Based Systems," *The 12th International Conference on ITS Telecommunications*, 2012.
2. Tsung-Ta Lu, **Hsin-De Lin**, and Tzu-Hsien Sang, "An SFBC-OFDM receiver to combat multiple frequency offsets in cooperative communications," *Personal Indoor and Mobile Radio Communications (PIMRC), 2010 IEEE 21st International Symposium on*.
3. Yu-Feng Chou, Tzu-Hsien Sang, and **Hsin-De Lin**, "Efficient Interpolation of Precoding Matrices in MIMO-OFDM Systems," *The 11th IEEE International Workshop on Signal Processing*, 2010.
4. **Hsin-De Lin**, Tzu-Hsien Sang, and David W. Lin, "BICM-OFDM for Cooperative Communications with Multiple Synchronization Errors," *International Wireless Communications and Mobile Computing Conference 2010*.
5. **Hsin-De Lin**, Sheng-Yi Hsu, and Tzu-Hsien Sang, "A Histogram-based Symbol Timing Synchronization Algorithm for OFDM Systems," *IEEE GLOBECOM 2006*.

6. Chin-Yun Hung, **Hsin-De Lin**, and Tzu-Hsien Sang, "A Sphere Decoding Algorithm for MIMO Channels," *Signal Processing and Information Technology, 2006 IEEE International Symposium on*.

